JPL D-13398, Rev. A
December 13, 1999

Multi-angle Imaging SpectroRadiometer (MISR)

Level 1
In-flight Radiometric Calibration
and Characterization
Algorithm Theoretical Basis

Approvals:

David J. Diner
MISR Principal Investigator

Thomas R. Livermore
MISR Project Manager

Graham W. Bothwell
MISR Science Data System Manager

The MISR web site should be consulted to determine the latest released version of this document (http://www-misr.jpl.nasa.gov). Approval signatures are on file with the MISR Project.

JPL

Jet Propulsion Laboratory
California Institute of Technology

TABLE OF CONTENTS

ACRONYMS

A
ADC   analog-to-digital converter
ARP   Ancillary Radiometric Product
ATB   Algorithm Theoretical Basis
AU   astromonical unit

B
BRF   bi-directional reflectance factor

C
CCD   Charge-Coupled Device

D
DAAC   Distributed Active Archive Center
DDQI   Detector Data Quality Indicators
DFM   design file memorandum
DN   digital number
DQI   Data Quality Indicator

E
EFL   effective focal length
EOS   Earth Observing System

F
FWHM   full-width-half-maximum

H
HDF   Hierarchical Data Format
HQE   high quantum efficiency

I
IFOV   instantaneous fields-of-view
IFRCC   In-flight Radiometric Calibration and Characterization

M
MISR   Multi-angle Imaging SpectroRadiometer
MODIS   Moderate Resolution Imaging Spectroradiometer

N
NIST   National Institute of Standards and Technology

O
OBC   On-Board Calibrator
OCC   Optical Characterization Chamber

P
PIN   p-i-n intrinsic layer doped photodiode

PSF   point-spread function

R
RCC   Radiometric Characterization Chamber
RTC   radiative transfer code

S
SCF   Science Computing Facility
SNR   signal-to-noise ratio

T
TOA   top-of-atmosphere

V
VC   Vicarious Calibration

1. INTRODUCTION

1.1 PURPOSE

This Algorithm Theoretical Basis (ATB) document describes the algorithms which operate at the Multi-angle Imaging SpectroRadiometer (MISR) Science Computing Facility (SCF) as part of the In-flight Radiometric Calibration and Characterization (IFRCC) subsystem. In particular, this subsystem produces the MISR Ancillary Radiometric Product (ARP), which is required as input for generation of the MISR Level 1B1 Radiometric Product at the Distributed Active Archive Center (DAAC). The ARP is distributed and revised in four separate Hierarchical Data Format (HDF) files. The file descriptions are given at the end of this chapter, in Table 1.2, followed by a detailed parameter listing in Tables 1.3 to 1.6.

This document assumes the reader has a basic understanding of the MISR design parameters and experiment approach. This is required in order to understand the rationale behind the ARP parameter dimensions (i.e., camera, band, and averaging mode). In brief, MISR has nine cameras each with four spectral bands, for a total of 36 data channels. Within each channel, there may be 1504, 752, or 376 data samples transmitted, per line, depending on the averaging mode for which a channel is configured. Greater details can be found in a number of references, including the [Exp] and [IFRCC Plan], where these project references are defined below.

1.2 SCOPE

This document serves to identify sources of input data, provides a background to the algorithm selection, and gives a mathematical description of the processes used for generation of instrument calibration and characterization data, in particular the parameters contained in the ARP. It also describes practical considerations which were factored into the algorithm development. Chapter 1 defines the ARP, and lists MISR project reference documents. Chapters 2 through 5 give the theoretical basis for the four ARP structures (preflight characterization, preflight calibration, in-flight calibration, and configuration file parameters), respectively. Chapter 6 lists assumptions and limitations. Chapter 7 gives open literature and internal design file memorandum (DFM) references. Appendix A provides a discussion of basis of the radiometric equations used by MISR. Appendix B discusses the pre-launch radiometric response data analysis, in that it differs from the post-launch approach.

1.3 MISR DOCUMENTS

Throughout this document a notation of the form [shorthand] will be used to reference project documents. These definitions are:

[Exp]	Experiment Overview, JPL D-13407.
[ISR]	Instrument Science Requirements, JPL D-9090, Rev. B.
[FDR]	Instrument Functional and Design Requirements, JPL D-9988, Rev. B, Aug96.

[CalMgmt]	Calibration Management Plan, JPL D-7463.
[PreCal]	Preflight Calibration Plan, JPL D-11392.
[IFRCC Plan]	In-flight Radiometric Calibration and Characterization Plan, JPL D-13315.
[L1Rad ATB]	Level 1 Radiance Scaling and Conditioning Algorithm Theoretical Basis, JPL D-11507, Rev. B.
[VC ATB]	Under preparation.
[GeoCal Plan]	In-flight Geometric Calibration Plan, JPL D-13228.
[L1Geo ATB]	Level 1 Georectification and Registration Algorithm Theoretical Basis, JPL D-11532, Rev. B.
[DSSR]	Data System Science Requirements, JPL D-11398.
[DPD]	Data Product Description, JPL D-11103.
[ADP]	Algorithm Development Plan, JPL D-11220.
[DPSize]	Science Data Processing Sizing Estimates, JPL D-12569.
[L2Aer ATB]	Level 2 Aerosol Retrieval ATB, JPL D-11400, Rev. B.
[L2Surf ATB]	Level 2 Surface Retrieval ATB, JPL D-11401, Rev. B.

Conversely, open literature references, internal Design File Memorandum (DFM), and Science Design File Memorandum (SDFM) listings are pointed to by means of superscript numbers in the text. These numbers refer to the publications listed in Chapter 7.

1.4 REVISIONS

This is Rev. A of this document. Changes from the original document are listed below.

- The dimensions of several paramters have been changed in Tables 1.3 through 1.6. These include the measured response profiles, R_λ, and the calibration uncertainties ε_{abs_sys}, ε_{abs}, ε_{cam_sys}, ε_{cam}, ε_{band_sys}, ε_{band}, ε_{pix_sys}, and ε_{pix}. These are now specified on a per camera basis. There are now two threshold parameters for saturation and line average errors: $\varepsilon_{pix\_sat\_1}$, $\varepsilon_{pix\_sat\_2}$ and $\varepsilon_{line\_sat\_1}$, $\varepsilon_{line\_sat\_2}$.
- Extensive revisions have been made to Chapter 4. The in-flight processing algorithms are now better defined, including an approach for computing radiometric uncertainties and making use of our Spectralon bidirectional reflectance factor data base.
- Algorithms used for delivering the pre-launch determined response coefficients have been

moved to Appendix B.
Revisions must be approved by the MISR Principal Investigator and Instrument Scientist.

1.5 NOTATION

Throughout this document the following notation is used in conjunction with algorithm parameters.

- The subscript λ is used to denote a parameter which is a spectral function, e.g.
  - L_λ, the scene spectral radiance;
  - $E_{0\lambda}$, the exo-atmospheric solar irradiance at 1 A.U.

- The indices c, b, and p append a parameter that has a camera (9), band (4), or pixel (9x4x1504) dependency. Sample s and wavelength are also used.
  - EFL(c), the effective focal length of camera c;
  - $S_\lambda(b,\lambda)$, the standardized spectral response profile for band b and wavelength λ;
  - PSF(c,b,s), the point-spread function for camera c, band b, sample s;
  - $G_0(c,b,p)$, $G_1(c,b,p)$, and $G_2(c,b,p)$, the radiometric gain coefficients for pixel p.

- The subscripts g and m describe a spectral parameter that has been computed using either the gaussian or moments analysis equations, respectively. Other subscripts, such as "solar" (referring to a solar weighted parameter), and superscripts such as "meas", and "std" (weighting by the measured and standardized spectral response functions), are defined throughout the document, as needed, e.g.
  - $\lambda_{m,solar}^{meas}$, center wavelength computed using the solar-weighted measured spectral response profile;

  - $\lambda_{m,solar}^{std}$, center wavelength computed using the solar-weighted standardized spectral response profile;

  - $\lambda_g^{std,in-band}$, center wavelength computed from a gaussian best-fit to the standardized in-band profile.

- Band averaged parameters are designated by use of script parameters (e.g., $\mathcal{L}^{meas,\,in-band}$, $\mathcal{E}_0^{std}$). Unless otherwise stated, band-weighting is over the entire spectral response range of the sensor, 365 to 1100 nm. The superscripts "in-band" and "out-band" denote exceptions to the total-band weighting convention.

When referring to a specific pixel, a value between 1 and 1504 shall be used. The ARP generation software must make the appropriate translation between other numbering conventions. Specifically, for parameters generated from the spectral analysis code, or pinhole image scans, the active pixels were numbered 12 through 1515. These preflight tests always refer to the CCD clock order. Conversely, the parameters within the ARP are pixel-order reversed for the nadir and aftward viewing cameras. The translation between a preflight test pixel number and ARP pixel number is provided by the following table:

Table 1.1. Preflight pixel number to ARP pixel number conversion algorithms

Preflight test	Cameras	Preflight pixel indices, p	Corresponding ARP pixel indices, pARP
Radiometric analysis	Forward	1-1504	pARP=p (values 1-1504)
	Aft and Nadir	1-1504	pARP=1505-p (values 1504-1)
Spectral analysis	Forward	12-1515	pARP=p-11 (values 1-1504)
	Aft and Nadir	12-1515	pARP=1516-p (values 1504-1)
Pinhole image scan	Forward	12-1515	pARP=p-11 (values 1-1504)
	Aft and Nadir	12-1515	pARP=1516-p (values 1504-1)

The ARP coefficients are placed into the HDF file in an averaging mode (subscript am), camera (c), band (b), pixel (p), and radiometric level (l) order. The index order is:

- averaging mode: 1x1, 1x4, 2x2, and 4x4;
- camera order is: Df, Cf, Bf, Af, An, Aa, Ba, Ca, and Da;
- band order: Blue, Green, Red, NIR;
- pixel order is to be from 1 to 1504 for the forward cameras, and from 1504 to 1 for the nadir and aftward-viewing cameras, where this pixel index refers to the original camera clocking output order;
- radiometric levels: from low to high values (0.001 to 1.0).

Table 1.2. ARP structures

File name	Description
Preflight Characterization Data	This file contains preflight instrument characterization parameters, supplied for data user reference. Examples include the measured spectral response functions, and the instantaneous fields-of-view. These parameters are not used by DAAC processes. It is unlikely that this file will be modified once delivered. A version number will be tracked, however, should this be the case.
Preflight Calibration Data	This file contains preflight calibration data. It is distinguished from the Preflight Characterization Data file, in that these data are used as input to DAAC processes. Parameters include spectral descriptors relevant to the standard products, and band weighted solar irradiances. Radiometric gain coefficients are not included here, as they are updated on-orbit. It is unlikely that this file will be modified once delivered. A version number will be tracked, however, should this be the case.
In-flight Calibration Data	This file contains in-flight calibration data. It is also used as input to DAAC standard product generation. It is distinguished from the Preflight Calibration Data file, in that these instrument parameters are monitored on-orbit. At-launch values are initialized by the preflight calibration data. Monthly updates to this file allow processing to continue with current performance metrics. Parameters include radiometric calibration coefficients, calibration uncertainties, signal-to-noise ratios, and Detector Data Quality Indicators. A version number will track file format changes; a date range revision number will indicate a revision has been made to the parameters, should this occur.
Configuration Parameters	This file contains threshold parameters and process control limits used by DAAC processes. Examples are the average digital number (DN) value of a line above which data integrity is reduced, and the number of iterations performed for point-spread function (PSF) deconvolution. They are expected to change only at the discretion of the Principal Investigator, Instrument Scientist, and the Science Team. Such a change would reflect a relaxation or stricter tolerance of specific data anomalies. A version number will reflect any such changes.

Table 1.3. ARP: Preflight characterization data. Parameters marked in column R have pixel order reversed for the forward cameras, as compared to the CCD read-out order.

Parameter name [units]	No. of values	Section	Comments	R
Version number	1	2.1	Incremented if file format or parameters are revised.	
Spectral response profiles:				
$R_\lambda(c,b,s,\lambda)$ [none], measured response profiles	9x4x3x 1471	2.2.4	Each profile from 365 to 1100 nm in 0.5 nm steps. These measured profiles provide the system transmittance with wavelength. Data are reported for one pixel within each of the 7 zones at which data were acquired.	√
$Z_R(c,b,s)$ [none], measured response profile zones	9x4x3	2.2.5	Pixel value within each zone that is associated with the above spectral response function measurements.	√
$S_\lambda(b,\lambda)$ [none], standardized response profiles	4x1471	2.2.6	Each profile from 365 to 1100 nm in 0.5 nm steps. Processing which do not remove the out-of-band contribution report band-weighted radiances, corrected to these standardized spectral response functions.	
$S_\lambda^{in\text{-}band}(b,\lambda)$ [none], in-band standardized response profiles	4x200	2.2.6	Each profile from 365 to 1100 nm in 0.5 nm steps. Certain Level 2 products, i.e. those in which the out-of-band response has been removed, report equivalent reflectances weighted by these in-band profiles.	
in-band wavelength limits: $\lambda_l^{std}(b)$ [nm], lower limit, and $\lambda_u^{std}(b)$ [nm], upper limit	λ_l^{std}: 4 λ_u^{std}: 4	2.2.6	Used to define starting wavelength for $S_\lambda^{in\text{-}band}$ database	
Gaussian analysis parameters, unweighted:				
$S_g^{in\text{-}band}(b)$ [none], peak response, gaussian fit to the standardized profile	4	2.3	Peak system transmittance of a best-fit gaussian to the standardized spectral response function.	

1. Introduction

Table 1.3. ARP: Preflight characterization data. Parameters marked in column R have pixel order reversed for the forward cameras, as compared to the CCD read-out order.

Parameter name [units]	No. of values	Section	Comments	R
$\lambda_g^{std,in-band}(b)$ [nm], center wavelength, gaussian fit to the standardized profile	4	2.3	Best-fit gaussian parameter.	
$\Delta\lambda_g^{std,in-band}(b)$ [nm], bandwidth, gaussian fit to the standardized profile	4	2.3	Best-fit gaussian parameter.	
$R_g^{in-band}(c,b,p)$ [none], peak response, gaussian fit to the measured profile	9x4x 1504	2.3	Peak system transmittance of a best-fit gaussian to the measured spectral response functions.	√
$\lambda_g^{meas,in-band}(c,b,p)$ [nm], center wavelength, gaussian fit to the measured profile	9x4x 1504	2.3	Best-fit gaussian parameter.	√
$\Delta\lambda_g^{meas,in-band}(c,b,p)$ [nm], bandwidth, gaussian fit to the measured profile	9x4x 1504	2.3	Best-fit gaussian parameter.	√
Moments analysis parameters, unweighted:				
$S_m^{std}(b)$ [none], equivalent response, moments analysis of the standardized profile	4	2.4	Equivalent square-band transmittance, determined from standardized spectral response.	
$\lambda_m^{std}(b)$ [nm], center wavelength, moments analysis of the standardized profile	4	2.4	Equivalent square-band center wavelength from the standardized spectral response.	

Table 1.3. ARP: Preflight characterization data. Parameters marked in column R have pixel order reversed for the forward cameras, as compared to the CCD read-out order.

Parameter name [units]	No. of values	Section	Comments	R
$\Delta\lambda_m^{std}(b)$ [nm], bandwidth, moments analysis of the standardized profile	4	2.4	Equivalent square-band bandwidth from the standardized spectral response.	
$R_m(c,b,p)$ [none], equivalent response, moments analysis of the measured profile	9x4x 1504	2.4	Equivalent square-band transmittance, determined from the measured spectral response.	√
$\lambda_m^{meas}(c,b,p)$ [nm], center wavelength, moments analysis of the measured profile	9x4x 1504	2.4	Equivalent square-band center wavelength from the measured spectral response.	√
$\Delta\lambda_m^{meas}(c,b,p)$ [nm], bandwidth, moments analysis of the measured profile	9x4x 1504	2.4	Equivalent square-band bandwidth from the measured spectral response.	√
Exo-atmospheric solar irradiance:				
$E_{0\lambda}(\lambda)$ [W m^{-2} μm^{-1}], exo-atmospheric solar irradiance	1471	2.5	Spectra from 365 to 1100 nm, resampled to 0.5 nm steps. World Climate Research Programme[12] data	
Solar and measured response weighted parameters:				
$E_0^{meas}(c,b,p)$ [W m^{-2} μm^{-1}], solar irradiances, measured response weighted	9x4x 1504	2.5	Reported for each pixel.	√
$\lambda_{m,solar}^{meas}(c,b,p)$ [nm], center wavelength, solar and measured response weighted	9x4x 1504	2.5	Describes spectral parameters associated with the measured response weighted exo-atmospheric solar irradiances.	√

Table 1.3. ARP: Preflight characterization data. Parameters marked in column R have pixel order reversed for the forward cameras, as compared to the CCD read-out order.

Parameter name [units]	No. of values	Section	Comments	R
$\Delta\lambda_{m,solar}{}^{meas}(c,b,p)$ [nm], bandwidth, solar and measured response weighted	9x4x 1504	2.5	"	√
Instantaneous fields-of-view:				
$IFOV_x(c,b,s)$ [μrad], crosstrack instantaneous fields-of-view	9x4x5	2.6	Estimated from crosstrack pointing angle at five field-angle locations.	√
$IFOV_d(c,b,s)$ [μrad], downtrack fields-of-view	9x4x5	2.6	Determined from downtrack scan as half response angle. Reported at same five field-angle locations as above.	√
$Z_{ifov}(c,b,s)$ [none], measured IFOV zones	9x4x5	2.6	Pixel values corresponding to each of the above IFOV measurements, per channel.	√
Effective focal length:				
$EFL(c)$ [mm], effective focal length	9	2.7	Reported for each camera.	

Table 1.4. ARP: Preflight calibration data

Parameter [units]	No. of values	Section	Comments
Version number	1	3.1	Incremented if file format or parameters are revised.
Solar and in-band standardized response weighted parameters:			
$E_0^{std,in-band}(b)$ [W m^{-2} μm^{-1}], solar irradiances, in-band standardized response weighted	4	3.2	Used in converting between radiances and equivalent reflectances, where out-of-band correction has been applied.
$\lambda_{m,solar}^{std,in-band}(b)$ [nm], center wavelength, solar and in-band standardized response weighted	4	3.2	Spectral descriptor for Level 2 products in which the out-band energy has been subtracted.
$\Delta\lambda_{m,solar}^{std,in-band}(b)$ [nm], bandwidth, solar and in-band standardized response weighted	4	3.2	"
Solar and total-band standardized response weighted parameters:			
$E_0^{std}(b)$ [W m^{-2} μm^{-1}], solar irradiances, standardized response weighted	4	3.3	Used in converting between radiances and equivalent reflectances, where out-of-band correction has not been applied.
$\lambda_{m,solar}^{std}(b)$ [nm], center wavelength, solar and standardized response weighted	4	3.3	Spectral descriptor of spectral response function, to be used where out-of-band correction has not-been applied.
$\Delta\lambda_{m,solar}^{std}(b)$ [nm], bandwidth, solar and standardized response weighted	4	3.3	"

1. Introduction

18

Table 1.4. ARP: Preflight calibration data

Parameter [units]	No. of values	Section	Comments
c(b,s) [none], Spectral out-of-band correction matrix	4x4	3.4	Used to remove out-of-band contribution to equivalent reflectances in deriving certain Level 2 products
$PSF_{am}(c,b,s)$ [none], PSF functions	PSF_{1x1}: 9x4x51 PSF_{2x2}: 9x4x25 PSF_{4x4}: 9x4x13	3.5	Used to derive the PSF deconvolution kernels, given below
$DPSF_{am}(c,b,s)$ [none], PSF deconvolution kernels	$DPSF_{1x1}$: 9x4x51 $DPSF_{2x2}$: 9x4x25 $DPSF_{4x4}$: 9x4x13	3.6	Used in Level 1B1 radiance conditioning: image restoration processing. Function assumed to be 51 points in 1x1. Provided for each channel and averaging mode.
PAR(b) [none], PAR integration weights	3	3.7	Used at Level 2 for generation of hemispherical reflectances in photosynthetically active region. Provided for b=1,2, and 3.

Table 1.5. ARP: In-flight calibration data. Parameters marked in column R have pixel order reversed for the forward cameras, as compared to the CCD read-out order.

Parameter [units]	No. of values	Section	Comments	R
Version number	1	4.1	Incremented if file format is revised.	
Revision number	1	4.1	Incremented if the data values are corrected	
Radiometric calibration coefficients:				
Calibration date	3	4.2	The date of the calibration experiment	
Radiometric gain coefficients: $G_{0,am}(c,b)$ [DN] gain offset; $G_{1,am}(c,b)$ [DN/ (W m^{-2} µm^{-1} sr^{-1})] gain; $G_{2,am}(c,b)$ [DN/ (W m^{-2} µm^{-1} sr^{-1})^2] gain second order coefficient	$G_{0,1x1}$: 9x4x1504 $G_{1,1x1}$: 9x4x1504 $G_{2,1x1}$: 9x4x1504 $G_{0,2x2}$: 9x4x752 $G_{1,2x2}$: 9x4x752 $G_{2,2x2}$: 9x4x752 $G_{0,4x4}$: 9x4x376 $G_{1,4x4,}$: 9x4x376 $G_{2,4x4}$: 9x4x376	4.3.6.1	Provides band-averaged radiance given pixel DN. Determined from OBC, vicarious calibration, and histogram equalization methodologies. Separate coefficient tables used for the 1x1 (or 1x4), 2x2, and 4x4 averaging modes.	√
$t_{integ}(c,b)$ [msec], integration time	9x4	4.4	Integration times associated with the above calibration coefficients. Reported for each channel.	
Calibration uncertainties:				
ER(l) [none], equivalent reflectances	15	4.5	Equivalent reflectances at which calibration uncertainties and signal-to-noise are reported.	
$\varepsilon_{abs\_sys}(c,b,l)$ [%], absolute radiometric uncertainty: systematic component	9x4x15	4.9	Provided at 15 radiometric levels for each channel.	

Table 1.5. ARP: In-flight calibration data. Parameters marked in column R have pixel order reversed for the forward cameras, as compared to the CCD read-out order.

Parameter [units]	No. of values	Section	Comments	R
$\varepsilon_{abs}(c,b,l)$ [%], absolute radiometric uncertainty: total for 1x1	9x4x15	4.9	Provided at 15 radiometric levels for each channel.	
$\varepsilon_{cam\_sys}(c,b,l)$ [%], camera-to-camera relative radiometric uncertainty: systematic component	9x4x15	4.9	Provided at 15 radiometric levels for each channel.	
$\varepsilon_{cam}(c,b,l)$ [%], camera-to-camera relative radiometric uncertainty: total for 1x1	9x4x15	4.9	Provided at 15 radiometric levels for each channel.	
$\varepsilon_{band\_sys}(c,b,l)$ [%], band-to-band relative radiometric uncertainty: systematic component	9x4x15	4.9	Provided at 15 radiometric levels for each channel.	
$\varepsilon_{band}(c,b,l)$ [%], band-to-band relative radiometric uncertainty: total for 1x1	9x4x15	4.9	Provided at 15 radiometric levels for each channel.	
$\varepsilon_{pix\_sys}(c,b,l)$ [%], pixel-to-pixel relative radiometric uncertainty: systematic component	9x4x15	4.9	Provided at 15 radiometric levels for each channel.	
$\varepsilon_{pix}(c,b,l)$ [%], pixel-to-pixel relative radiometric uncertainty: total for 1x1	9x4x15	4.9	Provided at 15 radiometric levels for each channel.	

Table 1.5. ARP: In-flight calibration data. Parameters marked in column R have pixel order reversed for the forward cameras, as compared to the CCD read-out order.

Parameter [units]	No. of values	Section	Comments	R
$SNR_{am}(c,b,l)$ [none], signal-to-noise ratios	SNR_{1x1}: 9x4x15 SNR_{1x4}: 9x4x15 SNR_{2x2}: 9x4x15 SNR_{4x4}: 9x4x15	4.6	Provided at 4 averaging modes, 15 radiometric levels, and for each channel.	
$DDQI_{am}(c,b,s)$ [none], Detector Data Quality Indicators	$DDQI_{1x1}$ 9x4x1504 $DDQI_{2x2}$ 9x4x752 $DDQI_{4x4}$ 9x4x376	4.7	Values 0 (within specification), 1 (reduced accuracy), 2 (unusable for science), and 3 (unavailable). Provided for each pixel and averaging mode.	√
$F(c,b)$ [none], channel operability flag	9x4	4.8	Values 0 (some or all of the data within the channel are valid), 1 (dead channel)	

Table 1.6. ARP: Configuration file parameters

Parameter [unit]	No. of values	Section	Comments
Version number		5.1	Incremented if file format or parameters are revised.
$L_{max}(b)$ [W m^{-2} μm^{-1} sr^{-1}], band weighted maximum radiance	4	5.2	Used to scale Level 1B1 radiances to a 14-bit integer. Defined as the maximum radiance a band can observe before saturation.
$DN_{pix\_sat}(c,b)$ [DN], pixel saturation threshold	9x4	5.3	DN above which the analog-to-digital converter (ADC) is saturated
n_{pix_sat}[none], number of allowable saturated pixels	1	5.3	If the number of saturated pixels exceeds n_{pix_sat}, the entire line is considered unusable.
Pixel saturation block limits: $n_{am}(s)$ [none], saturation block start and saturation block end.	n_{1x1}: 2 n_{2x2}: 2 n_{4x4}: 2	5.3	Number of pixels to subtract from (add to) saturated pixel location to identify beginning (end) of saturation block. Provided for each of 1x1 (or 1x4), 2x2, and 4x4 averaging modes (am).
$a_{pix\_sat}(s)$ [none], pixel saturation noise coefficients	2	5.3	Coefficients used in conjunction with the number of pixels saturated in a line, to predict the noise pedestal associated with saturation blooming.
$\varepsilon_{pix\_sat}(s)$[%], pixel saturation error thresholds	2	5.3	Percentage radiometric error thresholds (e.g. 0.5% and 10%) allowed in the presence of saturation blooming.
$DN_{line\_sat}(c,b)$ [DN], line average threshold	9x4	5.4	Line average DN above which data quality might be impaired.
$\Delta DN_{line\_sat}(c,b)$ [DN], line average noise	9x4	5.4	Estimated uncertainty in video offset resulting from the average data number across a given line exceeding DN_{line_sat}.
$\varepsilon_{line\_sat}(s)$ [%], line average error thresholds	2	5.4	Percentage radiometric error thresholds (e.g. 0.5% and 10%) allowed in the presence of video offset uncertainty, as measured by the overclock pixels.

2. ARP: PREFLIGHT CHARACTERIZATION DATA

The parameters contained within the ARP: Preflight Characterization Data file are given in Table 1.2. The basis for their computation is given in this chapter.

2.1 VERSION NUMBER

It is unlikely that this file will be modified once delivered. A version number will be tracked, however, should this be the case. Version numbers are incremented in sequence. Each of the four ARP files have their own version identifier, so that they might be modified independently of each other. Metadata within the ARP file provide a unique file identifier, published within the Level 1A product.

2.2 SPECTRAL RESPONSE PROFILES

Spectral calibration of the nine cameras and photodiodes is performed preflight, and assumed invariant during the flight mission. Strength to this assumption is given in that MISR has made use of Ion Assisted Deposition (IAD) filter technology. This provides thin-film coatings which are densely packed, and impermeable to water absorption. In previous remote sensing instruments, changes in the spectral properties of filters have been attributed to water absorption within the thin-film layers. Early Landsats, for example, were calibrated in ambient conditions, and experienced a spectral shift on-orbit once the sensors were in a vacuum condition. As the MODerate Resolution Imaging Spectroradiometer (MODIS) will also utilize IAD filters, and as this instrument has an on-board spectrometer, stability of the IAD design will be confirmed on-orbit. Lacking any colored contaminants on the elements, there are no known mechanisms which would lead to a change in the spectral response of the MISR cameras.

The spectral response functions and parameters reported for MISR refer to the system response, taking into account the optics and filter spectral transmittances, and the CCD spectral quantum efficiency across each band. Field-angle dependencies of these quantities are provided, as needed to characterize the response of individual pixels. These measured spectral response functions are denoted $R_{\lambda,p}$. The "in-band" region is defined to be the spectral range over which the response continuously exceeds 1% of the peak response. The MISR cameras are found to have a non-negligible response (system transmittance in the range 10^{-4} to 10^{-3}) outside of the in-band region9. The radiances reported at Level 1B1 contain contributions from the out-of-band region. Certain Level 2 products are corrected for the out-of-band response [L2Aer ATB].

2.2.1 System response model

Prior to the spectral calibration of a camera, a combined radiometric and spectral model for that camera is prepared. This model combines component spectral measurements with the system-level radiometric calibration. It therefore provides an equivalent to the measured spectral response profile of each charge-coupled device (CCD) detector element, but is provided on an absolute transmittance scale. Although the measured system spectral responses are more accurate than the model data, the model is used to assign the measured data to an absolute scale.

The lower wavelength cut-off of the model (365 nm) has been determined using the Code V lens design program. This code contains the MISR lens model, and includes a data base giving spectral transmittance of the lens. This model has been verified by comparing the predicted transmittances to measured test pieces, for the entire 365 to 1100 nm spectral range52. The upper cut-off of the cameras (1100 nm) is provided by the band-gap of the silicon detectors14. This model predicts a cut-off of 1107 nm at 25° C. In fact, the extrapolated measured transmittance predicts that the spectral response goes to 10^{-6} at 1050 nm.

The following are used as input to construct the complete model:

(1) lens data file: contains lens transmittance including the detector window and projected solid angle as a function of wavelength and relative field positions 0.0, 0.25, 0.5, 0.75, and 1.0 (symmetry in crosstrack field is assumed and data is assumed to be constant in downtrack field). Based on CODE V model.

(2) focal plane data file: contains spectral quantum efficiency of the filtered detector used in the current camera produced from Sensor Test Set measurements (data is for each channel and is assumed to be constant across pixels). Measurement range is 350-1000 nm. Linear extrapolation is used for wavelengths outside this range.

(3) flat field file for each channel: contains offset subtracted data numbers averaged over 100-pixel blocks that map to the relative field positions 0.0, 0.25, 0.5, 0.75, and 1.0; and the applicable offset for each channel. This is the measured response of the camera to the integrating sphere.

(4) detector gains (electrons/DN): for each channel, as measured by the camera light transfer test.

(5) integration times: used for each channel at which the flat-field data files were acquired.

(6) radiance of the sphere: output for each channel corresponding to the flat-field files.

With these inputs, a predicted signal in DN corresponding to the flat-field files is derived, based on the unmodified model parameters and input conditions. The integrating sphere is modeled as a 3100 K blackbody, and the blackbody curve is scaled so that the radiance at the band-center wavelength matches the calibrated sphere radiance for the channel and flat-field file. Next, a comparison is made to the actual measured signal in the flat-field files. A scale factor is determined as the ratio of measured to predicted signal. The model response is then adjusted by the scale factor to arrive at the adjusted spectral response model. A separate scale factor is computed at each of the nine field positions for a given channel. The scale factor is assumed to be spectrally flat for the channel and field position to which it is applied.

The resulting models are documented in the MISR design file memorandum (DFM) reports for each of the nine cameras (see Table 7.1).

2.2.2 Spectral response measurements

Relative spectral calibration of the MISR cameras is performed at the camera level (prior to assembly onto the instrument optical bench) under thermal vacuum conditions. A single grating monochromator is used, with a xenon lamp and adjustable exit slit. The exit aperture is fitted with an integrating sphere to improve spectral uniformity of the emitted light. The monochromator output is first observed by laboratory detector-based standards. These are of high quantum efficiency (HQE) design, and in a trapped configuration to account for Fresnel reflections. The standards are known to have a uniform response to photons, independent of wavelength, and thus are used to normalize the camera output by the incoming spectral radiance, such that the camera response to a spectrally neutral source is obtained. When illuminating a camera, the sphere exit aperture simultaneously illuminates a camera "zone" of about 50 crosstrack pixels at all bands. A scan mirror between the monochromator sphere and camera is used to deviate the output such that coverage is obtained for multiple camera zones, sampling the field-of-view. At each zone the monochromator is scanned between 400 and 900 nm. Following this, the next zone is illuminated and the monochromator scan repeated. Due to the time required to obtain test data, only 7 equally spaced zones are tested for the in-band response characterization (about 25% of the array), while 3 zones are tested for the out-of-band response (about 10% of the array). Response curves for pixels not directly measured during this calibration are obtained by interpolation. For an in-band scan, data are acquired at 2.6 nm spectral resolution and 0.5 nm sampling; for the out-of-band scan the resolution is 19.6 nm and sampling is every 10 nm.

Test results are documented in the DFM reports for each of the nine cameras (see Table 7.1). These results are not duplicated here, as it is believed that only the spectral response data reported in Chapter 3 will be utilized by the scientific community.

2.2.3 Data preprocessing

The MISR spectral analysis code, SpectCal, is written in the IDL language. The raw pixel DN data are first conditioned by three procedures. First, there is a video offset subtraction using the mean of the center six shielded pixels that are found at either end of the active pixel region. If the shielded pixels are not suitable, due to a large variability in their value, then the dark frame for that file is used. The equation that represents this processing step is

$$DN_{\lambda,p} = DN_{\lambda,p} - DN_{offset} \qquad (2.1)$$

where DN_{offset} is constant when the shielded pixels are used, and is a function of pixel for the dark frame. (Note that later testing determined that the overclock samples are the best means of determining the offset, which is dynamic and must be sampled for the line of data under analysis. Overclock pixels are signal chain samples which are clocked out following active pixels reads, and are therefore a measure of the system video offset. They are treated as real pixels by the system electronics, i.e., digitized, averaged, and transmitted for ground processing along with other pixels in the channel. In an unaveraged mode, there are eight transmitted overclock pixels per line of data. In general, the shielded pixels are not a good representation of the video offset, as they contain pinholes. For the spectral calibration test, however, they are not typically illuminated, and are therefore an adequate measure of the offset).

The spectra are next normalized to provide the system response to a spectrally flat input. This is done by making use of the laboratory standard output current, HQE_λ, to the monochromator output, via the equation:

$$DN_{\lambda,p} = DN_{\lambda,p} * HQE_{\lambda,c} / HQE_\lambda. \tag{2.2}$$

Here "λ,c" is the nominal center wavelength for the band. This step preserves the DN value at this wavelength, but scales the DN response at other wavelengths according to the relative spectral photon flux, as measured by the photodiode standards. Finally, the recorded wavelengths are calibrated16 for adjustments in the monochromator setting by $\lambda = \lambda * a_0 + a_1$. A new monochromator calibration is made prior to each camera's spectral testing (i.e., the coefficients a_0 and a_1 are recomputed prior to each camera calibration). Data that have been processed for these corrections are termed "conditioned data". At this point data are treated differently, depending on whether they are from in-band or out-of-band measurements.

2.2.4 Composite spectra

As both in- and out-of-band runs are used to characterize the cameras, these must be combined into one profile. The in-band runs have the advantage of high spectral resolution, needed to evaluate an effective band center and width. However, during these in-band runs, there is insufficient response to characterize the out-of-band region. For the out-of-band scans, the monochromator exit slit is opened, allowing greater illumination, as needed for detection of the response in this region. A composite spectrum is first constructed from the out-of-band scan, substituting the response at in-band wavelengths from the in-band run. Care is taken to preserve the relative scale when merging the two files. First, the in-band region of the in-band data from the corresponding zone and band is blurred and resampled at the out-of-band step size. This is done by convolving the in-band data with a gaussian of width 19.3 nm (yielding an output of comparable spectral resolution to the out-of-band data). A comparison of the in- and out-of-band data sets is next made to determine the scale factor between them. Once this scale factor is determined the high resolution in-band data are scaled using this term, then combined with the out-of-band data, which are next sampled at the higher resolution, to allow even sampling distances throughout the composite spectrum. At this step the composite spectrum may exhibit a discontinuity at the borders where the two files are merged. This artifact is removed by extending directly from the base of the narrow in-band peak to a point 20 nm outward. This last modification preserves the same area under this new curve to that which was in the original out-of-band profile.

The last step performed to create a final response curve is to extend the region to all wavelengths for which the MISR cameras have sensitivity. The radiometric/ spectral model data are thus used between 365 and 400 nm, and also from 900 to 1100 nm. Additionally, the peak of the composite array is assigned an absolute transmittance from the model, although the measured relative response is preserved between 400 and 900 nm.

Summarizing these steps mathematically, let

$$s(\lambda_{max}) = \frac{DN_{\lambda max}^{\,out-band}}{\int DN_\lambda^{\,in-band} \exp[-4(\ln 2)(\lambda - \lambda_{max})^2/19.3\,nm^2]\;d\lambda}\;, \tag{2.3}$$

where the scaling is defined at wavelength λ_{max}, with

$$DN_{\lambda max}^{\,out-band} = \max(DN_\lambda^{\,out-band})\;. \tag{2.4}$$

The measured spectral response function is then found from these data:

$$R_{\lambda,\,p} = \frac{DN_\lambda^{\,out-band}\,t(\lambda_c)}{s(\lambda_{max})\;DN_{\lambda c}^{\,in-band}} \quad \text{for } \lambda_l > \lambda \text{ or } \lambda > \lambda_u \tag{2.5}$$

$$= \frac{DN_\lambda^{\,in-band}\,t(\lambda_c)}{DN_{\lambda c}^{\,in-band}} \text{ for } \lambda_l \; \lambda \; \lambda_u \tag{2.6}$$

$$= t(\lambda) \quad \text{for } 400\,nm > \lambda \text{ or } \lambda > 900\,nm\,. \tag{2.7}$$

Here, $t(\lambda)$ is from the spectral response model.

2.2.5 Pixel response function interpolation

The procedure for deriving spectral response profiles for the ARP consists of:

• providing one representative in-band response function for each of the seven measured in-band zones. The profile is selected as that from the pixel with the largest illumination for the scan;

• creating a total-band response function from this in-band measurement, by adding an out-of-band and model extrapolation to the data, per the procedure described above. The out-of-band scan selected is that from the pixel with the largest illumination for the scan, and for the zone closest to where the in-band measurement was made;

• interpolating (or extrapolating, as appropriate) on a pixel-by pixel basis between the seven composite spectral response functions to assign a measured response function, $R_{\lambda,p}$, to each pixel.

2.2.6 Standardized spectral response functions

Because there are slight (a few nm) shifts in band center and bandwidth across the fields of view of each camera, and also from camera to camera, standardized spectral response profiles are

derived from the measured spectral response functions, $R_{\lambda,p}$. MISR radiances are reported as if all detectors of a particular band acquired data in these standardized passbands. The standardized spectral response profiles are derived averaging all 3 zone and 9 camera profiles within a spectral band. This generates a set of four standardized response curves, one for each band, and denoted $S_{\lambda,b}$. The in-band region of this function is denoted $S_{\lambda,b}^{in-band}$ and it lies between the lower and upper wavelength limits $\lambda_{l,b}^{std}$, and $\lambda_{u,b}^{std}$.

2.3 IN-BAND GAUSSIAN ANALYSIS

Analyses of the spectral response functions can lead to descriptor parameters which are approximations to the actual functions. These derived parameters are a mathematical convenience, and additionally useful in defining specifications, in comparing pixel-to-pixel or camera-to-camera response differences, or in assigning a wavelength to which a geophysical parameter (e.g., surface reflectance, or atmospheric transmittance) is reported. The gaussian representation is useful to approximate the MISR in-band region. This is because the MISR filters were designed to be gaussian in shape, allowing a polarization insensitive camera design when used in conjunction with a Lyot depolarizer12. As the filters were specified to be gaussian in wavenumber (corresponding to what the theoretical design provides), the gaussian best-fit analysis is done in the wavenumber domain.

A computation of peak response, $R_{g,p}^{in-band}$, center wavelength, $\lambda_{g,p}^{meas,in-band}$, and full-width-half-maximum (FWHM), $\Delta\lambda_{g,p}^{meas,in-band}$, is made by fitting the data to a gaussian of the form

$$R_{\lambda_{g,p}}^{in-band}=R_{g,p}^{in-band} \exp[-(4 \ln 2)(v-v_{g,p})^2/\Delta v_{g,p}^2] \,. \tag{2.8}$$

where $v=\lambda^{-1}$ denotes wavenumber, $v_{g,p}$ is the center wavenumber; and $\Delta v_{g,p}$ is the FWHM in wavenumber. Only in-band data (between wavelengths where the DN is continuously 1% of peak response), are fitted. Note that the center wavelength and bandwidth in wavelength units can be found from $\lambda_{g,p}^{meas,in-band}=v_{g,p}^{-1}$, and $\Delta\lambda_{g,p}^{meas,in-band}=(v_{g,p}-\Delta v_{g,p}/2)^{-1}-(v_{g,p}+\Delta v_{g,p}/2)^{-1}$. These parameters are computed for each pixel.

The gaussian analysis is repeated fitting the standardized response profiles to derive $S_{g,b}^{in-band}$, $\lambda_{g,b}^{std,in-band}$, and $\Delta\lambda_{g,b}^{std,in-band}$:

$$S_{\lambda_{g,b}}^{in-band}=S_{g,b}^{in-band} \exp[-(4 \ln 2)(v-v_{g,b})^2/\Delta v_{g,b}^2] \,; \tag{2.9}$$

$$\lambda_{g,b}^{std,in-band}=v_{g,b}^{-1}; \text{ and} \tag{2.10}$$

$$\Delta\lambda_{g,b}^{std,in-band}=(v_{g,b}-\Delta v_{g,b}/2)^{-1}-(v_{g,b}+\Delta v_{g,b}/2)^{-1}. \tag{2.11}$$
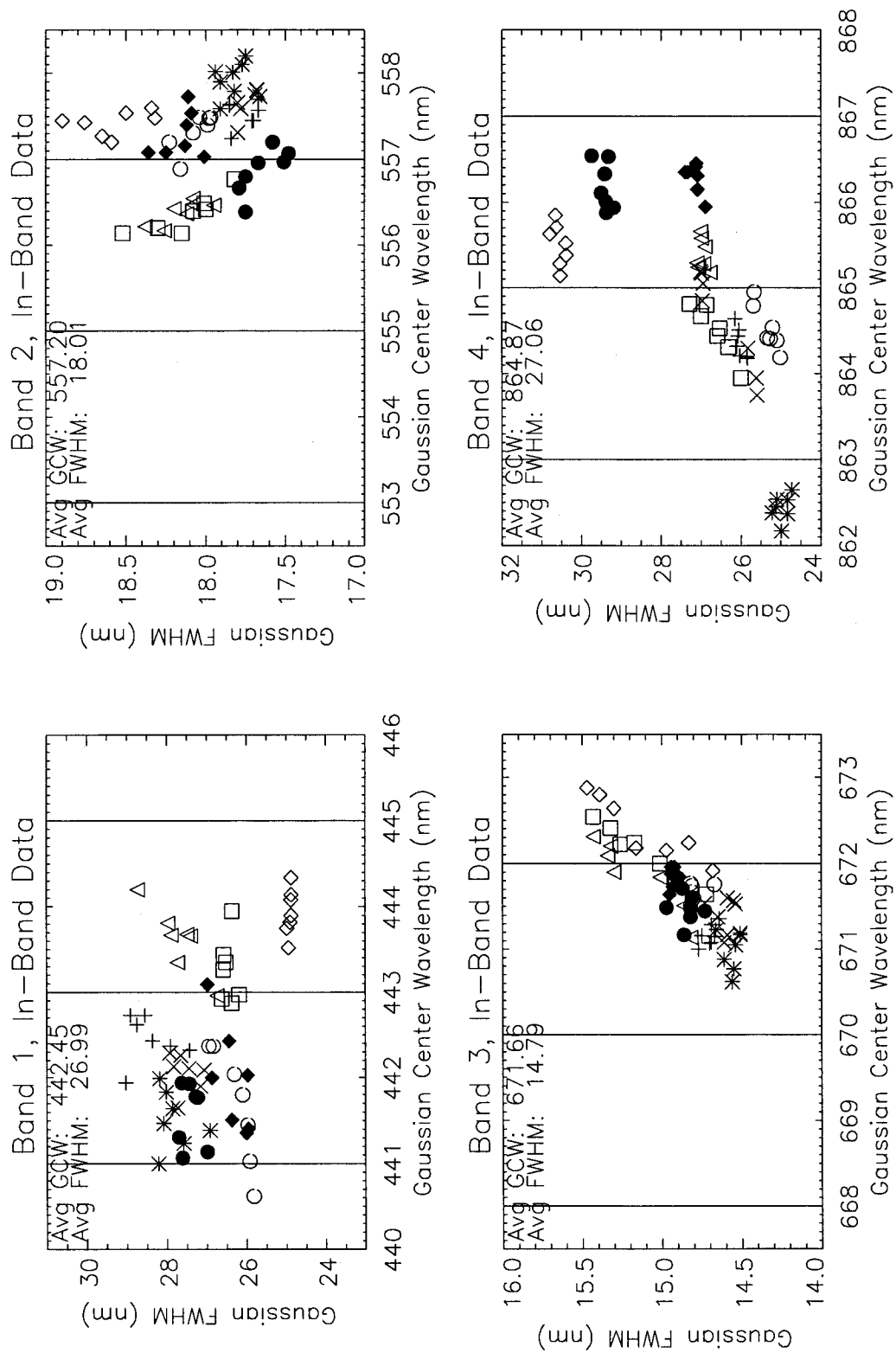
Figure 2.1. Measured gaussian center wavelength and FWHM

Figure 2.1 shows the gaussian center wavelengths and FWHM, as measured for at seven equally spaced zones across each channel. These seven data points are plotted using a common symbol. Data are plotted for each of the nine cameras on a separate plot for each of the four bands. The vertical dashed lines represent the specifications on center wavelength and center wavelength tolerance.

2.4 TOTAL-BAND MOMENTS ANALYSIS

The moments analysis provides an equivalent square band representation of the profile, and is convenient in summarizing the total-band response spectral performance of the array. Using this method the following computations are made:

$$(2.12)$$

$$\lambda_{m,p}^{meas} = \int \lambda \cdot R_{\lambda,p} d\lambda / \int R_{\lambda,p} d\lambda$$

$$\sigma^2 = \int \lambda^2 \cdot R_{\lambda,p} d\lambda / \int R_{\lambda,p} d\lambda - (\lambda_{m,p}^{meas})^2$$

$$\lambda_{u,l} = \lambda_{m,p}^{meas} \pm \sqrt{3} \cdot \sigma$$

$$\Delta\lambda_{m,p}^{meas} = 2\sqrt{3} \cdot \sigma$$

$$R_{m,p}^{meas} = \frac{1}{\Delta\lambda_{m,p}^{meas}} \int R_{\lambda,p} d\lambda$$

where $\lambda_{m,p}^{meas}$ is the effective (centroid) wavelength and σ^2 is the variance. The effective wavelength limits are given by λ_u and λ_l and $\Delta\lambda_{m,p}^{meas}$ is the equivalent square bandwidth. The parameter $R_{m,p}^{meas}$ is the equivalent square-band response for each pixel.

This analysis is repeated for the standardized spectral response functions, using $S_{\lambda,b}$ within the integral, and producing $S_{m,b}$, $\lambda_{m,b}^{std}$ and $\Delta\lambda_{m,b}^{std}$.

2.5 EXO-ATMOSPHERIC SOLAR IRRADIANCE

The exo-atmospheric solar irradiance, $E_{0\lambda}$, model used by MISR is one recommended by the Earth Observing System (EOS) calibration panel. Although the data are published by the World Climate Research Programme10, they are included in the MISR ARP, for reference. Values are reported at 1 astromonical unit (AU).

2.5.1 Measured response weighted exo-atmospheric solar irradiances

The measured total-band weighted solar irradiance, $E_{0,p}^{meas}$ is given by:

$$E_{0,p}^{meas} = \frac{\int\limits_{365}^{1100} E_{0\lambda} R_{\lambda,p} \lambda \; d\lambda}{\int\limits_{365}^{1100} R_{\lambda,p} \lambda \; d\lambda} \qquad (2.13)$$

This irradiance is associated with an equivalent band that is characterized by the moments equations:

$$\lambda_{m,solar,p}^{meas} = \int\limits_{365}^{1100} \lambda \cdot E_{0\lambda} R_{\lambda,p} d\lambda \Big/ \int\limits_{365}^{1100} E_{0\lambda} R_{\lambda,p} d\lambda$$

$$\sigma^2 = \int\limits_{365}^{1100} \lambda^2 \cdot E_{0\lambda} R_{\lambda,p} d\lambda \Big/ \int\limits_{365}^{1100} E_{0\lambda} R_{\lambda,p} d\lambda - (\lambda_{m,solar,p}^{meas})^2$$

$$\lambda_{u,l} = \lambda_{m,solar,p}^{meas} \pm\sqrt{3}\cdot\sigma \qquad (2.14)$$

$$\Delta\lambda_{m,solar,p}^{meas} = 2\sqrt{3}\cdot\sigma$$

These wavelengths are provided for completeness, and are used to reference the wavelengths at which the measured weighted solar irradiances are reported.

2.6 INSTANTANEOUS FIELDS-OF-VIEW

The angular crosstrack and alongtrack instantaneous fields-of-view (IFOV) will be documented at five field positions (pixels) across the array. These data are obtained from the pre-flight ground testing program, and thus include the effects of diffraction and distortion. The IFOVs are expected to be invariant during the flight mission.

Pixel-theta measurements, performed within the Optical Characterization Chamber (OCC), are used to provide IFOV data, as well as other performance descriptors. The test hardware is described in the Appendix, and in the literature[8]. One of two techniques are used for these measurements: (1) a continuous scan, or (2) a stop-and-stare approach. In technique 1 the gimbal scans the pinhole image across the entire CCD array at a prescribed rate. In technique 2 the gimbal is commanded to a discrete set of field angles. Technique 1 generates 1504 measured pointing angles per array but requires a priori knowledge of the camera boresight and EFL. Technique 2 produces about 15 to 20 measured pointing angles per array but requires no a priori knowledge about the camera. Both methods have been shown to produce results that meet the measurement goal which is pointing knowledge to better than a 1/8 of a pixel for all pixels.

The result of the measurement techniques described above is a fifth-order polynomial for each band of each camera at 0, 5, and 10° C (108 total). The polynomial gives the tangent of the pixel crosstrack pointing angle as a function of pixel number. Thus,

$$\tan(\theta)_p = \sum_{i=0,5} c_i \, p^i \qquad (2.15)$$

where p is the pixel number of the pixel of interest and c_i are the coefficients of the fifth-order polynomial. In particular, the boresight of the camera is given by the pixel number that yields $\tan(\theta)=0$.

From these data the following steps are taken to report the IFOVs:

• the pixel values, Z_{ifov}, are determined as those locations where the five downtrack pinhole image scans were made. This information is camera independent, and therefore assumes all cameras were tested at the same field-positions. This assumption is valid to within a few pixels.

• from Eqn. (2.15) the crosstrack IFOV is determined as

$$IFOV_{x,p} = |\,(\theta_{p-1} - \theta_{p+1})\,|\,/2\,. \qquad (2.16)$$

Additionally, the downtrack $IFOV_{d,p}$ is determined from a downtrack scan data. It is defined as the difference in the angles for which the pixel response is half of peak.

2.7 EFFECTIVE FOCAL LENGTHS

EFL is derived from the pixel-theta test described above. The test measures the field angles corresponding to a set of pixels. The camera EFL is defined as the best-fit slope to the relationship $\tan(\theta)$ versus pixel number. Knowing the pixel dimensions, EFL is reported in units of mm.

3. ARP: PREFLIGHT CALIBRATION DATA

The parameters contained within the ARP: Preflight Calibration Data file are given in Table 1.3. The basis for their computation is given in this chapter.

3.1 VERSION NUMBER

It is unlikely that this file will be modified once delivered. A version number will be tracked, however, should this be the case. Version numbers are incremented in sequence. Each of the four ARP files have their own version identifier, so that they might be modified independently of each other. Metadata within the ARP file provide a unique file identifier, published within the Level 1A product.

3.2 IN-BAND WEIGHTED EXO-ATMOSPHERIC SOLAR IRRADIANCES

The in-band weighted solar irradiance, $E_{0,b}{}^{std,in-band}$, over each of the MISR bands is given by:

$$E_0^{std,in-band} = \frac{\int\limits_{in-band} E_{0\lambda}S_\lambda^{in-band}\lambda \; d\lambda}{\int\limits_{in-band} S_\lambda^{in-band}\lambda \; d\lambda} \tag{3.1}$$

where the in-band region is defined as $\lambda_{l,b}{}^{std} < \lambda < \lambda_{u,b}{}^{std}$, $E_{0\lambda}$ is the exo-atmospheric solar spectral irradiance at 1 astronomical unit (AU), and $S_{\lambda,b}{}^{in-band}$ is the standardized spectral response function. The multiplication by λ within the integrals is for the purpose of converting from units of photon counts to energy, as the CCD detectors are photon-recording devices. (It is the product $S\lambda$ that should be considered as the spectral response function.) The irradiance reported by this equation is associated with an equivalent band that is characterized by the moments equations:

$$\lambda_{m,solar}^{std,in-band} = \int\limits_{in-band} \lambda \cdot E_{0\lambda}S_\lambda^{in-band}d\lambda / \int\limits_{in-band} E_{0\lambda}S_\lambda^{in-band}d\lambda$$

$$\sigma^2 = \int\limits_{in-band} \lambda^2 \cdot E_{0\lambda}S_\lambda^{in-band}d\lambda / \int\limits_{in-band} E_{0\lambda}S_\lambda^{in-band}d\lambda - (\lambda_{m,solar}^{std,in-band})^2$$

$$\lambda_{u,l} = \lambda_{m,solar}^{std,in-band} \pm \sqrt{3} \cdot \sigma \tag{3.2}$$

$$\Delta\lambda_{m,solar}^{std,in-band} = 2\sqrt{3} \cdot \sigma$$

These wavelength parameters should be used in the description of any Level 2 data product for which out-of-band correction has been performed.

Values for these parameters are given below, from SDFM#78[71].

Table 3.1. Solar and In-Band Standardized Response Weighted Parameters

Parameter [units]	Band 1 Blue	Band 2 Green	Band 3 Red	Band 4 NIR
$E_{0,}^{std,\ in\text{-}band}$ [W m^{-2} µm^{-1}]	1871.29	1851.30	1524.96	969.64
$\lambda_{m,solar}^{std,\ in\text{-}band}$ [nm]	446.34	557.54	671.75	866.51
$\Delta\lambda_{m,solar}^{std,in\text{-}band}$ [nm]	40.89	27.17	20.44	38.62

3.3 TOTAL-BAND WEIGHTED EXO-ATMOSPHERIC SOLAR IRRADIANCES

The total-band weighted solar irradiance, $E_{0,b}^{std}$ is given by:

$$E_0^{std} = \frac{\int_{365}^{1100} E_{0\lambda} S_\lambda \lambda \ d\lambda}{\int_{365}^{1100} S_\lambda \lambda \ d\lambda} \qquad (3.3)$$

This irradiance is associated with an equivalent band that is characterized by the moments equations:

$$\lambda_{m, solar}^{std} = \int\limits_{365}^{1100} \lambda \cdot E_{0\lambda} S_{\lambda} d\lambda \Big/ \int\limits_{365}^{1100} E_{0\lambda} S_{\lambda} d\lambda$$

$$\sigma^2 = \int\limits_{365}^{1100} \lambda^2 \cdot E_{0\lambda} S_{\lambda} d\lambda \Big/ \int\limits_{365}^{1100} E_{0\lambda} S_{\lambda, b} d\lambda - (\lambda_{m, solar}^{std})^2$$

$$\lambda_{u, l} = \lambda_{m, solar}^{std} \pm \sqrt{3} \cdot \sigma \tag{3.4}$$

$$\Delta\lambda_{m, solar}^{std} = 2\sqrt{3} \cdot \sigma$$

These wavelength parameters should be used in the description of any product for which out-of-band correction has not been performed.

Values for these parameters are given below, from SDFM#78[71].

Table 3.2. Solar and Total Standardized Response Weighted Parameters

Parameter [units]	Band 1 Blue	Band 2 Green	Band 3 Red	Band 4 NIR
E_0^{std} [W m^{-2} μm^{-1}]	1867.27	1842.51	1524.22	977.75
$\lambda_{m, solar}^{std}$ [nm]	447.53	557.85	669.47	857.79
$\Delta\lambda_{m, solar}^{std}$ [nm]	69.53	74.46	91.94	184.19

3.4 SPECTRAL OUT-OF-BAND CORRECTION MATRIX

The out-of-band contribution to the Level 1 total-band weighted radiances can lead to a difference, as compared to in-band weighted radiances, of several percent, at low signal levels[6]. For this reason certain Level 2 data products will make use of an out-of-band correction algorithm [L2Aer ATB]. The algorithm will be of the form:

$$\rho_b^{in-band} = \sum_{i=1,4} c_{ib} \rho_i \tag{3.5}$$

The coefficients c_{ib} are derived in this section.

The in-band equivalent reflectance, $\rho_b^{\text{in-band}}$, is defined to be π times the ratio of the incident radiance, $L_b^{\text{in-band}}$, as weighted by the in-band spectral response function, divided by the in-band weighted exo-atmospheric solar irradiances, $E_{0,b}^{\text{std,in-band}}$. The incident radiance is defined by

$$L_b^{\text{in-band}} = \frac{1}{\int\limits_{\text{in-band}} S_{\lambda,b}\lambda d\lambda} \int\limits_{\text{in-band}} L_\lambda S_{\lambda,b}^{\text{in-band}}\lambda d\lambda \tag{3.6}$$

and $E_{0,b}^{\text{std,in-band}}$ is given by Eqn. 3.1. Thus,

$$\rho_b^{\text{in-band}} = \frac{\pi L_b^{\text{in-band}}}{E_{0,b}^{\text{std,in-band}}} = \frac{\pi}{E_{0,b}^{\text{std,in-band}}} \frac{(L_b - L_b^{\text{out-band}})}{\int\limits_{\text{in-band}} S_{\lambda,b}\lambda d\lambda} \tag{3.7}$$

$$= \frac{1}{E_{0,b}^{\text{std,in-band}} \int\limits_{\text{in-band}} S_{\lambda,b}\lambda d\lambda} \left(\rho_b E_{0,b}^{\text{std}} \int\limits_{\text{total-band}} S_{\lambda,b}\lambda d\lambda - \int\limits_{\text{out-band}} E_{0\lambda}\rho_\lambda S_{\lambda,b}\lambda d\lambda \right)$$

$$\tag{3.8}$$

Here, L_b and $L_b^{\text{out-band}}$ are the radiances integrated, along with with $S_{\lambda,b}\lambda$, over the total-band and out-of-band spectral regions, respectively. Likewise, let E_b^{std} and $E_b^{\text{std,in-band}}$ be exo-atmospheric solar irradiances, integrated (with $S_{\lambda,b}\lambda$) over the total and in-band wavelengths. In addition, it is convenient to make the following definitions:

$$I_b(\lambda_i;\lambda_j) = \int\limits_{\lambda_i}^{\lambda_j} E_{0\lambda} S_{\lambda,b}\lambda d\lambda \text{ , and} \tag{3.9}$$

$$I_b^2(\lambda_i;\lambda_j) = \int\limits_{\lambda_i}^{\lambda_j} E_{0\lambda} S_{\lambda,b}\lambda^2 d\lambda \tag{3.10}$$

$$k_b = \frac{1}{E_{0,b}^{\text{std,in-band}} \int\limits_{\text{in-band}} S_{\lambda,b}\lambda d\lambda} = \frac{1}{E_b^{\text{std,in-band}}} \text{ , and} \tag{3.11}$$

$$\Delta\lambda_{ij} = \lambda_j - \lambda_i . \tag{3.12}$$

The subscripts i and j are band indices 1-4. Also, let $\lambda_{Lb}=\lambda_{l,b}^{std}$, and $\lambda_{Ub}=\lambda_{u,b}^{std}$.

Next, the scene reflectance distribution is approximated by a linear interpolation between the total-band weighted equivalent reflectances, as measured by the four MISR channels. Hence

$$\rho_\lambda = \rho_1 \qquad \text{for } 365 \ \lambda \ \lambda_1$$

$$= \frac{(\rho_{b+1}-\rho_b)}{(\lambda_{b+1}-\lambda_b)}(\lambda-\lambda_b)+\rho_b \qquad \text{for } \lambda_b < \lambda < \lambda_{b+1}$$

$$= \rho_4 \qquad \text{for } \lambda_4 \ \lambda \ 1100 \text{ nm} \qquad (3.13)$$

where λ_b is used as a short hand for $\lambda_{m,solar,b}^{std,in\text{-}band}$, defined as per Eqn. 3.2.

Substituting Eqn. 3.13 into Eqn.3.8, and making use of Definitions 3.9 and 3.10, it can be shown that

Band 1 correction:

$$c_{11} = k_1 \, [E_1^{std} - I(365 \text{ nm};\lambda_{L1}) + \Delta\lambda_{21}^{-1} \, I^2(\lambda_{U1};\lambda_2) - (1+\lambda_1 \Delta\lambda_{21}^{-1}) \, I(\lambda_{U1};\lambda_2)]$$

$$c_{21} = k_1 \, [-\Delta\lambda_{21}^{-1} \, I^2(\lambda_{U1};\lambda_2) + \lambda_1 \Delta\lambda_{21}^{-1} \, I(\lambda_{U1};\lambda_2) + \Delta\lambda_{32}^{-1} \, I^2(\lambda_2;\lambda_3) - (1+\lambda_2 \Delta\lambda_{32}^{-1}) \, I(\lambda_2;\lambda_3)]$$

$$c_{31} = k_1 \, [-\Delta\lambda_{32}^{-1} \, I^2(\lambda_2;\lambda_3) + \lambda_2 \Delta\lambda_{32}^{-1} \, I(\lambda_2;\lambda_3) + \Delta\lambda_{43}^{-1} \, I^2(\lambda_3;\lambda_4) - (1+\lambda_3 \Delta\lambda_{43}^{-1}) \, I(\lambda_3;\lambda_4)]$$

$$c_{41} = k_1 \, [-\Delta\lambda_{43}^{-1} \, I^2(\lambda_3;\lambda_4) + \lambda_3 \Delta\lambda_{43}^{-1} \, I(\lambda_3;\lambda_4) - I(\lambda_4;1100 \text{ nm})]$$

Band 2 correction:

$$c_{12} = k_2 \, [- I(365 \text{ nm};\lambda_1) + \Delta\lambda_{21}^{-1} \, I^2(\lambda_1;\lambda_{L2}) - (1+\lambda_1 \Delta\lambda_{21}^{-1}) \, I(\lambda_1;\lambda_{L2})]$$

$$c_{22} = k_2 \, [E_2^{std} -\Delta\lambda_{21}^{-1} \, I^2(\lambda_1;\lambda_{L2}) + \lambda_1 \Delta\lambda_{21}^{-1} \, I(\lambda_1;\lambda_{L2}) + \Delta\lambda_{32}^{-1} \, I^2(\lambda_{U2};\lambda_3) - (1+\lambda_2 \Delta\lambda_{32}^{-1}) \, I(\lambda_{U2};\lambda_3)]$$

$$c_{32} = k_2 \, [-\Delta\lambda_{32}^{-1} \, I^2(\lambda_{U2};\lambda_3) + \lambda_2 \Delta\lambda_{32}^{-1} \, I(\lambda_{U2};\lambda_3) + \Delta\lambda_{43}^{-1} \, I^2(\lambda_3;\lambda_4) - (1+\lambda_3 \Delta\lambda_{43}^{-1}) \, I(\lambda_3;\lambda_4)]$$

$$c_{42} = k_2 \, [-\Delta\lambda_{43}^{-1} \, I^2(\lambda_3;\lambda_4) + \lambda_3 \Delta\lambda_{43}^{-1} \, I(\lambda_3;\lambda_4) - I(\lambda_4;1100 \text{ nm})]$$

Band 3 correction:

$$c_{13} = k_3 [- I(365 \text{ nm};\lambda_1) + \Delta\lambda_{21}^{-1} I^2(\lambda_1;\lambda_2) - (1+\lambda_1 \Delta\lambda_{21}^{-1}) I(\lambda_1;\lambda_2)]$$

$$c_{23} = k_3 [-\Delta\lambda_{21}^{-1} I^2(\lambda_1;\lambda_2) + \lambda_1 \Delta\lambda_{21}^{-1} I(\lambda_1;\lambda_2) + \Delta\lambda_{32}^{-1} I^2(\lambda_2;\lambda_{L3}) - (1+\lambda_2 \Delta\lambda_{32}^{-1}) I(\lambda_2;\lambda_{L3})]$$

$$c_{33} = k_3 [E_3^{std} -\Delta\lambda_{32}^{-1} I^2(\lambda_2;\lambda_{L3}) + \lambda_2 \Delta\lambda_{32}^{-1} I(\lambda_2;\lambda_{L3}) + \Delta\lambda_{43}^{-1} I^2(\lambda_{U3};\lambda_4) - (1+\lambda_3 \Delta\lambda_{43}^{-1}) I(\lambda_{U3};\lambda_4)]$$

$$c_{43} = k_3 [-\Delta\lambda_{43}^{-1} I^2(\lambda_{U3};\lambda_4) + \lambda_3 \Delta\lambda_{43}^{-1} I(\lambda_{U3};\lambda_4) - I(\lambda_4;1100 \text{ nm})]$$

Band 4 correction:

$$c_{14} = k_4 [- I(365 \text{ nm};\lambda_1) + \Delta\lambda_{21}^{-1} I^2(\lambda_1;\lambda_2) - (1+\lambda_1 \Delta\lambda_{21}^{-1}) I(\lambda_1;\lambda_2)]$$

$$c_{24} = k_4 [-\Delta\lambda_{21}^{-1} I^2(\lambda_1;\lambda_2) + \lambda_1 \Delta\lambda_{21}^{-1} I(\lambda_1;\lambda_2) + \Delta\lambda_{32}^{-1} I^2(\lambda_2;\lambda_3) - (1+\lambda_2 \Delta\lambda_{32}^{-1}) I(\lambda_2;\lambda_3)]$$

$$c_{34} = k_4 [-\Delta\lambda_{32}^{-1} I^2(\lambda_2;\lambda_3) + \lambda_2 \Delta\lambda_{32}^{-1} I(\lambda_2;\lambda_3) + \Delta\lambda_{43}^{-1} I^2(\lambda_3;\lambda_{L4}) - (1+\lambda_3 \Delta\lambda_{43}^{-1}) I(\lambda_3;\lambda_{L4})]$$

$$c_{44} = k_4 [E_4^{std} -\Delta\lambda_{43}^{-1} I^2(\lambda_3;\lambda_{L4}) + \lambda_3 \Delta\lambda_{43}^{-1} I(\lambda_3;\lambda_{L4}) - I(\lambda_{U4};1100 \text{ nm})].$$

Values for these parameters are given below, from SDFM#78B[71].

Table 3.3. Out-of-band correction matrix

Parameter [units]	Band 1 Blue	Band 2 Green	Band 3 Red	Band 4 NIR
c_{ib} [none]	1.01055e+00	-7.98322e-03	-6.02825e-03	-4.81379e-03
	-5.71698e-03	1.02004e+00	-4.81411e-03	-3.29545e-03
	-3.77674e-03	-8.64212e-03	1.01446e+00	-1.36208e-02
	-1.05971e-03	-3.41470e-03	-3.61692e-03	1.02173e+00

Note that if one refers to Eqn. 3.5 we see that the coefficients in column 1 (not row 1) are used to derive the in-band radiance for Band 1, blue.

3.5 POINT SPREAD FUNCTIONS

The point-spread functions (PSF) are provided from the pinhole image crosstrack scans (see Section 2.6). They are normalized such that the integrated area under the PSF curves is unity. A careful screening of the data was made prior to selection of the response profiles, to insure the gimbal is scanning along the cross-track axes. A single PSF response profile wase selected for each pixel, based upon these scans. Anomalous profiles were deleted, then all measurements averaged to provide a single profile per channel. From these PSFs, provided for 1x1 resolution mode, 2 consecutive PSF samples (for 2x2 resolution), and 4 consecutive pixels (for 4x4 resolution) were averaged to provide the parameters for the other averaging modes. Because the PSFs are one dimensional, the profile for the 1x4 resolution mode is the same as the 1x1 profile. These derived PSF functions are also normalized to unity.

3.6 PSF DECONVOLUTION KERNELS

Deconvolution of the L1B1 data product is performed in order to remove the effects of slight blurring due to the sensors' PSF response. The measured line array image can be represented, in theory, as a 1-dimensional convolution of the ideal image with the PSF. Conversely, the enhanced image can be obtained as a convolution of the measured image with a kernel which is derived from the PSF.

The equation used to obtain the enhanced image is found in the [L1 ATB, Rev. E, Section 3.4.5.2]:

$$f(x_k) = \sum_{i=k-j}^{k+j} g(x_i)d(x_i-x_k) \qquad k = 1, ..., N$$

(3.14)

Here f represents the enhanced image, g the measured image, and d the deconvolution kernel. The deconvolution kernels are derived by Fourier transforming the PSF's, taking the mathematical inverse of the resulting function, inverse Fourier transforming back to the spatial domain, and taking the real part of the result. Because the PSF's are nearly symmetric, the imaginary parts of the deconvolution functions are negligible and reasonably ignored. Mathematically, this process is expressed as follows, letting a represent the PSF:

$$d = \text{Real}\left\{ F^{-1}\left[\frac{1}{F[a]} \right] \right\}$$

(3.15)

where F denotes the Fourier transform and F^{-1} denotes the inverse transform. This approach to deconvolution is often not attempted because the Fourier transform of the PSF in general may have zero crossings, in which case taking the mathematical inverse would result in singularities. Fortunately, each of the MISR camera PSF's is well-behaved in the regard and this situation does not occur; the deconvolution functions are well-defined, therefore making this approach feasible.

In practice, a numerical Fast Fourier Transform (FFT) algorithm is used to calculate the deconvolution kernels. The FFT requires the number of samples in the function being transformed to be a power of 2. Since the PSF's for the 1x1 (and 1x4), 2x2, and 4x4 averaging modes of MISR are 51, 25, and 13 samples wide, respectively, 64-element arrays were used in the FFT process and elements beyond the range of the PSF's were filled with 0. Because the wings of the PSF's drop to very low values this leads to a negligible discontinuity at the PSF edges and no consequent ill effects in the transformed functions.

After the inverse FFT is applied and the real part taken, the result data are truncated to a width, in samples, equivalent to the width of the input PSF. Thus, the deconvolution kernels also have widths of 51, 25, and 13 samples for the various averaging modes. As a final step, the deconvolution functions are normalized by the sum of values over all samples, to insure that the area under each kernel is unity.

Verification of the numerical accuracy of the deconvolution kernels was performed by convolving the deconvolution kernels with the corresponding original PSF's. In each case, delta functions (the expected result) were obtained to a very high degree of accuracy.

Image restorations often make use of the estimated noise power spectrum to effect a degree of smoothing in the result. The above discussion has ignored the effects of noise in the image modeling equations, and no smoothing is incorporated into the algorithm. We believe this is justified by the high signal-to-noise ratio of the MISR cameras. However, since the deconvolution process is basically an image-sharpening process, the magnitude of random noise in the restored image will be larger than in the unrestored data, even in images of uniform targets. This will result in some loss of signal-to-noise ratio, but since the MISR cameras have such high SNR to begin with and the blur PSF's are to first order close to delta functions this is not deemed a significant problem. Nevertheless, this fact requires the deconvolution process to be tested on samples of calibration imagery of the instrument's deployable Spectralon panels obtained on orbit, in order to compare SNR before and after deconvolution. From such measurements, correction factors for SNR can be derived and applied, if necessary, to SNR ratios reported in the ARP.

3.7 PAR INTEGRATION WEIGHTS

During Level 2 processing, certain geophysical properties (bi-hemispherical reflectance and directional hemispherical reflectance) are spectrally integrated over the photosynthetically active radiation (PAR) regime (400 - 700 nm). This is accomplished by generating estimates of this integral using the values retrieved in the blue, green, and red bands, and then computing weighted sums of these spectral values. This section provides the derivation of these integration weights.

Assume that we want to integrate spectral reflectance, ρ_λ, from 400 to 700 nm. Let ρ_1, ρ_2, and ρ_3 denote the values in the blue, green, and red bands respectively, making the simplification that these are monochromatic values at the MISR band-center wavelengths. Next, assume a piecewise linear variation in ρ_λ over the 400 - 700 nm region, i.e.:

$$\rho_\lambda = \rho_1, \qquad\qquad\qquad 400 \; \lambda \; \lambda_1$$

$$\rho_\lambda = \rho_1 + (\lambda - \lambda_1)(\rho_2 - \rho_1)/(\lambda_2 - \lambda_1), \qquad\qquad \lambda_1 \; \lambda \; \lambda_2$$

$$\rho_\lambda = \rho_2 + (\lambda - \lambda_2)(\rho_3 - \rho_2)/(\lambda_3 - \lambda_2), \qquad\qquad \lambda_2 \; \lambda \; \lambda_3$$

$$\rho_\lambda = \rho_3, \qquad\qquad\qquad \lambda_3 \; \lambda \; 700$$

where λ_1, λ_2, and λ_3 represent the band center wavelengths of the three bands, represented by the in-band center wavelengths calculated from a moments analysis of the standardized spectral profiles weighted by the exo-atmospheric solar irradiance, i.e. $\lambda_{m,solar,b}^{std-in-band}$, with b=1,2,3.

Now, let

$$(3.16)$$

$$S_1 = \int_{400}^{\lambda_1} E_{0\lambda} d\lambda \qquad\qquad S_2 = \int_{\lambda_1}^{\lambda_2} E_{0\lambda} d\lambda \qquad\qquad S_3 = \frac{1}{(\lambda_2 - \lambda_1)} \int_{\lambda_1}^{\lambda_2} (\lambda - \lambda_1) E_{0\lambda} d\lambda$$

$$S_4 = \int_{\lambda_2}^{\lambda_3} E_{0\lambda} d\lambda \qquad\qquad S_5 = \frac{1}{(\lambda_3 - \lambda_2)} \int_{\lambda_2}^{\lambda_3} (\lambda - \lambda_2) E_{0\lambda} d\lambda \qquad\qquad S_6 = \int_{\lambda_3}^{700} E_{0\lambda} d\lambda$$

Then

$$\int_{400}^{700} \rho_\lambda E_{0\lambda} d\lambda = (S_1 + S_2 - S_3)\rho_1 + (S_3 + S_4 - S_5)\rho_2 + (S_5 + S_6)\rho_3 \qquad (3.17)$$

and if we define

$$w_1 = S_1 + S_2 - S_3 \qquad\qquad w_2 = S_3 + S_4 - S_5 \qquad\qquad w_3 = S_5 + S_6 \qquad (3.18)$$

and then normalize these such that

$$PAR_1 = \frac{w_1}{w_1 + w_2 + w_3} \qquad PAR_2 = \frac{w_2}{w_1 + w_2 + w_3} \qquad PAR_3 = \frac{w_3}{w_1 + w_2 + w_3} \qquad (3.19)$$

then the normalized weights provide the required inputs to the Level 2 spectral integration algorithm (see [L2 Surf ATB]).

Values for these parameters are given below, from SDFM#78A[71].

Table 3.4. PAR values

Parameter [units]	Band 1 Blue	Band 2 Green	Band 3 Red	Band 4 NIR
PAR_b [none]	0.355996	0.388044	0.255960	---

4. ARP: IN-FLIGHT CALIBRATION DATA

The parameters contained within the ARP: In-flight Calibration Data file are to be updated throughout the MISR mission. Data from the On-Board Calibrator (OBC), Vicarious calibration experiments, and image techniques (such as Histogram Equilization) are utilized to provide the sensor response determination. The complete set of parameters to be recomputed have been given in Table 1.4; the basis for their computation is given in this chapter. Background information on detector responsivity theory is additionally provided in Appendix A.

We discuss each of the ARP and calibration report deliverables, in turn, in the sections below.

4.1 VERSION NUMBER AND REVISION NUMBER

Version numbers will be used to track format or layout changes for the ARP. Should the parameter fields be changes in size or kinds of parameters, a version number will be incremented. Version numbers are incremented in sequence. Each of the four ARP files have their own version identifier, so that they might be modified independently of each other. Changes in data values are allowed under the same version number, as the revision numbers distinguish one file from the next.

Revision numbers will track changes in the value of a data parameter, due to processing or algorithm errors. Should an error be found in a particular value of a data parameter, the corrected file will have a new revision number, and the applicable version number will be unchanged from the previous revision.

Neither the version number, nor the revision numbers will be incremented routinely from one calibration experiment to the next. The ARP file name and the calibration date parameter will be used to distinguish files representing different calibration experiments.

4.2 CALIBRATION DATE

The calibration date will identify the date at which the calibration experiment was conducted.

Level 1B data processing will never be delayed due to the lack of a calibration file for a specific date. Newly acquired data will be converted using the last received ARP calibration parameters. It is assumed that calibration experiments are conducted monthly, and that a new ARP is delivered within 30 days of this experiment. Thus, science data products never have to use an ARP that is more than 30 days old.

Should Level 1B data processing be delayed for more than a month, or should reprocessing be requested, the most recently delivered ARP should not be used. Rather, one that has a calibration date no earlier than 31 days from the science data acquisition date should be used.

Should the EOS and MISR projects decide to reprocess data, the files representing the updated version and revisions should be used, and not necessarilty the files used in the first round of processing.

4.3 RADIOMETRIC GAIN COEFFICIENTS

We begin this section by providing a flow diagram for the gain coefficient determinations, as implemented by our processing code. This, Fig. 4.1, will serve to provide an overview to the material which follows.
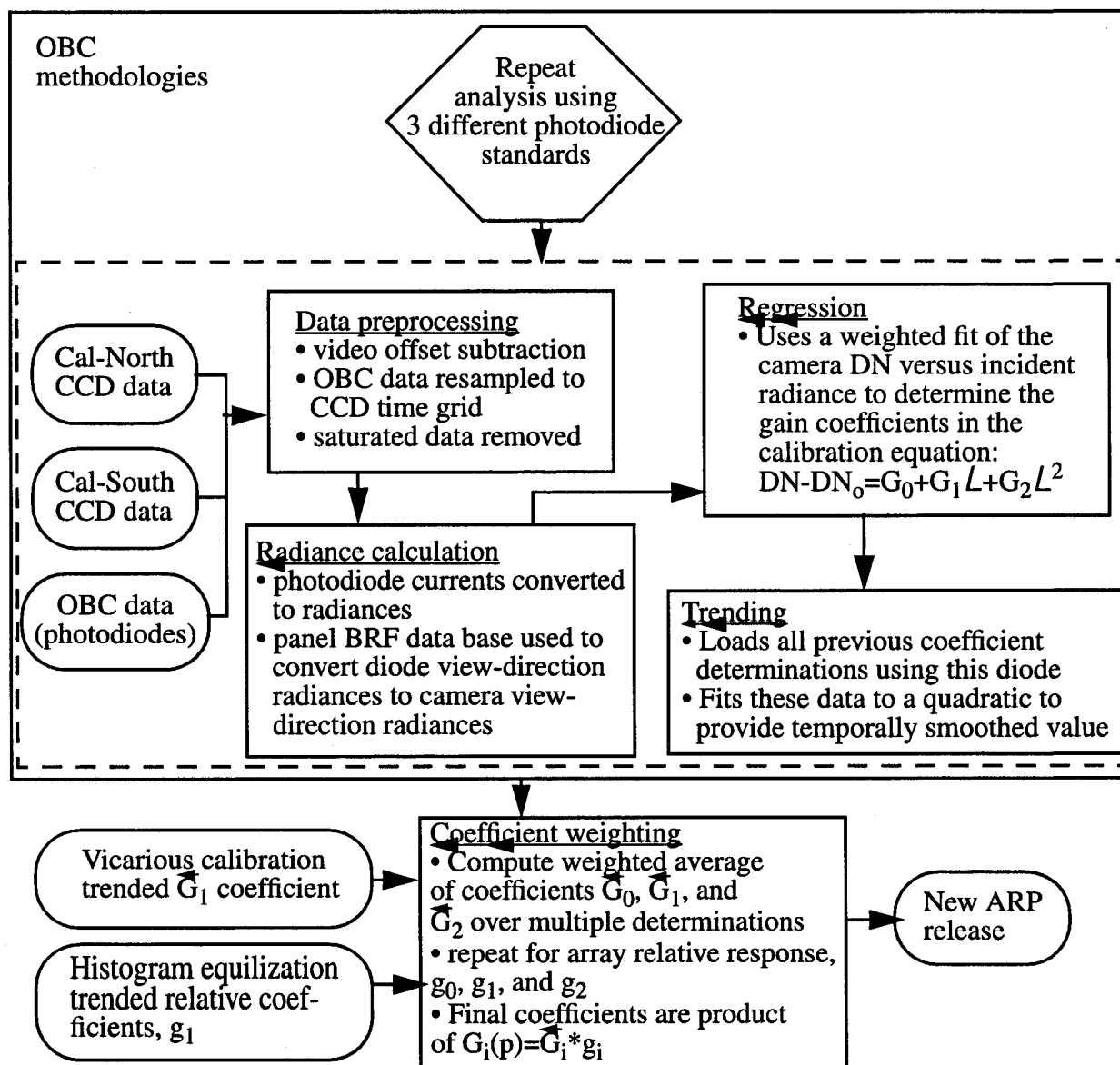
Figure 4.1. Gain coefficient process flow

4.3.1 OBC calibration experiment

MISR has developed data acquisition modes known as Cal-North, Cal-South, Cal-Dark, and Cal-diode (discussed in [IFRCC Plan]). These are used for instrument calibration and characterizations. The in-flight calibration of the MISR cameras is provided, in one methodology, by the On-Board Calibrator (OBC), and data from Cal-North and Cal-South. Needed inputs to this process include camera CCD calibration data (DN and data time tags), during view of the deployed calibration panel, currents from the flight photodiodes (for the same time period), and the preflight diffuse panel characterization data. Camera, photodiode data, and time tags are provided to the SCF processing center via the Level 1A product, obtained from the DAAC. Figure

4.2 shows this data routing plan. Time tags are used to correlate the CCD and photodiode data, and to determine the solar angle onto the diffuse panels.
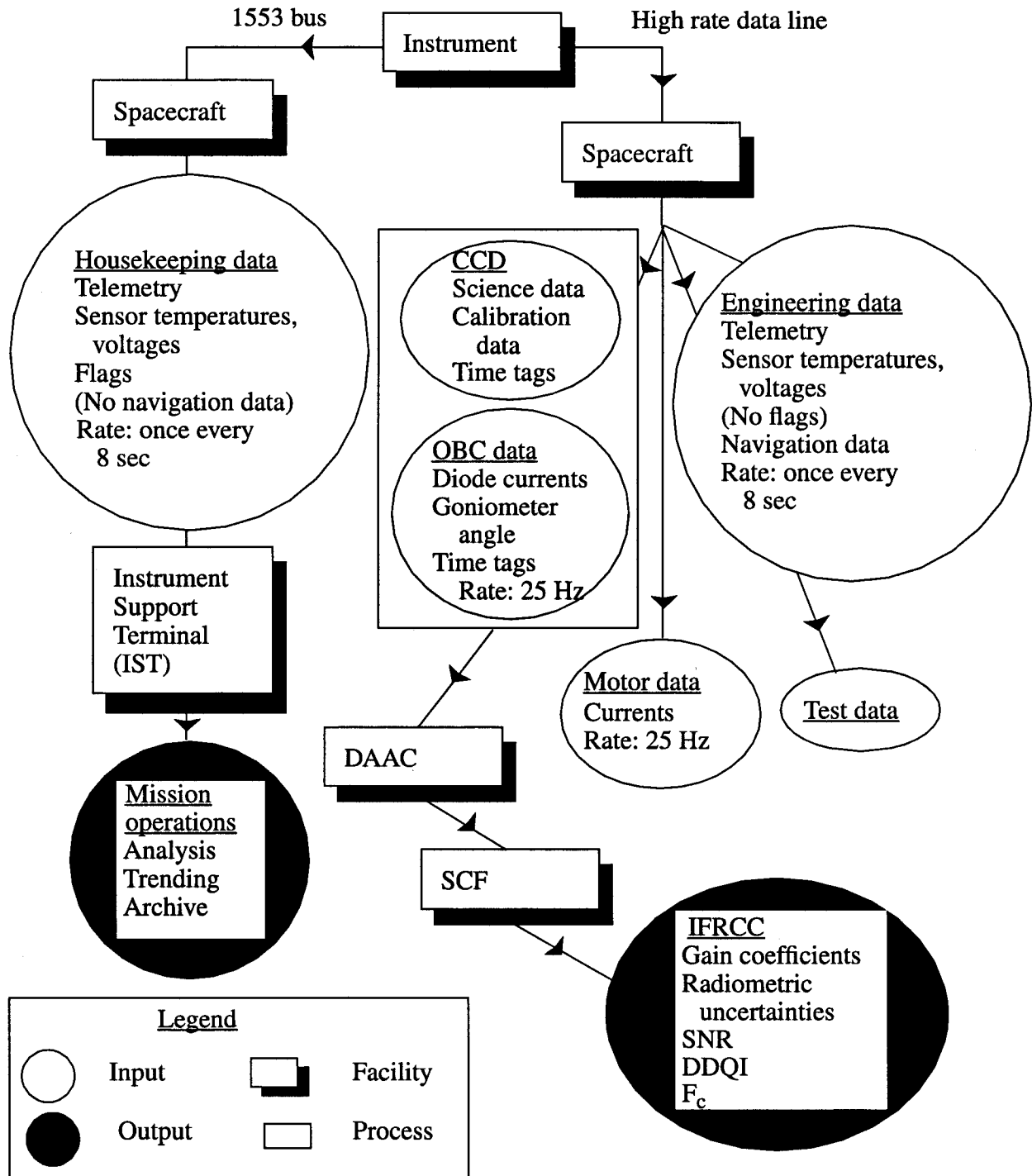
Figure 4.2. Sources of data for OBC calibration methodology

The OBC consists of six sets of flight photodiodes; each set is composed of four detector units, filtered to the four MISR wavelengths. One photodiode set is mounted to a goniometer, used to monitor panel BRF stability with time. A pair of deployable Spectralon diffuse panels

completes the OBC. Monthly, the panels are deployed to reflect sunlight into the cameras. The flight photodiodes determine the panel reflected radiances, and the panel bi-directional reflectance factor (BRF) data base is used to convert these to camera-incident radiances.

Using these information we desire to establish the relationship:

$$(DN - DN_o) = G_0 + G_1 L^{std} + G_2(L^{std})^2 \qquad (4.1)$$

where

L^{std} is the incoming spectral radiance weighted by the standardized spectral response [W m^{-2} μm^{-1} sr^{-1}];

$DN - DN_0$ is the offset subtracted sensor digital number output [DN];

G_0 is the detector gain coefficient [DN];

G_1 is the detector gain coefficient [(W m^{-2} μm^{-1} sr^{-1})$^{-1}$ DN]; and

G_2 is the detector gain coefficient [(W m^{-2} μm^{-1} sr^{-1})$^{-2}$ DN].

It is understood that each of the coefficients G_0, G_1, and G_2 are specified per camera, band, and pixel. These dependencies are omitted in our notation for simplicity.

4.3.1.1 Multiple OBC photodiode standards

For processing of data from the calibration experiment, each gain coefficient determination made with a different photodiode standard is considered a different methodology. Three methodologies are to be utilized. An exception is that for the nadir camera, data are considered which have been acquired over both the north and south poles. Thus, for this camera, six OBC methodologies are to be reconciled. This default operational approach is listed in the table below.

For the purpose of computing signal-to-noise ratio, data quality indices, or the channel operability flag, it suffices to utilize radiance values as computed from a single photodiode. The -y-PIN-2 photodiode is considered the baseline choice for these analysis.

Table 4.1. OBC multiple methodologies.

Camera	Method 1	Method 2	Method 3	Method 4	Method 5	Method 6
Df	Cal-South, -y-PIN-2	Cal-South, HQE	Cal-South, Df-PIN-3			
Cf						
Bf			Cal-South, +y-PIN-1			
Af						
An				Cal-North, -y-PIN-2	Cal-North, HQE	Cal-North, +y-PIN-1
Aa	Cal-North, -y-PIN-2	Cal-North, HQE	Cal-North, +y-PIN-1			
Ba						
Ca			Cal-North, Da-PIN-4			
Da						

4.3.2 Data preprocessing

As suggested by Figs. 4.1 and 4.2, the data acquired during the Cal-North and Cal-South operating modes are collected and delivered to the SCF. The first steps taken in preparing the data are to delete all saturated data, and resample the photodiode data to the CCD time stamps, using a linear interpolation (verify). This resampling is done independently for each photodiode and spectral band. Thus, a data loss in one data set does not degrade the quality of the experiments for the other bands. <== Is a spline fit done, or simply a linear interpolation over the nearest neighbor OBC points?

Operationally, CCD data which have no corresponding photodiode data, within ??? msec, are deleted.

4.3.3 Flight photodiode standards

Data from the flight diodes are used to measure the panel reflected radiances. Signals from these photodiodes are digitized by the instrument. For each of the 24 photodiode channels, the relationship between current and voltage is 8×10^{-9} A/V. Further, the analog-to-digital gain is set to 6/16383 V/DN. With these multipliers we know the relationship between diode DN and current is given as

$$i[\text{nAmps}] = (\text{DN } [\text{DN}]) / 341.3125 \ [\text{nAmps}^{-1} \text{ DN}] \qquad (4.2)$$

with a maximum allowable current of 48 nAmps.

It is particularly important that radiances measured by the p-i-n intrinsic layer doped photodiode (PIN) flight photodiodes be corrected for out-of-band response. Although the MISR cameras and photodiodes utilize filters of the same design, their specific mounting configurations cause different out-of-band response, due to poor out-of-band blocking at oblique angles to the filter. This effect was noticed during Engineer Model testing[11]. Knowledge of the photodiode spectral response function is first used to compute the diode-measured radiance at wavelength λ^{std}:

$$L^{std, OBC} = \frac{1.2395 \ i \ E_0^{std} \ W \ \mu m \ Amps^{-1}}{A\Omega \int\limits_{200}^{1200} E_{0\lambda} R_\lambda^{OBC} \lambda d\lambda} \quad , \tag{4.3}$$

where

$L^{std,OBC}$	equals the spectral radiance measured by the OBC photodiode at wavelength λ^{std}
$E_{o\lambda}$	is the spectral exo-atmospheric solar irradiance function
E_0^{std}	equals the exo-atmospheric solar irradiance, at wavelength λ^{std}
$A\Omega$	is the area*solid angle product for the photodiode
R_λ^{OBC}	is the spectral response function of the OBC flight photodiode
λ^{std}	is a shorthand notation for $\lambda_{m,solar}^{std}$ which is an ARP preflight calibration file parameter

This equation is motivated by the fact that the Spectralon diffuse panel has a constant reflectance with wavelength across any given spectral band. Thus, the diffuse panel reflected radiance has the same spectral shape as the exo-atmospheric solar irradiance.

Next, it is necessary to convert these radiances into values that are band-weighted over the camera spectral response. Using the relationships:

$$L^{std} = \frac{\int L_\lambda S_\lambda \lambda d\lambda}{\int S_\lambda \lambda d\lambda} \quad , \tag{4.4}$$

with

L_λ	a radiance versus wavelength distribution (here, that incident onto the photodiode);
S_λ	the standardized spectral response function;

$$L_\lambda = \frac{L^{std,OBC} E_{0\lambda}}{E_0^{std}} \; ; \qquad (4.5)$$

$$E_0^{std} = \frac{\int_{200}^{1200} E_{0\lambda} S_\lambda \lambda d\lambda}{\int_{200}^{1200} S_\lambda \lambda d\lambda} \; ; \qquad (4.6)$$

and

E_0^{std} the exo-atmospheric solar irradiance, as integrated over the MISR standardized response profile.

In conjunction with Eqn. 4.3, we have

$$L^{std,OBC} = \frac{1.2395 \; i \; W \; \mu m \; Amps^{-1}}{A\Omega} \frac{E_0^{std}}{\int_{200}^{1200} E_{0\lambda} R_\lambda^{OBC} \lambda d\lambda} \qquad (4.7)$$

where

$L^{std,OBC}$ is the MISR-band weighted radiance measured by the diodes.

The radiance given in the above equation has yet to be corrected for diffuse panel BRF effects. This is needed in order to determine the radiance reflected into each of the cameras to be calibrated.

The diode names and response values are provided in Table 4.2, as taken from SDFM#168[78] and DFM#995[70]. Recalling that the solid angle is the ratio of an area on a sphere to the square of the radius of the sphere, and that this area can be approximated as the flat base of the cone, πr_b^2, the diode $A\Omega$ products have been computed using the equation:

$$A\Omega = \frac{(\pi r_b r_d)^2}{(r_b^2 + d^2)} \qquad (4.8)$$

where

r_b is the diameter of the field-limiting diode baffle (outer baffle) [m]

r_d is the diameter of the diode baffle (inner baffle) [m]

d is the distance between the baffles [m]

$A=\pi r_d^2$, diode area

r_d, diode radius

$\Omega \sim \pi r_b^2/(r_b^2+d^2)$, diode solid angle [sr]

$\theta=\arctan(r_b/d)$, diode full angle [degrees]
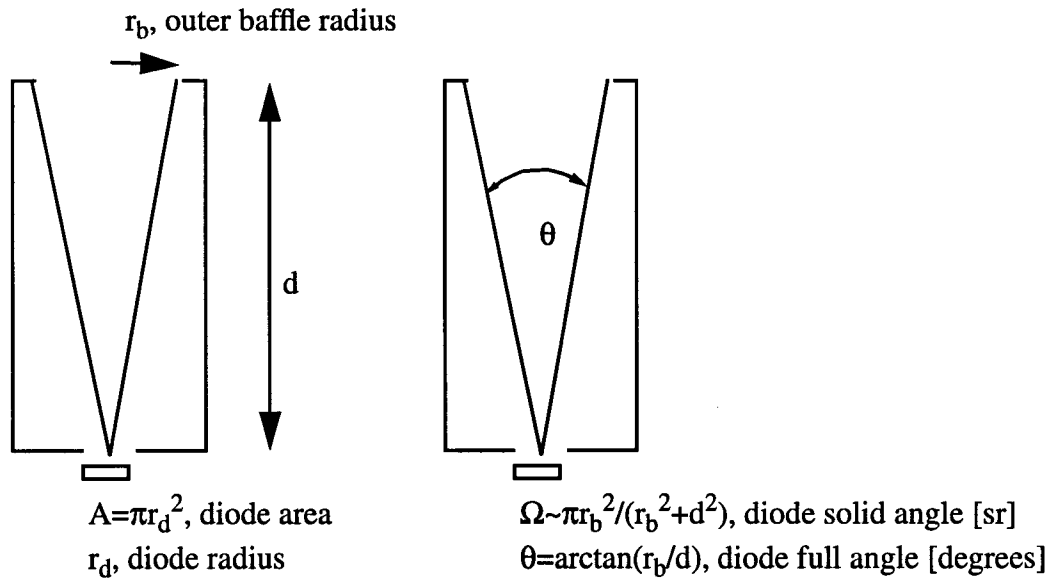
Figure 4.3. Photodiode dimensions

The values of r_b, r_d, and d are given in DFM#952[67]. (Note in DFM#952 Table 2 is erroneously labeled "radius", as it is the baffle diameters that are given. Also, our values of the $A_{diode}\Omega$ have been recomputed here, as the term of r_d^2 in the denominator of Eqn. 2 should be deleted). The last column in Table 4.2 represents the denominator of Eqn. 4.7.

Table 4.2. Flight diode designations

Science name		Part number identifier	$A_{diode}\Omega$, m^2 sr	Full angle, degrees	Response integral, $W\ m^{-2}\ \mu m$
Location	Spectral band				
HQE	Blu	343-1	7.4541E-09	1.971E+00	17.324
HQE	Grn	325-2	7.4495E-09	1.971E+00	11.657
HQE	Red	336-3	7.4719E-09	1.971E+00	12.518
HQE	NIR	311-4	7.4730E-09	1.971E+00	16.181

Table 4.2. Flight diode designations

Science name		Part number identifier	$A_{diode}\Omega$, m^2 sr	Full angle, degrees	Response integral, $W\ m^{-2}\ \mu m$
Location	Spectral band				
+y-PIN-1 (+y edge)	Blu	103-1	1.4806E-08	2.017E+00	13.070
	Grn	103-2	1.4829E-08	2.018E+00	14.353
	Red	103-3	1.4755E-08	2.017E+00	8.757
	NIR	103-4	1.4653E-08	2.017E+00	11.422
-y-PIN-2 (closest to center)	Blu	261-1	1.4803E-08	2.017E+00	13.010
	Grn	261-2	1.4813E-08	2.017E+00	14.951
	Red	261-3	1.4766E-08	2.017E+00	8.772
	NIR	261-4	1.4674E-08	2.017E+00	12.168
Df-PIN-3 (-x side)	Blu	185-1	1.4786E-08	2.017E+00	11.701
	Grn	185-2	1.4793E-08	2.017E+00	12.396
	Red	185-3	1.4738E-08	2.017E+00	12.097
	NIR	185-4	1.4623E-08	2.017E+00	11.724
Da-PIN-4 (+x side)	Blu	216-1	1.4752E-08	2.017E+00	16.057
	Grn	216-2	1.4783E-08	2.017E+00	15.558
	Red	216-3	1.4786E-08	2.017E+00	10.810
	NIR	216-4	1.4783E-08	2.017E+00	11.696
G-PIN (-y side)	Blu	237-1	1.4796E-08	2.018E+00	12.682
	Grn	237-2	1.4830E-08	2.018E+00	14.209
	Red	237-3	1.4806E-08	2.017E+00	11.141
	NIR	237-4	1.4779E-08	2.016E+00	10.988

The value of E_0^{std}, also utilized by Eqn. 4.7, is found in Table 3.2.

4.3.4 Panel bidirectional reflectance factor correction

The calibration algorithm next makes use of the bi-directional reflectance factor (BRF) for Spectralon, as measured preflight. This function is used to convert the radiance directed towards the photodiodes to a measure of the panel-reflected radiances in the camera-view angle directions.

A two-dimensional, second-order polynomial fit to the BRF data is used for data interpolation. The panels are considered spatially uniform, and isotropic (rotationally symmetric). As laboratory data were acquired using a laser-based system, BRF data for two incident angles of polarization are averaged. (MISR is insensitive to the incident angle of polarization, hence the two components of the panel-reflected field are not required separately). A description of this data base is found in Bruegge, et. al.[3].

The radiance measured by each photodiode is in response to a field directed towards the photodiode boresight, $(\theta_r^{OBC}, \phi_r^{OBC})$. BRF changes within the photodiode field-of-view are negligible, as demonstrated by SDFM#168[78]. Using the flight photodiode radiances, provided by Eqn. 4.7, and our Spectralon BRF data, camera incident radiances are next provided unique to each pixel, knowing the camera pixel view-angle with respect to the panel:

$$L^{std}(\theta_i, \phi_i; \theta_r^p, \phi_r^p) = L^{std, OBC}(\theta_i, \phi_i; \theta_r^{OBC}, \phi_r^{OBC}) \cdot \frac{BRF(\theta_i, \phi_i; \theta_r^p, \phi_r^p)}{BRF(\theta_i, \phi_i; \theta_r^{OBC}, \phi_r^{OBC})} \qquad (4.9)$$

where

θ_i, ϕ_i are the incident zenith and azimuth angles, respectively, with respect to the panel normal

$\theta_r^{OBC}, \phi_r^{OBC}$ are the reflected zenith and azimuth angles, respectively, as viewed by a given OBC photodiode

θ_r^p, ϕ_r^p are the reflected zenith and azimuth angles, respectively, as viewed by a given detector element, p

BRF   is the preflight-determined bidirectional reflectance function of the diffuse panel

4.3.5 Radiance verification

As a verification on our system, we compute the radiance reflected into a given camera pixel independent of the photodiodes. This approach is less accurate, in that in does not account for panel reflectance degradation. The equation involved is simply:

$$L^{std}(\theta_i, \phi_i; \theta_r^p, \phi_r^p) = E_o^{std} \cdot \cos(\theta_i) \cdot BRF(\theta_i, \phi_i; \theta_r^p, \phi_r^p)/\pi \ . \qquad (4.10)$$

We wish to compare these radiances to those derived from Eqns. 4.7 and 4.9.

This verification algorithm has not been yet been implemented in our processing code (but has been submited as ClearTrack lien number 603).

4.3.6 Coordinate systems

In order to determine the angles required in Eqn. 4.9, the calibration algorithms must make transformations from spacecraft, instrument, camera, detector, and panel coordinate systems. These must all be converted to angles within the laboratory coordinate system used to measure the panels; the BRF data base is published in this as-measured format.

These coordinate systems are described in the following paragraphs. References for this section include the [FDR] document, DFM#932[60], DFM#963[69], and SDFM#106[72].

4.3.6.1 Spacecraft coordinate system

The spacecraft coordinate system (SCS) is imbedded in and fixed relative to the spacecraft structure. In the nominal flight attitude, the longitudinal axis of the spacecraft in the velocity direction is defined as the +X axis. The axis perpendicular to the X-axis and parallel to the plane of the spacecraft in the anti-Sun direction is defined as the +Y-axis. The +Z axis is defined as the right-hand cross-product of the X-axis and Y-axis, nominally nadir.

4.3.6.2 Instrument coordinate system

The instrument coordinate system (ICS) is imbedded in and fixed relative to the instrument structure. A right-handed instrument coordinate system is defined which is fixed relative to the MISR optical bench. Each axis is nominally aligned parallel to the corresponding axis of the spacecraft coordinate system, though misalignments between the two coordinate systems may arise as a result of the fabrication, integration, or orbital thermal effects.

The ICS is illustrated in Fig. 4.4. The +X direction is the velocity direction, the +Z nominally points to earth, and the -Y hemisphere includes the Sun. The Earth's rotation during the instrument transit from North Pole (NP) to the South Pole (SP) is also shown. Each MISR camera boresight is defined, relative to the nadir direction, by the rotation angles δ and β. Forward (aft) cameras have negative (positive) δ and positive (negative) β angles. Since the rotations are finite the rotation order is important. The MISR camera boresights are defined by first performing a rotation on a unit vector in the nadir direction about the X axis by δ and then around Y by β.
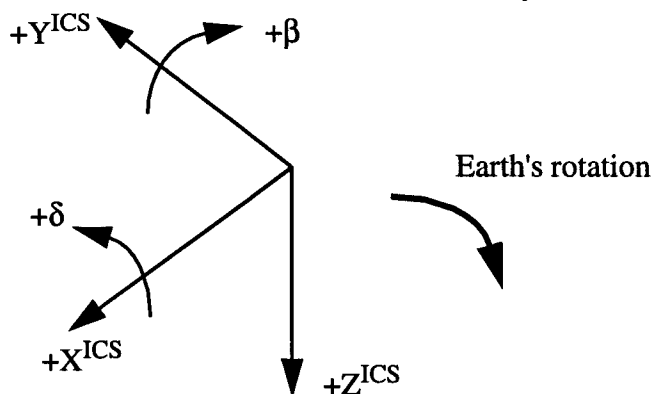

Figure 4.4. ICS with signs for camera angles δ and β defined.

4. ARP: In-flight calibration data

56

4.3.6.3 Camera coordinate systems

For the Camera coordinate system (CCS), the Z-axis is aligned with the optical axis of the camera (where the chief ray intersects the geometric center of the Band 3/ Red CCD array). It is positive in the direction from the detector to the lens. The camera Y-axis is nominally parallel to the long axis of the CCD detector arrays. The camera X-axis is defined as the cross product of the detector Y-axis and the camera Z-axis.

4.3.6.4 Detector coordinate system

The detector coordinate system (DCS) is specified such that the X-axis is perpendicular to the long axis of, and in the plane of, the CCD detector array. The Y-axis is parallel to the long axis of the CCD array with the direction so chosen that the Z-axis is positive in the direction of the lens. The Z-axis is the right-hand cross product of the X- and Y-axes. The CCS axes are aligned with the detector coordinate system (DCS) except where small angle rotations, due to camera assembly and/ or alignment errors, occur.

Fig. 4.5 illustrates the imaging of the MISR camera from object space to the DCS, view from the CCD looking out, to the CCS which takes into account the mounting orientation of the camera onto the optical bench and the definition of the Z-axis. For the nadir and aft cameras, the CCS and the DCS are nominally the same.

4.3.6.5 Panel coordinate system (PCS)

The Panel coordinate system (PCS) can be derived from the ICS by a single rotation about the ICS y axis. The PCS is shown in Fig. 4.6 where the Z-axis is normal to the calibration panel. For calibration of the nadir and aft cameras, which occurs at the North Pole, $\Delta=112.5°$. For the nadir and forward camera calibrations at the South Pole, $\Delta=-112.5°$.
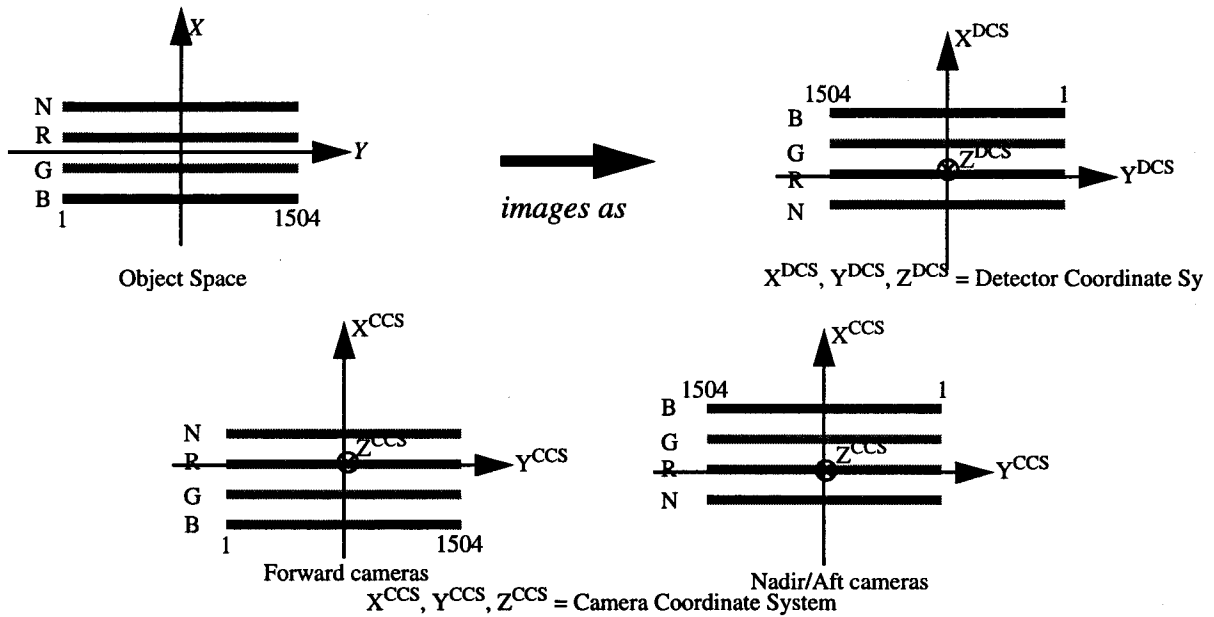
Figure 4.5. Object space to DCS to CCS.

The parameters used to define the panel coordinate system (PCS) are shown in the figures below. The subscripts i and r refer to the incident and reflected directions, respectively. The panel normal is aligned with the Z-axis, and the zenith angle, θ, is measured from these. The Y-axis is in the plane of the panel and parallel to the Y-axis of the ICS; the X-axis is perpendicular to the long dimension of the panel.
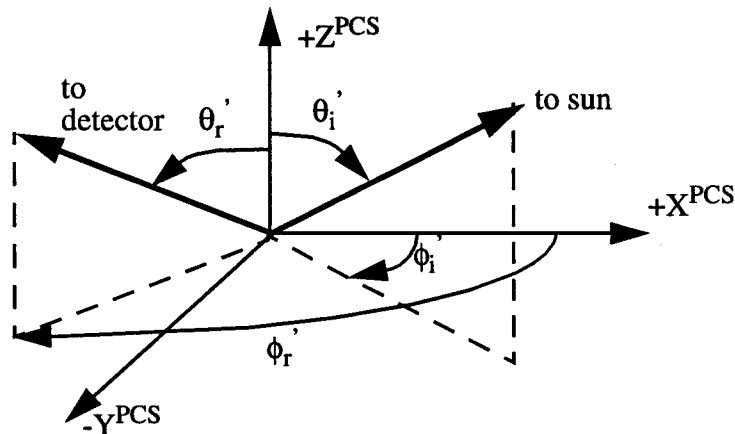
Figure 4.6. Incident and reflected angles in the PCS.

4.3.6.6 Laboratory coordinate system (LCS)

For the BRF measurements, the position of the source (representing the sun) is fixed while the position of the detector (camera/ diode) is confined to movement on a circle of fixed radium in

a plane (one degree of freedom).This laboratory coordinate system (LCS) is depicted by the following figure.
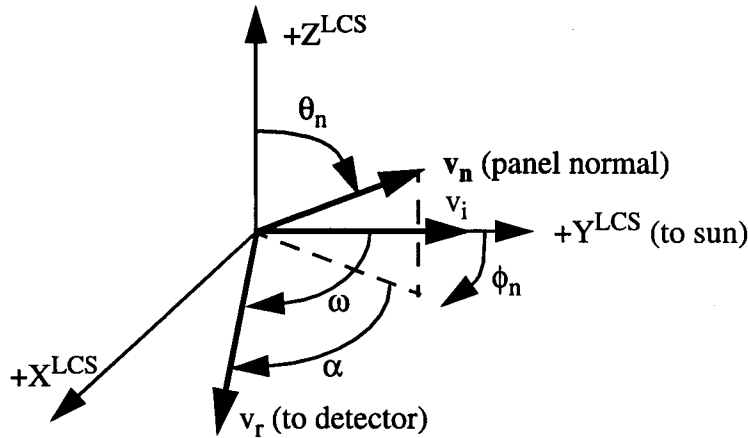
Figure 4.7. Panel normal geometry in the laboratory coordinate system.

Here the source is aligned along the Y-axis, and the +z axis is perpendicular to the principal plane containing the detector and source.

4.3.7 Coordinate transformations for BRF data-base utilization

The camera pointing angles and solar incident angles are initially provided in instrument and spacecraft coordinate systems, respectively. The coordinate transformations needed to determine the associated angles in the panel coordinate system have been defined in SDFM#117[74]. For the cameras, each pixel will have its own view angle in spherical coordinates with respect to the calibration panel. It is important to note that the Nadir camera views either the North panel or the South panel, and that its azimuthal viewing angle will vary between these two cases.

We start by defining the location of pixel p in detector space as shown in Eqn. 4.11. This is an idealized coordinate system that is used as a temporary starting point. Note that while x_{band} depends only upon spectral channel, EFL_{band}, the effective focal length, depends upon spectral channel and camera ID. The values for EFL_{band}, at the nominal optical-bench temperature, are listed in Table 4.4. (The values for other temperatures can be found in the SDFM, although the algorithm is not sensitive to these differences with temperature).

$$\text{Forward cameras:} \quad \begin{bmatrix} x_d \\ y_d \\ z_d \end{bmatrix} = \begin{bmatrix} x_{band} \\ (p - 752.5) \times 0.021 \\ -EFL_{band} \end{bmatrix} \quad [\text{mm}] \quad (4.11)$$

Nadir/ aft cameras: $\begin{bmatrix} x_d \\ y_d \\ z_d \end{bmatrix} = \begin{bmatrix} x_{band} \\ (752.5 - p) \times 0.021 \\ -EFL_{band} \end{bmatrix}$ [mm]   (4.12)

Here

$$x_{band} = \begin{cases} \text{blue} & 0.24 \\ \text{green} & 0.08 \\ \text{red} & -0.08 \\ \text{nir} & -0.24 \end{cases} \text{[mm], and} \qquad (4.13)$$

p is the pixel/ column number (values 1 to 1504) of the Level 1A data product. We utilize two formulas in the above, to account for the inversion done in the Level 1A data product. The conversion from pixel index to physical units is given by the conversion 0.021 mm/ pixel. We have defined the origin as the array center (i.e., half way between pixel 752 and 753 centers).

The next step is to convert to the "ideal" camera coordinate system which takes into account the band and pixel ordering based on how the cameras are mounted onto the optical bench. This conversion is given in Eqn. 4.14. For the nadir camera, the "ideal" CCS would be coincident with the ICS if there were no errors in β and δ.

Forward cameras: $\begin{bmatrix} x_{CCS}^{ideal} \\ y_{CCS}^{ideal} \\ z_{CCS}^{ideal} \end{bmatrix} = \begin{bmatrix} x_d \\ y_d \\ -z_d \end{bmatrix}$ Nadir/Aft cameras: $\begin{bmatrix} x_{CCS}^{ideal} \\ y_{CCS}^{ideal} \\ z_{CCS}^{ideal} \end{bmatrix} = \begin{bmatrix} -x_d \\ -y_d \\ -z_d \end{bmatrix}$ (4.14)

Now we apply the clocking angle and boresight shifts measured with the CAT (collimator array tool) to arrive at pixel location in the CCS (Eqn. 4.15). To transform this point to the ICS, the as-built pointing angles of the CAT (Table 4.7) are utilized in Eqn. 4.16.

$$\begin{bmatrix} x_{CCS} \\ y_{CCS} \\ z_{CCS} \end{bmatrix} = \left(\begin{bmatrix} \cos\varepsilon & \sin\varepsilon & 0 \\ -\sin\varepsilon & \cos\varepsilon & 0 \\ 0 & 0 & 1 \end{bmatrix} \begin{bmatrix} x_{CCS}^{ideal} \\ y_{CCS}^{ideal} \\ z_{CCS}^{ideal} \end{bmatrix} \right) - \begin{bmatrix} dx \\ dy \\ 0 \end{bmatrix} \text{[mm]} \qquad (4.15)$$

4. ARP: In-flight calibration data

60

$$\begin{bmatrix} x_{ICS} \\ y_{ICS} \\ z_{ICS} \end{bmatrix} = \begin{bmatrix} \cos\beta & \sin\beta\sin\delta & \sin\beta\cos\delta \\ 0 & \cos\delta & -\sin\delta \\ -\sin\beta & \cos\beta\sin\delta & \cos\beta\cos\delta \end{bmatrix} \begin{bmatrix} x_{CCS} \\ y_{CCS} \\ z_{CCS} \end{bmatrix} \qquad (4.16)$$

The transformation from ICS to CCS is expressed in Eqns 4.17 and 4.18. The transformation matrix $T_{ics2cpcs}$ differs for each panel, North and South, due to the change in sign of the calibration panel angle Δ. The nadir and aft cameras are calibrated over the North pole while the nadir and forward cameras are calibrated over the South pole.

$$T_{ics2cpcs} = \begin{bmatrix} \cos\Delta & 0 & -\sin\Delta \\ 0 & 1 & 0 \\ \sin\Delta & 0 & \cos\Delta \end{bmatrix} \qquad \Delta = \begin{cases} \text{North Pole:} & 112.5 \\ \text{South Pole:} & -112.5 \end{cases} \quad \text{[degrees]} \qquad (4.17)$$

$$\begin{bmatrix} x_{CPCS} \\ y_{CPCS} \\ z_{CPCS} \end{bmatrix} = T_{ics2cpcs} \begin{bmatrix} x_{ICS} \\ y_{ICS} \\ z_{ICS} \end{bmatrix} \qquad (4.18)$$

Finally, we can compute the spherical coordinates for the vector from the calibration panel to the pixel of interest, p, by following Eqn. 4.19 and Eqn. 4.20.

$$\theta_d = \text{acos}\left(\frac{-z_{PCS}}{\sqrt{x_{PCS}^2 + y_{PCS}^2 + z_{PCS}^2}}\right) \cdot \frac{180}{\pi} \qquad \text{[degrees]} \qquad (4.19)$$

North pole (nadir/aft cameras): $\qquad \phi_d = \text{atan}\left(\frac{y_{PCS}}{x_{PCS}}\right)\frac{180}{\pi} \qquad$ [degrees]

South pole (nadir/forward cameras): $\quad \phi_d = \text{atan}\left(\frac{y_{PCS}}{x_{PCS}}\right)\frac{180}{\pi} - 180 \qquad$ [degrees] $\qquad (4.20)$

Table 4.3. Summary of spherical coordinates for camera detector elements

Camera	Range over all bands and pixels for nominal boresight (pixel 752.5, red)			
	θ_d [deg]	ϕ_d [deg]	θ_d [deg]	ϕ_d [deg]
Df	[9.2, 13.8]	[-206.1, -132.2]	9.8	-163.3
Cf	[16.1, 20.1]	[-203.8, -143.1]	16.5	-171.5
Bf	[27.3, 30.7]	[-202., -151.6]	27.6	-176.3
Af	[43.9, 46.6]	[-199.9, -157.6]	44.2	-178.7
An-South	[67.3, 68.6]	[-196.2, -163.8]	67.5	-180.0
An-North	[67.2, 68.5]	[-16.2, 16.2]	67.5	0.0
Aa	[43.9, 46.6]	[-19.8, 22.3]	44.2	1.3
Ba	[27.3, 30.7]	[-22.8, 36.8]	27.6	3.5
Ca	[16.2, 20.2]	[-23.8, 36.8]	16.5	8.4
Da	[9.4, 13.8]	[-26., 47.4]	9.9	16.1

Table 4.4. Effective focal lengths for MISR cameras

Camera		Operating temperature of 5° C			
Location	ID	blue	green	red	nir
Df	pfd233	123.669	123.681	123.67	123.67
Cf	pfc188	95.343	95.342	95.341	95.341
Bf	pfb366	73.027	73.030	73.030	73.036
Af	pfa172	58.893	58.899	58.903	58.908
An	pfa421	58.934	58.940	58.944	58.951
Aa	pfa244	59.025	59.030	59.035	59.035
Ba	pfb155	72.979	72.995	73.003	73.008
Ca	pfc297	95.33	95.326	95.322	95.325
Da	pfd3109	123.668	123.655	123.653	123.646

Table 4.5. Band and Pixel ordering in ICS

Camera Location	Band Order +X to -X	Pixel Order -Y to +Y
forward	Blue, Green, Red, NIR	1 to 1504
nadir/aft	NIR, Red, Green, Blue	1504 to 1

Table 4.6. Boresight shifts[a] and rotation angles measured with CAT

Camera	dy (crosstrack) [pixel]	dx (alongtrack) [pixel]	clocking/rotation angle (ε[b]) [degrees]
Df	-10.5	-16.5	-0.2759
Cf	-7.3	-1.4	0.0709
Bf	0.3	-2.3	0.0376
Af	3.3	-4.7	-0.0509
An	0.5	3.2	-0.1518
Aa	-3.5	3.0	0.0753
Ba	-3.9	2.7	0.0264
Ca	6.7	-1.8	-0.0421
Da	3.0	2.5	0.1308

a. To get dx and dy in mm multiply by 0.021 mm/pixel.
b. This is the effective clocking angle: as-built CAT angle plus measured rotation angle.

Table 4.7. As-built pointing angles of CAT

Camera	Boresight Angle (β)	Offset Angle (δ)
Df	+58.0035	-2.7007
Cf	+51.2026	-2.3008
Bf	+40.0030	-1.7014
Af	+23.3041	-1.0004
An	0.0010	0.0022
Aa	-23.2980	+1.0032
Ba	-39.9996	+1.7029
Ca	-51.1982	+2.3036
Da	-58.0003	+2.7021

It is noted that the pointing angles are to be recomputed on-orbit. As our algorithm is relatively insensitive to pointing angle changes, we will not be updating these values during the course of our experiment.

Calibration photodiodes

For the On-Board Calibrator photodiodes,

$$\begin{bmatrix} x_{ICS} \\ y_{ICS} \\ z_{ICS} \end{bmatrix} = \begin{bmatrix} \sin\beta\cos\delta \\ -\sin\delta \\ \cos\beta\cos\delta \end{bmatrix} \tag{4.21}$$

where δ is zero for all cases, β is the measured optical bench angle (Table 4.7) and the remaining transformations are the same as for a camera pixel. The photodiodes were mounted on the optical bench to remove the effect of the δ angle built into the optical bench. (The photodiodes were

specified to be mounted with a zero δ angle. This was done so as to make it easier to build than the preferred co-alignment with the cameras. As it turns out, the engineering team had to make a shim to remove the angle built into the optical bench. As the BRF is slowly varying with angle, one design is as good as the other.)

Table 4.8. As-built photodiode pointing angles

Position on Bench		Diode Type	Boresight Angle (β)	Offset Angle (δ)
Df	-X	PIN-3	+57.95	0
Nadir	+Y	PIN-1	0.01	0
	-Y	PIN-2		
	+Y	HQE-BLU		
	+Y	HQE-GRN		
	-Y	HQE-RED		
	-Y	HQE-NIR		
Da	+X	PIN-4	-57.99	0

Sun vector

During the calibration sequence, the angle of the Sun onto the panel will change with time. The sun location will be received from the spacecraft in the spacecraft (platform) coordinate system (SCS) in rectangular coordinates. The SCS and the ICS are nominally aligned except for a translation of the origin and any misalignment due to fabrication errors. A transformation similar in form to that shown in Eqn. 4.15 is required to get from SCS to ICS. The required transformation will depend upon how the manufacture errors are reported. Once the sun location is known in the Instrument Coordinate System, the transformation to PCS and then to spherical coordinates proceeds in the same fashion as for the panel to detector vectors.

$$
\begin{bmatrix} x_{PCS} \\ y_{PCS} \\ z_{PCS} \end{bmatrix} = T_{ics2cpcs} \begin{bmatrix} x_{ICS} \\ y_{ICS} \\ z_{ICS} \end{bmatrix}
\tag{4.22}
$$

$$
\theta_s = acos\left(\frac{-z_{PCS}}{\sqrt{x_{PCS}^2 + y_{PCS}^2 + z_{PCS}^2}}\right) \cdot \frac{180}{\pi} \quad [degrees]
\tag{4.23}
$$

North pole: $\phi_s = atan\left(\frac{y_{PCS}}{x_{PCS}}\right)\frac{180}{\pi}$ [degrees]

South pole: $\phi_s = atan\left(\frac{y_{CPCS}}{x_{CPCS}}\right)\frac{180}{\pi} - 180$ [degrees]

The expected angular range for each calibration site may be summarized as follows.

North pole: $\qquad 38 \le \theta_s \le 55 \qquad -158 \le \phi_s \le -141 \qquad$ [degrees]

South pole: $\qquad 38 \le \theta_s \le 55 \qquad -38 \le \phi_s \le -22 \qquad$ [degrees]

BRF of the calibration panel

Once we know the spherical coordinates of the panel to sun vector, θ_s and ϕ_s, and the spherical coordinates of the panel to detector vector for the given pixel or photodiode, θ_d and ϕ_d, we can find the BRF of the panel.

The BRF is a function of source incidence angle expressed as θ_i and ϕ_i for elevation and azimuth respectively, and detector view angle (θ_r and ϕ_r). In the laboratory, ϕ_i is zero: making use of the independence of the BRF to the absolute values of the detector and source azimuthal angles, we can map the panel BRF for a given sun angle as viewed by a given detector to the laboratory BRF measurements as follows:

$$\theta_i = \theta_s$$
$$\phi_i = 0$$
$$\theta_r = \theta_d \qquad\qquad\qquad (4.24)$$
$$\phi_r = \phi_d - \phi_s$$

SDFM#158[77] gives implementation details for accessing the data base.

4.3.8 BRF stability

The term BRF rectification was initially chosen, as we had planned to use the goniometer data to retrieve an in-flight update to the panel BRF profiles. This algorithm, however, has not been implemented. Rather, our approach for this phase of development will be to verify BRF stability.

Preflight testing has indicated that BRF is maintained even in the presence of panel hemispheric reflectance degradation[4]. In order to verify such in-flight panel BRF stability, however, the goniometer is used to measure this function in the XZ plane (SCS). Should changes be observed, we will increase the uncertainties in the delivered radiometric calibration.

Consider the BRF ratio for a given solar incident and pixel-view geometry,

$$R_{BRF}(t) = \frac{BRF(t;\theta_i, \phi_i; \theta_r^P, \phi_r^P)}{BRF(t;\theta_i, \phi_i; \theta_r^{OBC}, \phi_r^{OBC})} \cdot \qquad\qquad (4.25)$$

The added calibration error due to a change in panel BRF is given by

$$\varepsilon_{BRF} = [R_{BRF}(t)-R_{BRF}(t=0)] * 100./ R_{BRF}(t=0) \qquad (4.26)$$

where

t   is the calibration experiment date index; t=0 corresponds to the preflight determination.

This parameter will be computed for the range of conditions encountered for the calibration experiment, and the worst case error will be folded into the uncertainty tables.

Should an update to the BRF be required at some future date, a reflectance model can be developed to predict on-orbit BRF, empirically adjusted by the within-plane data acquired by the goniometer[8].

4.3.9 Data regression

Once the radiances incident on the camera have been determined (Eqns. 4.7 and 4.9) and correlated with the DN data, a regression of these data give us the radiometric gain coefficients we seek, per Eqn. 4.1. This weighting function is a property of the camera data. For this reason we use only data from the -y-PIN-2 diode in the computation given in this section.

<u>Data weighting</u>

We wish to weight the data to be regressed inversely with the mean variance within a given window. This weighting is computed individually for each camera, band, pixel, and averaging mode. For simplicity, the dependence of the variance on these variables is not noted in the equations given below.

Let the ADN, Adjusted Digital Number, be defined as follows:

$$ADN = [DN - DN_o] \qquad (4.27)$$

The weighting algorithm makes use of a sliding window approach, with a window of a configurable width. After the weighting is computed for the window, it is assigned to the (ADN, diode radiance) index that is found in the middle of the window. The window is then moved over by one data index value, and the process repeated. The data that fall within the extreme ends of the data set are evaluated with a smaller window. Thus, let N be the number of ADN, diode radiance pairs, and W be the window width, and W/2 be a truncated integer, then

Data index, i	Window start index	Window end index
1 ≤ i ≤ W/2	1	i+W/2
W/2+1 ≤ i ≤ N-W/2	i-W/2	i+W/2
N-W/2+1 ≤ i ≤ N	i-W/2	N

For a window width of 101 points, data index 1 uses a window of 50 data points for its assigned variance. Between data indices 50 and N-50 there are 101 points used to compute the variance at data index i. For data indices greater than N-50, there are less than 101 points in the window.

Next the residuals are computed as the difference between the ADN values and a linear fit of the ADN versus diode radiance data within the window. Let $ADN^{fit}(i)$ be the fit of the data found within a window centered on data index i.

The residuals within this window are computed by differencing each ADN value to the linear fit of DN data versus photodiode measured radiance data, for data values that fall within the window. The photodiode determined radiances are computed via Eqn. 4.9 (resampled to the CCD data time grid). The weighting value then follows:

$$wgt_n^{-1} = \sigma_{\mu, n}^2 = \left(\frac{1}{W-1} \sum_{i-W/2, i+W/2-1} [(DN_i - DN_o) - DN_{fit}]^2\right)\left(\frac{1}{W}\right). \tag{4.28}$$

Variable window width

At low equivalent reflectances the illumination is changing rapidly. Here we prefer a smaller window to capture SNR over a small illumination range. At high illumination levels, the incident light does not change rapidly. A larger window is permissible. Initial studies have indicated a window width of 200 at high illumination, and 10 at low illumination might be considered. Operationally, the data stream is divided into a number of regions. For each region a window width is defined. Actual values of the width for each window are configurable.

Coefficient generation. Sensor calibration coefficients are computed from a weighted average of those derived from multiple methodologies. For the in-flight calibration using the photodiodes, the coefficients are determined through a statistical technique known as multiple regression or least-squares fit to a polynomial. These coefficient determinations will later be averaged with others determined from alternate methodologies.

The relationship between the data number or digital output count, DN, and the incident band-weighted spectral radiance, L^{std}, is assumed to be second-order and linear in the parameters of its fitting function. The regression algorithm is provided in this section.

Assume a calibration equation of the form:

$$(DN - DN_o) = G_0 + G_1 L^{std} + G_2 (L^{std})^2 + \varepsilon \tag{4.29}$$

where

L^{std} = incoming spectral radiance weighted by the standardized passband response [W m^{-2} μm^{-1} sr^{-1}];

$DN - DN_0$ = offset subtracted sensor digital number output [DN];

G_0 = detector gain coefficient used to retrieve band weighted radiances [DN];

G_1 = detector gain coefficient [$(W\ m^{-2}\ \mu m^{-1}\ sr^{-1})^{-1}$ DN];

G_2 = detector gain coefficient [$(W\ m^{-2}\ \mu m^{-1}\ sr^{-1})^{-2}$ DN]; and

ε = the increment by which any individual $(DN - DN_0)$ value may fall off the regression line.

In the data reduction we cannot determine the fit parameters or coefficients, G_i, exactly, but we can estimate them from the data collected at multiple illuminations levels by doing a least-squares fit to the function

$$ADN_n^{fit} = G_0 + G_1 L_n + G_2 L_n^2 .$$ (4.30)

Here we have introduced the notation

ADN_n is the video-offset-adjusted output at the illumination level incident during acquisition of data sample n, i.e. DN-DN_0 ; and

ADN_n^{fit} is the estimate of the video-offset-adjusted output, as determined from Eqn. 4.30;

Varying illumination levels are obtained as the solar incident angle sweeps through a range of angles (see the [IFRCC Plan] document).

The coefficients are found by minimizing using following, where the weigthing coefficients have been provided by Eqn. 4.28

$$\chi^2 = \sum [w_n[ADN_n - ADN_n^{fit}]]^2 = \sum [w_n[ADN_n - (G_0 + G_1 L_n + G_2 L_n^2)]]^2$$ (4.31)

which yields the following determinant solution for the coefficients.

$$G_0 = \frac{1}{\Delta} \begin{vmatrix} \sum w_n ADN_n & \sum w_n L_n & \sum w_n L_n^2 \\ \sum w_n ADN_n L_n & \sum w_n L_n^2 & \sum w_n L_n^3 \\ \sum w_n ADN_n L_n^2 & \sum w_n L_n^3 & \sum w_n L_n^4 \end{vmatrix}$$ (4.32)

$$G_1 = \frac{1}{\Delta} \begin{vmatrix} \sum w_n & \sum w_n ADN_n & \sum w_n L_n^2 \\ \sum w_n L_n & \sum w_n ADN_n L_n & \sum w_n L_n^3 \\ \sum w_n L_n^2 & \sum w_n ADN_n L_n^2 & \sum w_n L_n^4 \end{vmatrix} \qquad (4.33)$$

$$G_2 = \frac{1}{\Delta} \begin{vmatrix} \sum w_n & \sum w_n L_n & \sum w_n ADN_n \\ \sum w_n L_n & \sum w_n L_n^2 & \sum w_n ADN_n L_n \\ \sum w_n L_n^2 & \sum w_n L_n^3 & \sum A w_n DN_n L_n^2 \end{vmatrix} \qquad (4.34)$$

$$\Delta = \begin{vmatrix} \sum w_n & \sum w_n L_n & \sum w_n L_n^2 \\ \sum w_n L_n & \sum w_n L_n^2 & \sum w_n L_n^3 \\ \sum w_n L_n^2 & \sum w_n L_n^3 & \sum w_n L_n^4 \end{vmatrix} \qquad (4.35)$$

Once we have estimated the calibration coefficients, the calibration equation is determined and the inverse regression is used to provide our best estimate of the radiance based upon a measured offset-subtracted digital number. In other words, we find the positive real root of

$$G_2 L^2 + G_1 L + G_0 - (DN - DN_o)^{meas} = 0 \qquad (4.36)$$

which can be expressed as

$$L = \frac{-G_1 + \sqrt{G_1^2 - 4G_2[G_0 - (DN - DN_o)^{meas}]}}{2G_2} \qquad (4.37)$$

or alternatively as

$$L = \frac{-2[G_0 - (DN - DN_o)^{meas}]}{G_1 + \sqrt{G_1^2 - 4G_2[G_0 - (DN - DN_o)^{meas}]}} \qquad . \qquad (4.38)$$

The alternate solution to the quadratic is preferred since the gain coefficient G_2 is small.

4.3.10 Vicarious calibration methodology

Output to the vicarious processes are top-of-atmosphere (TOA), band-weighted, camera incident radiances, $L^{std}(\theta_i, \phi_i; \theta_r^P, \phi_r^P)$, which is the radiance at a specific pixel's view angle, and "std" implies the radiance is band-weighted over the MISR standardized spectral response function for this specific band. These will need to be produced for each of the four MISR bands, at view angles where MISR data are collected over the vicarious target, as well as for AirMISR, if it should be available to support the vicarious calibration.

The [IFRCC Plan] discusses several vicarious methodologies. Currently only one is implemented: the surface reflectance-based approach. The ATB for this experiment is written under a separate cover (see [VC ATB]). Note a given vicarious calibration campaign will supply radiances for only a single pixel per channel, 36 channels (and 36 pixels) total. This is because an ideal ground target needs to have surface uniformity over an area three times the MISR pixel footprint, to account for alignment errors between the pixel field-of-view, and target area that is characterized. With pixels sizes of 275 km, it will be likely that most vicarious sites serve only to provide a calibration to a single pixel per channel. This is sufficient for our needs, as other techniques such as histogram equalization will provide an accurate measure of relative response across the detector.

The surface-based techniques rely heavily on radiative transfer codes (RTC), which make use of surface reflectance and an in-situ atmospheric characterization to compute TOA values. These codes operate monochromatically, that is make consecutive computations a single wavelength at a time. For this reason the ideal inputs (surface reflectance/ radiance, and atmospheric optical depth and aerosol parameters) would be collected in a monochromatic fashion. Ten nanometer filters are typically considered sufficient for this purpose. This is currently the approach utilized with the sunphotometer and surface viewing radiometers.

Representative scenes are desert sites, with a clear atmosphere (visibility > 100 km).

The vicarious determinations will utilize measurements at only one radiometric level, and therefore provide information only on the G_1 gain coefficient. The G_0 coefficient is indeterminate from vicarious calibrations, and the G_2 coefficient is approximated as a function of the newly determined G_1 coefficient:

$$\overline{G}_{0,VC} = \overline{G}_{0,OBC} \tag{4.39}$$

$$\overline{G}_{1,VC} = G_{1,VC}(p) / g_1(p) \tag{4.40}$$

$$\overline{G}_{2,VC} = \overline{G}_{2,OBC} (\overline{G}_{1,VC} / \overline{G}_{1,OBC})^2 . \tag{4.41}$$

The latter equation is motivated by the fact that if there is a change in the reported radiance, for the linear term, of an amount $\overline{G}_{1,VC} / \overline{G}_{1,OBC}$, then the change in the quadratic term will change by the square of this radiance change, or $(\overline{G}_{1,VC} / \overline{G}_{1,OBC})^2$.

4. ARP: In-flight calibration data

If more than one vicarious calibration methodology is used, all data that are believed to be accurate, to within the requirements defined by the calibration accuracy budgets, are used (i.e. 3%, as the targets are assumed bright). The multiple methodology reconciliation algorithm will make use of all valid data.

4.3.11 Histogram equalization

Histogram equalization insures that the relative gain coefficients within a channel are such that no striping is observed in the final image. This response normalization is applied after the OBC and VC techniques have determined the degradation of the channel as a whole (i.e., the degradation in the $\overline{G}$'s). The method is image-based, and therefore has the feature of using science data directly, rather than an instrument configuration unique to calibration (i.e. it does not make use of a panel view).

Histogram equalization analysis starts by selecting a statistically large number of scenes. The mean and standard deviation for each channel, pixel, and orbit swath (pole to pole data collected within a given orbit) is reported in a separate quality assurance file. These data are returned to the MISR SCF for histogram equalization processing. These means and standard deviations must be computed by throwing out data from all pixels within a line, if any single pixel is saturated.

The pixel relative response, or g_1 coefficient, is computed from the average of these mean data, as complied for a large number of swaths. We normalize the response function to have a mean of unity, when the average response across the line array is considered.

4.3.12 Dark current evaluation

Data from Cal-Dark will be used to monitor detector dark current stability with time. These data will be compared to the G_0 coefficient derived from the Cal-North and Cal-South data processing, as they should be in agreement.

One option to consider in the future is to constrain the G_0 values in the OBC calibration determination to the dark current observed during Cal-Dark. This newly proposed algorithm will be evaluated once post-launch data become available. An update to the ATB will announce when this algorithm change has been made, if this should be the case.

4.3.13 Trending analysis

The greatest change in sensor responsivity is expected to occur in the period immediately following launch. Here, the sensor is exposed to outgassing from instrument (and platform) components and other transitory affects. After the first month(s) in orbit, however, the responsivity of each camera is expected to change only slowly with time, and in a monotonic fashion. This may be the result of the continued exposure of the system to a radiation environment, or slow photochemical changes of contaminants. It is noted, however, that the

characterization of this responsivity change may require a large number of observations acquired over time. This is due to the uncertainty with which any single characterization is made.

It is for this reason that no single characterization of the system response function will be used to update coefficients transmitted to the DAAC. Rather, each newly generated coefficient will be combined with previous data, and a best curve fit to this time history of response produced. The coefficients to be used following a calibration experiment are those obtained from a fitted curve (trend line), evaluated at the last point in time for which calibration data were supplied. This fit smooths the time response function, and thereby assures the science community that the data products do not abruptly change or oscillate in time, as a result of the uncertainty in sensor calibration.

Consider a series of channel-mean data values, $\overline{G}_t$, stored in a historical calibration file. We wish to weight the fit according to the uncertainty in the individual data, as well as their proximity to the current data acquisition date. We propose the following algorithm. The weighting coefficient is determined as the inverse of the fractional absolute uncertainty scaled by a time factor:

$$w_t = \frac{10^4}{\varepsilon_{t,\,abs}^2}\left(1 - \frac{(\tau_t - \tau_o)^2}{(\tau_s - \tau_o)^2}\right) \tag{4.42}$$

where

t	is the calibration experiment index for which the weighting factor is being computed
τ_o	is the present time, in weeks from launch
τ_t	is the time that this coefficient was applicable, in weeks from launch
τ_s	is the time at the start of the window we are using for the trend, and
$\varepsilon_{t,abs}$	is the absolute radiometric uncertainty of the G coefficient reported at time index t, and at an equivalent reflectance value of 0.5.

Note: to implement a finite window to consider for the trend, the coefficient w_t can be set to zero for those points outside the desired window.

The uncertainty value is obtained from the historical data file. This value is reported at 15 equivalent reflectance levels, as specified in the [IFRCC ATB]. The uncertainty used in the algorithm that which is evaluated at an equivalent reflectance level of 0.5 (i.e., roughly mid-way in the sensor dynamic range).

This equation was developed from analogy to the Fidelity Interval analysis, in which the errors in calibration grow with distance from the mean of radiances used in the calibration experiment. The parameter τ_o is the present time, in weeks since launch. The denominator contains a sum of squares of the time difference from the present time. The factor of 10^4 results

from converting the percentage uncertainty into fractional units. For the current OBC coefficients, it will be necessary to utilize the value of uncertainty reported in the last similar historical data file.

Let us next consider a trend equation of the form:

$$\bar{G} = k_0 + k_1\tau + k_2\tau^2 \quad , \tag{4.43}$$

where time is expressed in units of weeks. The coefficients are found by minimizing

$$\chi^2 = \sum[w_n[\bar{G}_n - \bar{G}_n^{fit}]]^2 \tag{4.44}$$

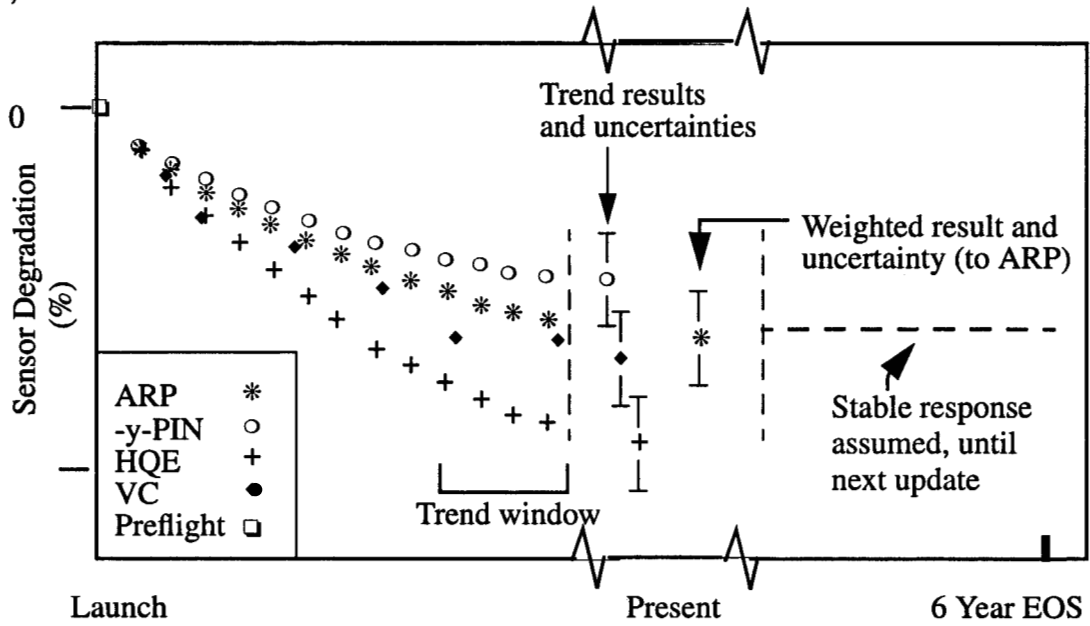$$= \sum[w_n[\bar{G}_n - (k_0 + k_1\tau + k_2\tau^2)]^2] \; . \tag{4.45}$$

Figure 4.8. Coefficient reconciliation approach

Figure 4.8 summarizes the approach. In the above the percentage degradation is computed as:

$$\% \; degradation = \left(\frac{\bar{G}_1 - \bar{G}_{1,\,preflight}}{\bar{G}_{1,\,preflight}}\right)100 \tag{4.46}$$

The uncertainty in the trend-analysis reported gain is given as follows

$$\varepsilon_m = \sqrt{\varepsilon^2_{m,\,abs}(\rho_{eq}=0.5, T) + \frac{1}{(T-1)} \sum_{t\,=\,1,\,T} (\overline{G}_{1,\,m}(t) - \overline{G}^{fit}_{1,\,m}(t))^2} \qquad (4.47)$$

where

ε_m is the percentage uncertainty in the trend coefficients which are to be reconciled (i.e. weighted)

$\varepsilon_{m,abs}$ is the percentage uncertainty in gain coefficient, as reported for this methodology. Its value is that for an equivalent reflectance of 0.5 and for the current calibration experiment.

m   is the methodology index (PIN, HQE, VC, etc.)

t   is the index over the number of time-history data samples.

$\overline{G}_{1,m}$ is the value of the channel-mean gain coefficient at time t, for this methodology.

$\overline{G}_{1,m}^{fit}$ is the value of the trend-line fit at time t for this methodology.

Also reported in the above plot is the final reconciled value (labelled weighted result). This value will be one of the parameters entered into the new ARP file. The uncertainty in this coefficient is that determined from the uncertainty analysis derived later (in Eqn. 4.88).

The gain coefficients we report from this approach will be step functions in time. Assuming the instrument is built to the Science Team's requirements, it is noted that the step size will be small from one month to the next. The MISR team is aware of alternate approaches to trending. For example, a piecewise linear function can be assumed, which would smoothly transition the coefficients in time and avoid the step discontinuity. We believe this is disadvantageous, in that it requires a window in time before the response change information can fully be implemented.

4.3.14 Reconciling multiple methodologies

Calibration coefficients, the end product of the calibration activity, are produced through analysis conducted at the MISR SCF. Data from preflight calibration, the OBC, vicarious calibration campaigns, and image studies such as histogram equalization are considered.

The reconciliation of the vicarious and OBC calibrations is first made. That is, for the coefficients which follow trending we compute the weighted average:

$$\overline{G}_{1,\,ARP} = \frac{\displaystyle\sum_{m\,=\,1,\,M} (\overline{G}_{1,\,m}/\varepsilon^2_m)}{\displaystyle\sum_{m\,=\,1,\,M} (1/\varepsilon^2_m)} \qquad (4.48)$$

where m is the summation index over methodologies (in this case m=1-4), $\overline{G}_{1,m}$ is the channel average gain coefficient, and $\overline{G}_{1,ARP}$ is the final channel average gain coefficient, and ε_i is the absolute uncertainty for methodology m.

This $\overline{G}_{1,ARP}$ value is next used to scale the relative array response. Let $g_{1,ARP}(p)$ be the per pixel relative gain coefficient for an array, as established by reconciling data from the OBC and histogram equalization approaches. This function is normalized such that the mean is one. Thus,

$$G_{1,ARP}(p) = \overline{G}_{1,ARP} * g_{1,ARP}(p). \tag{4.49}$$

This process is repeated for the $G_{0,ARP}(p)$ and $G_{2,ARP}(p)$ coefficients. For the G_0 coefficient, however, data are reconciled from OBC and Cal-dark data; for G_2 data are reconciled from OBC data only.

The absolute uncertainty in the resulting calibration is given by

$$\varepsilon_{reconciled} = \frac{1}{M}\sqrt{\sum_{m=1,M} \varepsilon_m^2} \tag{4.50}$$

where M is the number of methodologies in the root-sum-square. We see that the uncertainty does not converge to zero for a large number of methodologies. We allow for systematic errors in each approach, and state that the uncertainty is simply an RSS average of the individual uncertainties. Note that these two data quality metrics do not fold into the ARP uncertainty values. Rather, they can be used to update the uncertainty tables provided by Table 4.12.

Also computed is the scatter in the methodologies. This is given by the RSS

$$\varepsilon_{scatter} = \sqrt{\left(\frac{1}{M}\sum_{m=1,M} \overline{G}^2_{1,m}\right) - \overline{G}^2_{1,ARP}} \tag{4.51}$$

Note that these two data quality metrics do not fold into the ARP uncertainty values. Rather, they can be used to update the uncertainty tables provided by Table 4.12. In practice we will need to update uncertainty Table 4.12 such that the above two metrics are in reasonable agreement.

4.4 INTEGRATION TIMES

Although each MISR channel can be individually commanded from approximately 0. to 40.8 msec, the actual integration times that will be used are fixed. It is noted that the gain coefficients, which describe the radiometric calibration for each MISR channel, are valid provided the current camera integration times are identical to those used for the calibration experiment. Thus, the ARP tracks the integration times associated with a given set of gain coefficients. The at-launch values that the camera will initially be set to are those derived from preflight radiometric testing. They are selected to achieve the appropriate balance between signal-to-noise ratio (SNR), and saturation. Basically, integration time is selected to just meet a SNR of 100 (in 1x1 mode) for an

input signal of ρ_{eq}=0.02. This is often done at the field edge, where the system transmittance is lowest. This integration time would be decreased if on-axis saturation at ρ_{eq}=1 resulted. This was not found to be the case; however, as little as an 8% margin results for some cameras.

Should on-orbit degradation result in a loss of SNR, the integration times will be adjusted from their at-launch values. However, this will be done on an infrequent basis (perhaps no more than a few times during the mission).

It will be the responsibility of the IFRCC team to coordinate any on-orbit camera configuration changes with the release of a new ARP. Prior to issuing the command to reconfigure to new channel integration times, an associated ARP file will be resident at the DAAC, with gain coefficients adjusted to account for this integration time change. The ARP so delivered will provide scaled coefficients where $G_0(t_{new})=G_0(t_{old})$; $G_1(t_{new})=G_1(t_{old})t_{new}/t_{old}$; and $G_2(t_{new})=G_2(t_{old})[t_{new}/t_{old}]^2$. This algorithm is motivated by the assumption that the G_0 term is independent of the incident radiance, and that the G_1 and G_2 terms respond linearly, and as the square, respectively, to the incident photons. This file will be replaced as soon as a new on-orbit calibration sequence can provide an as-measured response parameters. We therefore envision that an additional ARP delivery should follow the first within 1 week of the configuration change.

The Level 1B processing algorithm checks for consistency in integration times, between those associated with the Level 1A input data and the ARP gain coefficients. This is done at the start of each orbit. (If calibration was done with the camera in one integration time settings, then the derived coefficients are applicable only provided the camera is identically configured. The [L1 ATB] states that processing will continue with the existing coefficients, but an error will be logged.

4.5 EQUIVALENT REFLECTANCES

Radiometric uncertainties and signal-to-noise ratio (SNR) are reported for the instrument at 15 discrete radiometric levels. The parameters are given in terms of equivalent reflectances (see [ISR], [Exp]) and are band independent. The equivalent reflectances will be 0.001, 0.002, 0.005, 0.007, 0.01, 0.02, 0.03, 0.05, 0.07, 0.10, 0.15, 0.2, 0.5, 0.7, and 1.

4.6 SIGNAL-TO-NOISE RATIO

MISR will make use of measurements, when such data are available, to compute signal-to-noise ratio (SNR). For the flight update to this parameter, data from the Cal_North and Cal_South flight sequences will be used. SNR is computed at 15 radiometric levels, and 4 averaging modes, for delivery to the ARP.

To measure SNR at a particular incident illumination level, the local data residuals are used (Eqn. 4.28). These are assigned to an equivalent reflectance value, via the equations:

$$(DN - DN_o) = G_0 + G_1 L_b^{std} + G_2(L_b^{std})^2 \text{, and} \tag{4.52}$$

$$\rho_{eq} = L^{std} / E_b^{std} \ .$$

(4.53)

Note the first equation is simply that used to establish the radiometric calibration of the channel. Equivalent reflectance, ρ_{eq}, is computed from radiance by the second expression. Once SNR is computed versus ρ_{eq}, the appropriate values at the desired radiometric level are found by interpolation. No data extrapolation will be utilized. In the event a given illumination level was unavailable to measure SNR, a radiometric model will be used.

4.6.1 Measuring SNR

4.6.1.1 Algorithm description

MISR will make use of measurements, when data are available for a particular incident illumination condition, to compute signal-to-noise ratio (SNR). For the flight update to this parameter, data from the Cal_North and Cal_South flight sequences will be used. SNR is computed at all pixels and as the array median value, for any of the 15 radiometric levels or averaging modes for which data are available. The following measurement algorithm is valid for all averaging modes. Again, in this discussion, the dependency on camera, band, pixel, and averaging mode is omitted in the notation.

To measure SNR at a particular incident illumination level (or data index), first the in-band signal is determined:

$$\text{Sig\_dn\_inband} = \text{ADN} \cdot \text{InBand}$$

(4.54)

Here InBand is the in- to total-band ratio:

$$\text{InBand} = \frac{\int_{365}^{1100} S_\lambda^{in\text{-}band} \lambda d\lambda}{\int_{365}^{1100} S_\lambda \lambda d\lambda} \ .$$

(4.55)

The values of InBand are taken from SDFM#140, and given in §4.6.5.

The SNR is now given as the ratio of the in-band signal to its standard deviation:

$$\text{SNR(n)} = \frac{\text{Sig\_dn\_inband(n)}}{\text{N\_dn(n)}}$$

(4.56)

where

n   is the line sample index, and

where the standard deviation has been computed using the same sliding window/ variable window width technique discussed in §4.3.9. One difference, however, is that the data are not smoothed (via the polynomial fit) before passing to the SNR processing module. Smoothing is to be performed after combining with the model results (where measured data are not available).

$$(N\_dn)^2 =$$

$$\sigma^2(n) = \left(\frac{1}{W-1}\sum_{r=(N-W/2)}^{N+W/2}[ADN(n) - ADN^{fit}(n)]^2\right) \quad . \tag{4.57}$$

These SNR values are assigned to an equivalent reflectance value, via the equations:

$$L^{std}(i) = \frac{-2[G_0 - ADN(n))]}{G_1 + \sqrt{G_1^2 - 4G_2[G_0 - ADN(n))]}}. \tag{4.58}$$

The values for the G_0, G_1, and G_2 parameters are taken from a previously released ARP. Finally, the following is used to translate the radiance value to equivalent reflectance units, $\rho_{eq}(i)$:

$$\rho_{eq}(n)) = (L^{std}(n))\pi)/E_o^{std}. \tag{4.59}$$

The final step within this module is to determine a value representative of the array. This is done by determining the array median. Let p be the pixel index, and ρ_{eq_arp} be one of the 15 ARP equivalent reflectance values, then:

$$SNR\_array(\rho_{eq\_arp}) = MEDIAN[SNR(p,\rho_{eq\_arp})]. \tag{4.60}$$

4.6.2 Model SNR

4.6.2.1 Algorithm description: 1X1 mode

This radiometric model used for the MISR cameras was developed and summarized in DFM#675. For simplicity the dependency on camera, band, pixel, equivalent reflectance illumination, and averaging mode is omitted in this discussion. This section focuses on 1x1 data.

Signal in electrons, Sig_elect_inband, is calculated via:

$$Sig\_elect\_inband = (G_0 + G_1 L^{in-band} + G_2(L^{in-band})^2)g \text{ , where} \tag{4.61}$$

$$L^{in-band} = (E_o^{std,in-band} \cdot \rho_{eq})/\pi \quad . \tag{4.62}$$

$G_i(c,b,p)$ = are the 3 ARPgen found in a previously released ARP

$E_o^{std,in-band}$= is the in-band band-weighted exo-atmospheric solar irradiance, [W m^{-2} μm^{-1}]

ρ_{eq} = equivalent reflectance = $\pi \, L/E_o^{std,in-band}$

$L^{in-band}$ = in-band weighed incident spectral radiance, [W m^{-2} sr^{-1} μm^{-1}]

g = the camera head analog-to-digital gain factor [e-/ DN].

The parameter g has been determined for each channel, from results of the light transfer test, and summarized below:

Camera	Reference DFM	Band 1/ Blue	Band 2/ Green	Band 3/ Red	Band 4/ NIR
Df	787	70.80	74.60	71.90	71.80
Cf	879	76.85	74.95	80.30	79.70
Bf	848	75.30	77.50	76.40	80.10
Af	929	77.05	80.23	76.91	78.73
An	744	73.15	70.38	72.37	71.80
Aa	801	72.20	74.90	75.70	76.86
Ba	850	69.85	70.68	68.60	70.59
Ca	872	67.86	69.74	67.28	69.91
Da	920	74.73	73.92	74.46	76.04
AirMISR	SDFM 139	75.01	75.81	75.37	75.75

Noise in electrons is computed as

$$N\_elect = \sqrt{N_p^2 + N_q^2 + N_o^2} \,, \tag{4.63}$$

where these terms are developed in the following equations.

Dark current [e-]

The MISR focal plane group has empirically determined dark current as a function of temperature (Neil Pignatano, private communication). This was done for both beginning-of-life (BOL) and end-of-life (EOL) conditions, as simulated following radiation exposure testing. The model provided by this group is as follows.

$$i_{dark} = N \, Temp^{1.5} \, exp^{-\varepsilon/(k \, Temp)} \, [e-/ second] \tag{4.64}$$

where

k   =8.6184e-5 [eV/K], Boltzmann constant
Temp   = the CCD temperature in K
N   =3.098e16 for BOL, 3.45e13 for EOL
ε   = 0.888 for BOL, 0.689 for EOL

Reminder: there is no need to make use of the EOL coefficients for this detector_health module. When we develop the Cal_Dark data analysis tools, we will compare measured data to these preflight predictions.

<u>Video offset</u>

This parameter is of interest in that a change may represent a degradation in the detector quantum efficiency, resulting from radiation damage or other aging mechanisms. For this reason the measured overclock average, $DN_0(c,b,\rho_{eq})$, is to be reported as part of the monthly calibration data analysis. This is to be done as a function of illumination level. Using a linear regression to the measured data, the video offset coefficients $dark\_DN_0$ and m_DN_0 are determined:

$$DN_0(c,b,\rho_{eq})=dark\_DN_0(c,b,0) +m\_DN_0(c,b) \times \rho_{eq} \tag{4.65}$$

$$v_0(c,b,\rho_{eq})=DN_0(c,b,\rho_{eq}) \, g(c,b) \, . \tag{4.66}$$

Note, the focal plane group made an effort to set the video offset to a value approximately equal to FW/60, where FW is the detector full well capacity in electrons.

<u>Photon (Shot) noise, [e-]:</u>

$$N_p = \sqrt{S\_total + i_d \cdot t_i} \, , \text{ where} \tag{4.67}$$

$$S\_total = (G_0 + G_1 L + G_2 L^2)g \quad , \text{ and} \tag{4.68}$$

$$L = \pi(\rho_{eq}/E_o^{std}) \quad . \tag{4.69}$$

S_total = signal integrated over all wavelengths, [e-]
L = total-band weighed incident spectral radiance, [W m^{-2} sr^{-1} μm^{-1}]
i_d = dark current, [e- s^{-1}pixel^{-1}] as determined from BOL model.
t_i = integration time, [s], and

Quantization noise (14-bit linear/ 12-bit square-root encoding), [e-]:

$$N_q = \sqrt{\left(\frac{FW}{\sqrt{12} \cdot 2^{(14-1)}}\right)^2 + \left(\frac{2\sqrt{FW \cdot (S\_total + i_d \cdot t_i + v_o)}}{\sqrt{12} \cdot 2^{12}}\right)^2}$$ (4.70)

FW   =detector fullwell, [e-] = g(c,b)*(2^{14}-1)
v_o =video offset, [e-]
        Note the quantized signal appears in the numerator of the second term:
$S_q = S_T + t_i \cdot i_d + v_o$.

Other noise (e.g. signal chain noise and read noise), [e-]: $N_o = 55$

The signal-to-noise ratio is given by

$$SNR = \frac{Sig\_elect\_inband}{N\_elect}$$ (4.71)

S_elect_inband= signal integrated over in-band wavelengths, [e-]

4.6.2.2 Algorithm description: averaging modes

The algorithm for computing SNR for pixel averaging modes makes use of the same equations as for the 1x1 data mode. The exception is that Eqn. 4.63 is no longer valid. Instead we adopt the expression:

$$N\_elect = \sqrt{(N_p^2 + N_o^2)/(N\_am) + N_q^2} .$$ (4.72)

That is, the photon and other noise is decreased by the square-root of the number of pixels averaged, N_am(c,b). Quantization noise is modeled as independent of averaging mode.

4.6.3 Reconciling measured and modeled SNR parameters

4.6.3.1 Requirement

The median values of SNR that are to be reported to the ARP result from both the measured data, where available, and modeled data, otherwise.

The data reported to the SNR shall be monotonically increasing with equivalent reflectance.

A summary plot shall be made available which plots the measured, modeled, and reconciled values versus equivalent reflectance. Symbols shall denote the respective points, rather than a line style.

A summary plot shall be made available which plots the difference between measured and reconciled data (curve 1), and modeled versus reconciled (curve 2 of the same plot). Symbols shall denote the respective points, rather than a line style.

4.6.3.2 Algorithm

An array shall be constructed which has median values for the array of the measured SNR values, where present, and the modeled, otherwise. A quadratic fit to the these SNR versus ρ_{eq} data is next used to determine the "a" coefficients:

$$SNR(\rho_{eq})=a_0 + a_1\,\rho_{eq} + a_2\,\rho_{eq}^2 \tag{4.73}$$

The data fit are reported to the ARP.

4.6.4 Specifications

Specifications for SNR are given in the [ISD], and listed in Tables 4.9 and 4.10 and below:

Table 4.9. SNR specifications

Equivalent reflectance, %	Minimum SNR
100	700
70	600
50	450
20	300
2	100
<2	Best possible

Table 4.10. SNR Specifications

Band	Equivalent reflectance, %	Minimum SNR
1/ Blue	15	250
	10	225
2/ Green	7	300
	4	200
3/ Red	5	325
	3	200

Table 4.10. SNR Specifications

Band	Equivalent reflectance, %	Minimum SNR
4/ NIR	4	300
	2	200

4.6.5 In-total band ratio

From Table 1, SDFM#140[76]:

Table 4.11. In- to total-band radiance response ratio

Band	Integrated in-band	Integrated total-band	InBand_ radiance
1/ Blue	3070.39	3124.82	0.98
2/ Green	2234.59	2311.01	0.97
3/ Red	2352.82	2413.67	0.97
4/ NIR	3285.81	3352.45	0.98

4.7 ALTERNATE SNR MODEL

An alternate means of combining measured and model SNR data is given here. This approach basically uses the variances computed in Eqn. 4.57, then follows with an empirical fit such that a relationship between noise and illumination can be determined. This approach is preferred, but has not yet been implemented in our code. It has been submitted as IFRCC lien #604.

As before, consider the total noise in electrons to be given as:

$$N_{elect} = \sqrt{N_p^2 + N_q^2 + N_o^2} \; ; \tag{4.74}$$

and the photon noise as

$$N_p = \sqrt{S\_total + i_d \cdot t_i} \, , \text{with} \tag{4.75}$$

$$S\_total = (G_0 + G_1 L + G_2 L^2)g \quad . \tag{4.76}$$

We can then express the noise as a function of a sum of terms in powers of radiance, L:

$$N_p = \sqrt{(gG_0 + i_d \cdot t_i) + gG_1 L + gG_2 L^2} \,. \tag{4.77}$$

Referring to Eqn.4.70, quantization noise can be expressed as

$$N_q = \sqrt{N_{q0}^2 + N_{q1}^2 N_p^2 + N_{q1}^2 v_o} \tag{4.78}$$

where

$$N_{q0} \quad = \frac{FW}{\sqrt{12} \cdot 2^{(14-1)}}$$

$$N_{q1} \quad = \frac{2\sqrt{FW}}{\sqrt{12} \cdot 2^{12}}$$

v_o is the video offset in electrons, given by Eqn. 4.66.

Combining these equations we have

$$N_{elect} = \sqrt{N_{elect,o}^2 + C_1 L + C_2 L^2} \tag{4.79}$$

where the various coefficients can be found to equal

$$C_1 \quad = g\,(1 + N_{q1}{}^2)\,G_1$$

$$C_2 \quad = g\,(1 + N_{q1}{}^2)\,G_2$$

$$N_{elect,o}{}^2 \quad = (g\,G_0 + i_d\,t_i)\,(1 + N_{q1}{}^2) + N_0{}^2 + N_{q0}{}^2 + N_{q1}{}^2\,v_0\,.$$

$$L \quad = (E_o^{std} \cdot \rho_{eq})/\pi$$

This derivation from first principles is used to verify that the functional form of the square of the noise is a quadratic. We thus provide a quadratic fit of the measured data variances, Eqn. 4.57, versus equivalent reflectance, and make use of various relationships we have seen previously:

$$Sig\_elect\_inband = (G_0 + G_1 L^{\text{in-band}} + G_2 (L^{\text{in-band}})^2)g \,, \tag{4.80}$$

$$L^{\text{in-band}} = (E_o^{std,\text{in-band}} \cdot \rho_{eq})/\pi \,. \tag{4.81}$$

$$SNR(\rho_{eq}) = \frac{Sig\_elect\_inband(\rho_{eq})}{N_{elect}(\rho_{eq})} \tag{4.82}$$

4.8   DETECTOR DATA QUALITY INDICATORS

Data Quality Indicators (DQI) are defined to have the values 0 (within specification), 1 (reduced accuracy), 2 (unusable for science), or 3 (unusable for any purpose). The Detector Data Quality Indicators (DDQI) will be computed from measured signal-to-noise (SNR), acquired during 1x1 mode and at the nearest available radiometric illumination level to 2%. The measurement will be taken during the monthly OBC calibration exercise, and require CCD: calibration data and the associated OBC: diode current data. These data are requested at the SCF for in-flight calibration, and so serve a dual purpose.

Additionally, the local non-uniformity will be considered in the DDQI assignment for the case where there is 4x4 or 2x2 on-board averaging. The larger of the two DDQI values (based upon SNR or local non-uniformity) will be assigned to the pixel. This metric reflects that there is a degradation in the radiometry in the presence of on-board averaging over pixels of differing relative radiometric response.

4.8.1 DDQI for 1x1 mode data

For 1x1 data the DDQI will be assigned based solely on the SNR for that pixel. We denote these data as SNR_1x1. These data are obtained from measured data, if available, else model data at the 2% equivalent reflectance level. We use the following formulism to compute the DDQI_1x1 parameter:

SNR_1x1	DDQI_1x1
>100	0, else
>90	1, else
> 10	2, else
	3

4.8.2 DDQI for 2x2 mode data

For the 2x2 data mode, the mean of the SNR_1x1 data over two pixel are utilized. Thus, letting sample be the index of the DDQI_2x2 parameter, we have

- let the pixel_index be the index counter for 1x1 data, having a range of 1504 values,
- sample_index=pixel_index/2 be the index counter for 2x2 data, having a range of 752 values,
- and let the mean be taken across elements specified within the square brackets:
  SNR_1x1(sample_index)=mean (SNR_1x1[pixel_index:pixel_index + 1]) .

Then,

SNR_1x1	DDQI_2x2_snr
>100	0, else
>90	1, else
> 10	2, else
	3

We next consider the impact of local uniformity on the DDQI_2x2 parameter. For the case of 2x2 averaging, local non-uniformity is defined as the relative difference in response across 2 pixels. That is, if the 1504 pixels associated with a given channel are grouped into 752 groups of data samples, we compute the local uniformity metric as the relative difference in pixel response:

$$\text{DDQI\_2x2\_unif}_{c,p} (\text{sample\_index}) = \text{diff}(G_{1,c}[\text{pixel\_index:pixel\_index+1}]) \times 100 / \quad (4.83)$$
$$\text{mean}(G_{1,c}[\text{pixel\_index:pixel\_index+1}])$$

Once the above two metrics are computed, the DDQI_2x2 parameter is computed from the maximum:

$$\text{DDQI\_2x2} = \max([\text{DDQI\_2x2\_snr, DDQI\_2x2\_unif}]) \quad (4.84)$$

4.8.3 DDQI for 4x4 mode data

For the 4x4 data mode, the mean of the SNR_1x1 data over four pixels are utilized. Thus, letting sample be the index of the DDQI_4x4 parameter, we have

• let the pixel_index be the index counter for 1x1 data, having a range of 1504 values,
• sample_index=pixel_index/4 be the index counter for 4x4 data, having a range of 376 values,
• and let the mean be taken across elements specified within the square brackets:
  SNR_1x1(sample_index)=mean (SNR_1x1[pixel_index:pixel_index + 3]) .

Then,

SNR_1x1	DDQI_4x4_snr
>100	0, else
>90	1, else
> 10	2, else
	3

We next consider the impact of local uniformity on the DDQI_4x4 parameter. For the case of 4x4 averaging, local non-uniformity is defined as the relative standard deviation in response

across 4 pixels. That is, if the 1504 pixels associated with a given channel are grouped into 376 groups of data samples, we compute the local uniformity metric as:

$$DDQI\_4x4\_unif_{c,p} \text{ (sample\_index)}=sdev(G_{1,c}[pixel\_index:pixel\_index+3]) \text{ x } 100/ \quad (4.85)$$
$$mean(G_{1,c}[pixel\_index:pixel\_index+3])$$

Once the above two metrics are computed, the DDQI_4x4 parameter is computed from the maximum:

$$DDQI\_4x4=max([DDQI\_4x4\_snr, DDQI\_4x4\_unif]) \quad (4.86)$$

4.9 CHANNEL OPERABILITY FLAG

The channel operability flag, F_c, shall be set to 1 for any channel in which each and every pixel within the array has a SNR < 10 or if the channel is known to have failed. That is, this channel is considered dead. Under normal, or impaired operability of the array, the flag shall be set to 0.

4.10 RADIOMETRIC UNCERTAINTIES

During MISR calibration testing and analysis, the uncertainties are tracked in parallel with the measurements themselves.

4.10.1 Nomenclature

This SDFM documents the algorithm that is be applied to produce the radiometric uncertainty parameters that are reported as part of IFRCC's monthly update to the Ancillary Radiometric Product (ARP). The nomenclature used to describe these deliverable are:

percentage absolute uncertainty (total), ε_{abs_tot}. The estimation of the deviation of a measurement from truth, normalized by the true value and expressed in percentage units: $\varepsilon_{abs\_tot}=(|L_{mea}-L_{true}|x100)/L_{true}$.

percentage relative uncertainty (total), ε_{rel_tot}. The estimation of the deviation in the ratio of two measurements from the true ratio, normalized by the true ratio and expressed in percentage units. To describe this mathematically we let the ratio of measurements L_1 and L_2 be denoted R_{rel}, and the ratio of the true values $L_{true,1}$ and $L_{true,2}$ be denoted R_{true}. We then have $\varepsilon_{rel\_tot}=(|R_{rel}-R_{true}|X100)/R_{true}$. Specific relative uncertainties of interest to MISR are:

percentage band-to-band relative uncertainty (total), ε_{band_tot}. The uncertainty in the ratio of radiances measured by two separate bands within a given camera, expressed in units of a percentage of the true ratio;

percentage camera-to-camera relative uncertainty (total), ε_{cam_tot}. The uncertainty in the ratio of radiances measured by two separate cameras of a common band, expressed in units of a percentage of the true ratio; and

percentage pixel-to-pixel relative uncertainty (total), ε_{pix_tot}. The uncertainty the ratio of radiances measured by two separate pixels within a given MISR channel, expressed in units

of a percentage of the true ratio.

The systematic error parameters are those which are not reduced when the data is spatially averaged. We define these errors here as all error components excluding camera signal-to-noise (SNR). Thus, we can define a systematic term to the absolute and camera, band, and pixel relative errors as that value that when root-sum-squared (RSS) with the SNR specific to that illumination level, camera, and band, will produce the value computed for the associated "total error".

Each of these eight uncertainties are to be reported at 15 illumination levels. These levels defined by the [IFRCC ATB, Section 4.5]. They are: 0.001, 0.002, 0.005, 0.007, 0.01, 0.02, 0.03, 0.05, 0.07, 0.10, 0.15, 0.2, 0.5, 0.7, and 1 in equivalent reflectance units.

4.10.2 Algorithm

Table 4.12 lists all the systematic error components that are known at this time. They are invariant with illumination level, camera, and band (they are scalar values). Each table cell identified with a check indicates that the % uncertainty value listed to the left is applicable. If no such check exists, then this error component should not be included in the column RSS computation.

Table 4.12. In-flight radiometric systematic error sources

Parameter	% uncertainty for all 15x9x4 elements	Uncertainty type			
		Abs., ε_{abs}	Cam. relative , ε_{cam}	Band relative , ε_{band}	Pixel relative , ε_{pix}
Diode radiance uncertainty: internal QE, linearity, SNR, AΩ, filter transmittance	0.8	√			
Diode radiance uncertainty: filter transmittance only	0.5			√	
Diode to camera out-of-band correction	1.0	√			
Diffuse panel relative bidirectional reflectance function (BRF)	2.0	√	√		
Diffuse panel band relative BRF	0.5			√	
Diffuse panel angular stability and flatness	0.01		√		
Diffuse panel spatial non-uniformity	0.2	√	√		√

4. ARP: In-flight calibration data

Table 4.12. In-flight radiometric systematic error sources

Parameter	% uncertainty for all 15x9x4 elements	Uncertainty type			
		Abs., ε_{abs}	Cam. relative , ε_{cam}	Band relative , ε_{band}	Pixel relative , ε_{pix}
Calibration equation fit	0.02	√			
Selection of radiometric levels	0.1	√			

For each of the absolute and relative error components, the systematic component is computed as:

$$\varepsilon_{sys}[\%] = \sqrt{\sum_{r=1,R} \varepsilon_{sys,r}^2} \qquad (4.87)$$

where r is one of the checked row components. These systematic errors are reported in Table 4.13.

Table 4.13. In-flight radiometric uncertainties: OBC methodology

Radiometric uncertainty	Actual	Requirement	
	% uncertainty (invariant with illumination level)	% uncertainty at $\rho_{eq}=1$.	% uncertainty at $\rho_{eq}=0.05$
Absolute	2.4	3.	6.
Camera-to camera relative	2.0	1.	2.
Band-to-band relative	0.7	1.	2.
Pixel-to-pixel relative	0.2	0.5	1.

Next, the total absolute and relative components are computed by including the SNR. Note SNR is a function of illumination level ("equivalent reflectance"), er, camera, c, and band, b. Hence the total uncertainties are also a function of illumination, camera, and band. That is, the output product consist of eight uncertainty parameters, each of which is a 15x9x4 array.

$$\varepsilon_{tot}(er,c,b)[\%] = \sqrt{\sum_{r=1,R} \varepsilon_{sys,r}^2 + (100/SNR(er,c,b))^2} \qquad (4.88)$$

4.10.3 Application

The absolute radiometric uncertainty in the MISR Level 1B1 radiance product is derived from these uncertainty deliverables. Thus,

$$<L>=L_{true}(1\pm\varepsilon_{abs\_tot}/100).$$ (4.89)

Also, let R be the ratio of radiances acquired by different camera, bands, or pixels. Then,

$$R_{cam} = \frac{L_{cam1}(er1,c1,b1)}{L_{cam2}(er2,c2,b1)}$$

$$<R_{cam}>=R_{true}(1\pm\varepsilon_{R\_cam}/100), \text{ where}$$ (4.90)

$$\varepsilon_{R\_cam}[\%] = \sqrt{\sum\varepsilon^2_{cam1\_tot}(er1,c1,b1) + \sum\varepsilon^2_{cam2\_tot}(er2,c2,b2)}$$ (4.91)

The parameter ε_{cam1_tot} is the uncertainty parameter computed by this processing module, for camera 1, and ε_{cam2_tot} is the uncertainty parameter for camera 2. Likewise,

$$R_{band} = \frac{L_{band1}(er1,c1,b1)}{L_{band2}(er2,c1,b2)}$$

$$<R_{band}>=R_{true}(1\pm\varepsilon_{R\_band}/100), \text{ where}$$ (4.92)

$$\varepsilon_{R\_band}[\%] = \sqrt{\sum\varepsilon^2_{band1\_tot}(er1,c1,b1) + \sum\varepsilon^2_{band2\_tot}(er2,c1,b2)}$$ (4.93)

$$R_{pix} = \frac{L_{pix1}(er1,c1,b1)}{L_{pix2}(er2,c1,b1)}$$

$$<R_{pix}>=R_{true}(1\pm\varepsilon_{R\_pix}/100), \text{ where}$$ (4.94)

$$\varepsilon_{R\_pix}[\%] = \sqrt{(\sum\varepsilon^2_{pix\_tot}(er1,c1,b1)) + \sum\varepsilon^2_{pix\_tot}(er2,c1,b1)}$$ (4.95)

A further description of these uncertainties and their utilization in the Level 2 data products can be found in Bruegge, 1999[2].

4.11 SATURATION EQUIVALENT REFLECTANCE

The saturation equivalent reflectance is defined as the minimum incident illumination which would cause a pixel DN output value of $DN_{pix\_sat}(c,b)$, where $DN_{pix\_sat}(c,b)$ is the saturation DN established for a given channel and band and published within the ARP configuration file. (It will be shown in the next chapter to have a value of 16376).

We desire to provide a monthly calibration report which includes the saturation equivalent reflectance, ρ_{eq_sat}. To do so we make use of Eqn. 4.38, substituting in the value of DN_{pix_sat} for DN, and converting to equivalent reflectance units:

$$\rho_{eq\_sat} = \frac{(-2[G_0 - (DN_{pix\_sat} - DN_o)])(\pi / E_o^{std})}{G_1 + \sqrt{G_1^2 - 4G_2[G_0 - (DN_{pix\_sat} - DN_o)]}} \ . \tag{4.96}$$

The values for DN_o can be computed from Eqn. 4.65, using the approximation $\rho_{eq}=1$:

$$DN_o(c,b,\rho_{eq\_sat}) \sim dark\_DN_o(c,b,0) + m\_DN_o(c,b) \tag{4.97}$$

4.12 FIDELITY INTERVAL ANALYSIS

Fidelity Interval Analysis was used extensively in the preflight calibration of MISR. It was useful in evaluating the experiment quality, particularly the adequatecy of the number and values of radiometric levels used for the test. For the in-flight calibration we believe it will also provide a metric as to the quality of the calibration experiment. Should there be a partical loss of data, this analysis will provide a metric which will allow the Science Team to decide if coefficients derived from a calibration experiment should be used to update the ARP. This analysis is derived here.

First, we must specify how much confidence we want. By this, we mean the probability that the true data number lies within the interval we compute. The confidence interval about our calibration equation is formed from the regressed calibration data. MISR requirements are specified to the 68% confidence level (i.e., 1σ for gaussian statistics). The cutoff value, t, from Student's t-distribution is found from standard tables for $\upsilon=N-3$ degrees of freedom at the 68% confidence level, where υ is the number of degrees of freedom on which s^2, the estimate of the variance in the fit, is based, and

$$s^2 = \frac{1}{N-3} \sum_{n = 1, N} (DN_n - DN_n^{fit})^2 \tag{4.98}$$

Let us define the matrix **L**, and its transpose RadianceMatrix ' from the calibration radiances as follows

$$
\text{RadianceMatrix} \ = \
\begin{bmatrix}
1 & L_1 & L_1^2 \\
1 & L_2 & L_2^2 \\
\cdots & \cdots & \cdots \\
1 & L_N & L_N^2
\end{bmatrix}, \qquad
\text{RadianceMatrix}' \ = \
\begin{bmatrix}
1 & 1 & \cdots & 1 \\
L_1 & L_2 & \cdots & L_N \\
L_1^2 & L_2^2 & \cdots & L_N^2
\end{bmatrix}. \quad (4.99)
$$

Then, since the fidelity interval can be regarded as inverse confidence limits for the radiance estimated from a given an offset-subtracted data number, $(DN - DN_o)^{mea}$, the fidelity interval is found by solving

$$
\{-(DN - DN_o)^{mea} + G_0 + G_1 L + G_2 L^2\}^2 = t^2 s^2 \cdot
$$

$$
\left\{ 1 + \begin{bmatrix} 1 & L & L^2 \end{bmatrix} (\ \text{RadianceMatrix}' \ \text{RadianceMatrix}\ )^{-1} \begin{bmatrix} 1 \\ L \\ L^2 \end{bmatrix} \right\} \quad (4.100)
$$

for L. Here L represents the lower, L_l, or upper, L_u, limit of the fidelity interval for the radiance estimate, $\hat{L}$, corresponding to $(DN - DN_o)^{mea}$ as defined in Equation 4.38.

These are the limits in radiance about the radiance estimated from the calibration regression. The relative calibration uncertainty in terms of radiance is defined as

$$
\frac{\partial \hat{L}}{\hat{L}} = \frac{\max(\hat{L} - L_l, L_u - \hat{L})}{\hat{L}}. \tag{4.101}
$$

It should be noted that this radiance uncertainty excludes any random error in the calibration. It does, however, provide a relative measure of one experiment to the next. Unless there is a loss of data, we believe each experiment should have the same Fidelity Interval uncertainty.

It is recommended that any data set be rejected if the Fidelity Interval Analysis suggests that the radiance uncertainties do not meet the calibration requirements specified in the [ISD] document.

4. ARP: In-flight calibration data

5. ARP: CONFIGURATION PARAMETERS

5.1 VERSION NUMBER

It is unlikely that this file will be modified once delivered. A version number will be tracked, however, should this be the case. Version numbers are incremented in sequence. Each of the four ARP files have their own version identifier, so that they might be modified independently of each other. Metadata within the ARP file provide a unique file identifier, published within the Level 1A product.

5.2 MAXIMUM BAND RADIANCES

The processing steps associated with producing radiances from the cameras are:

- On-orbit, square-root encode the 14-bit camera data to 12-bit numbers, preserving resolution at the lower end of the dynamic range. This is done by the flight computer for the purpose of reducing the data transmission rate.

- During Level 1A ground processing, restore to the original 14-bit data, with some resolution loss at the upper end of the dynamic range curve.

- Apply the radiometric calibration coefficients, producing radiances. This is a Level 1B1 floating point operation.

- Convert these radiances to a 14-bit integer, using the formulism [L1Rad ATB]:

$$DN_{1B1,p} = \text{nearest integer } (L_p / \text{scale\_factor}), \tag{5.1}$$

$$\text{scale\_factor} = L_{max,b} / 16376$$

$$= \{0.04720, 0.04653, 0.03853, 0.02467 \text{ W m}^{-2} \text{ } \mu\text{m}^{-1} \text{ sr}^{-1} \text{ DN}^{-1}\} \tag{5.2}$$

where L_p is the observed radiance for a particular pixel, and scale_factor is a band-dependent constant.

To see how scale_factor was derived, we begin with the parameter $L_{max,b}$, which has been precomputed based upon our experience in using the MISR cameras, as tested pre-launch. Ideally we would select a value for this constant which is numerically equal to the physical saturation limit (in radiance units) for a given detector. This would imply having 9*4*1504 constants, one for each detector element. Additionally, these constants would have to change to track the sensor response change in time, as the saturation limit would also change under these circumstances. Instead we pick a $L_{max,b}$ value that is the largest of all the physical saturation limits for each of the nine channels and 1504 pixels, for a given band. This assures us that no data is lost due to the integerization of the radiance data.

We have observed that, radiometrically, the least sensitive pixel is at the edge of the CCD line-array, where the lens transmittance is lowest. For a given incident radiance, the DN output is lowest in this region of the camera, and increases towards the on-axis center. On-axis pixels will saturate at a radiance which may be lower by as much as a factor of 2, as compared to the radiance required to saturate a pixel at the edge of the field-of-view. A $L_{max,b}$ value of 1.3 in equivalent reflectance assures that no data will be lost due to this scale_factor value, even at the array center. Therefore,

$$L_{max,b} = 1.3\, E_{0,b}^{std}/\pi = \{773., 762., 631., \text{and } 404.\ \text{W m}^{-2}\ \mu\text{m}^{-1}\ \text{sr}^{-1}\}$$

5.3 PIXEL SATURATION BLOOMING (PIX_SAT)

5.3.1 Low saturation probability

It is noted that ocean glints have the potential for producing strong signals. Consider a solar-reflecting mirror, with no absorption. The radiance reflected from this target in the specular direction would be $L_{mirror}=E_{0\lambda}/\Omega$, or π/Ω times more intense than a lambertian target. Here Ω is the solid angle of the Sun, hence $\pi/\Omega = \pi/[\pi(0.5°)^2/4] = 5\times10^4$. It is noted, however, that even if the ocean were to reflect in such a manner, only a small fractional area within the MISR IFOV would be oriented so as to reflect energy into the cameras.

The integration times for each of the MISR channels are independently selectable. Furthermore, each has been set to insure saturation above an equivalent reflectance of unity[18]. Even bright targets such as snow and clouds typically have an equivalent reflectance less than this amount, particularly as non-zero zenith angle solar illumination attenuates the signal. For these reasons saturation is believed to occur infrequently once on-orbit.

5.3.2 Saturated point-spread function profiles

From preflight testing it has been determined that saturated pixels do bloom, reducing data integrity across much of line array[64]. This has been found to be particularly true for pixels clocked out following the saturated pixel. Saturation is defined as any pixel for which DN_p is greater than or equal to the maximum allowable value, DN_{pix_sat}, where

$$DN_{pix\_sat}=16376 \tag{5.3}$$

==> Need to explain why are using 16376 and not 16383

for this 14-bit instrument. (For 2x2, or 4x4 averaging modes, a pixel is also considered saturated if the image of the same target is saturated in the red-band. The red-band pixels are always reported in 1x1). Saturation blooming is defined as an additive noise that affects a non-saturated pixel which is in the vicinity of a saturated pixel. Saturated PSF profiles were obtained during preflight testing by first viewing a pinhole target adjusted in intensity to produce a signal that was just below the saturation limit. The camera integration times were then increased by a factor of 20, producing an image that was oversaturated by a known amount. The size of the target is such that sub-pixel illumination is predicted from diffraction theory, for either case. Figure 5.1 shows the PSF response to both this saturated image (outer curve) and unsaturated image (inner curve). The

saturated PSF response has a larger amplitude in the wings, as compared to the unsaturated case. This is due both to optical and electrical effects. As the integration time has been increased for the array, adjacent pixels produce a larger DN in response to the halo that surrounds the image point. (This halo is known to be the result of reflections between the CCD and filter, within the focal plane[11]). A new observation is made for this case, however, namely that the PSF is asymmetric. Pixels to the right (that is, pixels clocked out after the saturated pixel), have more noise than those equally spaced but to the left of the image point. As optical scattering is believed to produce a symmetrical halo about the image, the added noise to the right is believed to be the result of an electronic out-of-range condition, which requires a fraction of the line sample time to recover. This electronic noise effects appears to have a slower rate of decay with distance, as compared to the optical noise.

5.3.3 Data Quality Indicator parameters

The [L1Rad ATB] has defined a data integrity algorithm, whereby a segment of the array is considered unsuitable for use if it contains one or more saturated pixels. Under such conditions a Data Quality Indicator (DQI) flag is set to indicate a data error condition. The parameters needed to compute the DQI flags are DN_{pix_sat}, n_{pix_sat}, $n_{i,am}$, a_{i,pix_sat}, and ε_{i,pix_sat}. The subscripts "pix_sat" designate these data processing parameters as being associated with the pixel saturation blooming error condition.

Initially, the DQI algorithm identifies zones which contain one or more saturated pixels. Consider the parameters $n_{1,am}$ and $n_{2,am}$, where the subscript "i"=1 identifies a fixed distance to the left of the first saturated pixel, $p_{sat,i}$, within a zone, and "i"=2 identifies a fixed distance from the right of the last saturated pixel, $p_{sat,nsat}$, within a zone. The "am" indicates that these distances differ for the averaging modes, and "nsat" is the number of saturated pixels in a zone. These saturated pixels are such that for 1 n nsat :

$$p_{sat,n} < p_{sat,n-1} + n_{1,am} + n_{2,am}. \tag{5.4}$$

That is, within the same zone no two saturated pixels are greater than a distance of $n_{1,am}+n_{2,am}$ from each other. The boundary limits defined above refer to distances with respect to the pixel clocking order. Thus, terms left and right refer here to pixels clocked out before, or after, the saturated pixel. Pixel 1 is the first to be clocked out, 1504 the last. In terms of MISR images, $n_{1,am}$ may appear to the west, or east, of a saturated pixel, depending upon the camera. This is because the nine MISR cameras are assembled into the instrument in one of two 180° orientations.

The size of each saturated zone, Δp_z, can therefore be defined as

$$\Delta p_z = n_{1,am} + p_{sat,nsat} - p_{sat,1} + 1 + n_{2,am}. \tag{5.5}$$

The coefficients, $n_{i,1x1}$ are applicable for either 1x1 or 1x4 averaging modes. Using these values, the zone width will be 188 pixels wide for a single saturated pixel in 1x1 mode, and $(188 + p_{sat,nsat}$-

$p_{sat,1}$) for "nsat" saturated pixels in the zone. All pixels within this zone are considered unusable by later processing algorithms.

From plots such as Fig. 5.1, the following definitions have been made:

$$n_{1,1x1}=50 \text{ and } n_{2,1x1}=137 , \tag{5.6}$$

$$n_{1,2x2}=25 \text{ and } n_{2,2x2}=69 , \text{ and} \tag{5.7}$$

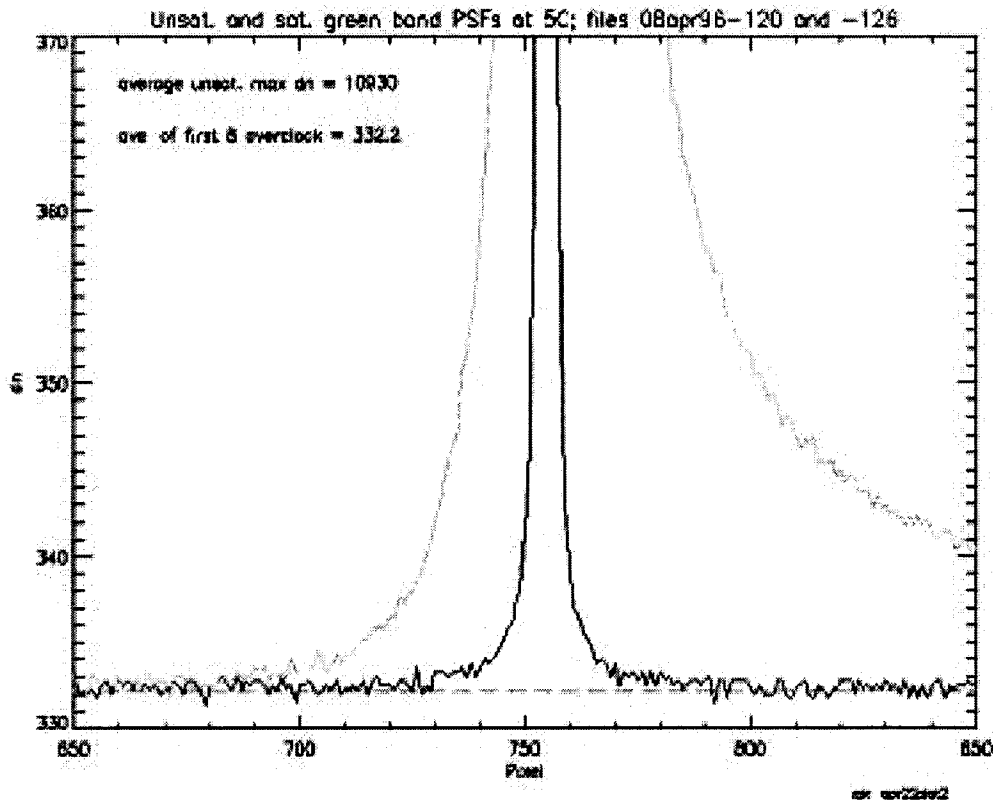$$n_{1,4x4}=13 \text{ and } n_{2,4x4}=34. \tag{5.8}$$

Figure 5.1. Saturation blooming

Outside of this range the noise falls to an acceptable level (i.e. the saturation blooming noise, ΔDN_{nsat}, is such that ΔDN_1 5 DN under conditions of nsat=1).

In establishing the saturation zone boundaries, an extreme condition (oversaturation factor of 20) was considered. This provides the worst-case area to exclude in the presence of a single saturated pixel. For a smaller oversaturation factor, the noise associated with saturation blooming is less severe, and perhaps more pixels than needed are excluded. This is acceptable in that a conservative error handling approach is desired. For those cases where more than one saturated pixels falls in a zone, data from an even larger portion of the array is excluded from processing.

5. ARP: Configuration parameters

96

This comes about in two ways: the zone width increases, and the estimated saturation blooming noise, ΔDN_{nsat}, increases. For pixels to the right of the saturation zone, data are used only if the DN_p is considered to be large, as compared to the blooming noise. Extended saturated image studies[64] have shown that blooming noise increases to a value of ΔDN_{750}=300 DN for the case where there is a continuum of 750 saturated pixels. Recalling, from above that ΔDN_1=5 DN, and assuming a linear relationship between noise and the number of saturated pixels within a zone, we establish

$$\Delta DN_{nsat} = \frac{(\Delta DN_{750} - \Delta DN_1)}{750 - 1}(m \cdot nsat - 1) + \Delta DN_1 \quad . \text{ Thus,} \tag{5.9}$$

$$\Delta DN_{nsat, 2x2} = a_0 + a_1 \cdot m \cdot nsat \quad , \text{ with} \tag{5.10}$$

$a_0 = 4.61$ and a_1=0.39, and m=1 (for 1x1 or 1x4), 2 (for 2x2), or 4 (for 4.4 averaging mode).

The percentage allowable noise, ε_{pix_sat}, for pixels outside the saturation zone is assigned to be

$$\varepsilon_{pix\_sat} = 0.5\% \quad . \tag{5.11}$$

Converting both the observed DN and noise ΔDN_{nsat} into radiance units ([L1Rad ATB]) the pixels for which

$$L_p \Delta L_{nsat} \, 100/ \, \varepsilon_{pix\_sat} \tag{5.12}$$

are considered usable, but are weighted half as much as if no saturation had occurred. This condition is indicated by a DQI value of 1, to indicate a reduction in accuracy.

The maximum number of allowable saturated pixels in a line is set to be

$$n_{pix\_sat} = 100 \quad . \tag{5.13}$$

If $nsat > n_{pix\_sat}$ then the entire line is considered unusable. This somewhat arbitrary limit can be adjusted during the mission, if there is a need. It is noted that preflight testing evaluated only the limited conditions nsat=1 and nsat=750.

In summary, Level 1A/ 1B1 processing will use the parameters described in this section to assign DQI's per the following logic:

Table 5.2. Saturation blooming DQI conditional statements

	DQI$_p$ value	Condition
	0 (within specifca-tion)	if nsat=0
else	1 (reduced accu-racy)	if $[p < p_{1,sat} - n_{1,am}$ and (m nsat) $n_{pix\_sat}]$ or if $[p > p_{sat,n} + n_{2,am}$ and $L_p \Delta L_{nsat}$ 100/ ε_{pix_sat} and (m nsat) $n_{pix\_sat}]$. Here $p_{sat,1}$ is the lowest numbered pixel which is saturate within a zone, $p_{sat,n}$ the highest number. Also, m=1 for 1x1, 2 for 2x2, and 4 for 4x4 averaging. "nsat" is the number of saturated pixels in a zone.
else	2 (specification violated)	

5.4 VIDEO OFFSET UNCERTAINTY (LINE_SAT)

Camera DN output is roughly composed of an additive video offset term, plus a term proportional to the incident radiance. The video offset is a dynamic number, and is proportional to the average DN for the array[61]. It also is known to change slowly with time, achieving a new steady-state value in about 25 line times following a change in the target intensity. The video offset is best measured by averaging the eight overclock pixels that are transmitted following clocking of the active pixels[49] (with m=1 for 1x1 or 1x4; =2 for 2x2; or =4 for 4x4 averaging mode).

During preflight camera testing, an unexpected finding was made in that the overclock pixels did not always report identically the same DN. This occurs for conditions in which there is a high average DN, denoted $DN_{ave,c}$, across a given line of data (hence the designator "line_sat" for this condition). Additionally, for these situations the 8 pixel shielded regions to the left and right of the active region differ in average DN. At average DN levels at or exceeding the value $DN_{line\_sat,b}$, the video offset non-uniformity (hence uncertainty, ΔDN_{line_sat}) becomes significant. It has been observed that

$$DN_{line\_sat,b} = \{16K, 16K, 14K, \text{ and } 12K\} \qquad (5.14)$$

for Bands 1-4, respectively, and that

$$\Delta DN_{line\_sat} = 25 \text{ DN} \qquad (5.15)$$

It is postulated that at a signal exceeding $DN_{line\_sat,b}$, the CCD approaches full-well, and charge begins to spill out into near-by trap sites. In order to read a CCD pixel, the charged is dumped into the serial register, and passed from one serial register to the next until the signal from a given pixel is sampled. After the active pixels are measured, sampling continues in order to measure the video offset. At this point, the equilibrium between the CCD loss mechanism and trap sites is disturbed, as now the active pixels have been drained. This allows the trapped charge to flow into the overclock samples, until depleted. As this trapped charge contaminates the overclock data sample, it creates an uncertainty in the video offset measurement.

A Data Quality Indicator (DQI) flags when the video offset measurement becomes uncertain. The parameters associated with this flag are $DN_{line\_sat,b}$, ΔDN_{line_sat}, and ε_{line_sat}. As in the above section, the data are considered usable if the signal is large compared to the noise uncertainty. Defining,

$$\varepsilon_{line\_sat}=0.5\% \qquad\qquad\qquad (5.16)$$

the following algorithm is provided:

Table 5.3. Video offset uncertainty DQI conditional statements

	DQI_p value	Condition
	0 (within specification)	if $[L_{ave,c} < L_{line\_sat,b}]$
else	1 (reduced accuracy)	if $[L_p \, \Delta L_{line\_sat} \, 100/ \, \varepsilon_{line\_sat}]$
else	2 (specification violated)	

Where the DN and ΔD_{line_sat} are converted to radiance units, during Level 1B processing. For the parameters defined here, the minimum radiance required such that DQI=1 is the equivalent associated with $DN_p =5000$.

6. ASSUMPTIONS AND LIMITATIONS

6.1 ASSUMPTIONS

None identified.

6.2 LIMITATIONS

None identified.

5. Assumptions

7. REFERENCES

7.1 OPEN LITERATURE (CONFERENCE AND JOURNALS)

1. Bevington, Philip R. and D. Keith Robinson (1992). Data Reduction and Error Analysis for the Physical Sciences, Second Edition. McGraw Hill, Inc.

2. Bruegge, C.J., N.L. Chrien, D.J. Diner, R.A. Kahn, J.V. Martonchik (1999). MISR radiometric uncertainty analyses and their utilization within geophysical retrievals. Submitted NEWRAD97 Conference issue, Metrologia.

3. Bruegge, C.J., N.L. Chrien, and D. Haner (1999). A Spectralon BRF data base for MISR calibration applications. Submitted to Remote Sens. Environment.

4. Bruegge, C.J., A.E. Stiegman, D.R. Coulter, R.R. Hale, D. J. Diner, and A.W. Springsteen (1991). Reflectance stability analysis of Spectralon diffuse calibration panels. SPIE Vol. 1493 Calibration of Passive Remote Observing Optical and Microwave Instrumentation, Orlando, Florida, 3-5 April.

5. Chrien, N.C.L., C.J. Bruegge, and B.R. Barkstrom (1993). Estimation of calibration uncertainties for the Multi-angle Imaging SpectroRadiometer (MISR) via fidelity intervals. In *Sensor Systems for the Early Earth Observing System Platforms*, Proc. SPIE **1939**, April, 114-125.

6. Chrien, N.L., C.J. Bruegge (1996). Out-of-band spectral correction algorithm for the Multi-angle Imaging SpectroRadiometer. In *Earth Observing System*, Proc. SPIE, Vol. 2820, Denver, Co, 5-9 August.

7. Draper, N.R. and H. Smith (1981). Applied Regression Analysis, Second Edition. John Wiley & Sons.

8. Flasse, S.P., M.M. Verstraete, B. Pinty, and C.J. Bruegge (1993). Modeling Spectralon's bidirectional reflectance for in-flight calibration of Earth-orbiting sensors. In Recent Advances in *Sensors, Radiometric Calibration, and Processing of Remotely Sensed Data*, Proc. SPIE **1938**, April, 100-108.

9. Flitner, D.E., B.M. Herman, K.J. Thome, and J.M. Simpson (1993). Total ozone and aerosols optical depths inferred from radiometric measurements in the Chappuis absorption bnad, J. Atmos. Sci, 50, 1113-1121.

10. Korechoff, R., D. Kirby, E. Hochberg, C. Sepulveda, and V. Jovanovic (1996). Distortion calibration of the MISR linear detectors. In *Earth Observing System*, Proc. SPIE, Vol. 2820, 05-09August, Denver, CO.

11. Korechoff, R.P, D.J. Diner, D.J. Preston, C.J. Bruegge (1995). In Advanced and Next-Generation Satellites. Spectroradiometer focal-plane design considerations: lessons learned from MISR camera testing. EUROPTO/ SPIE Vol. 2538, pp. 104-116, 25-28 September, Paris, France.

12. Wehrli, C. Extraterrestrial Solar Spectrum. World Radiation Center (WRC), Davos-Dorf, Switzerland, WRC Publication No. 615, July, 1985.

7.2 DESIGN FILE MEMORANDUMS

The following table lists MISR project DFMs by test name. Complete reference names are also provided here.

Table 7.1. DFM listing by camera test name

Camera/ test name	D233 (Df)	C188 (Cf)	B366 (Bf)	A172 (Af)	A421 (An)	A244 (Aa)	B155 (Ba)	C297 (Ca)	D3109 (Da)
EFL, boresight, distortion	782	881	824	926	747	811	862	873	910
Radiometric	806	883	864	946	779	829	865	883	931
Spectral	807	898	845	947	777	830	866	884	930
Radiometric model	787	879	848	929	744	801	850	872	920

13. McGuire, J. (23Jun91). Feasibility of Lyot depolarizers for MISR. DFM#58.
14. Wenkert, D. (20Aug93). Angles of the sun and its reflection during on-orbit calibrations. DFM#267A.
15. Jorquera, C. (4 Oct 94). Calibration Photodiode QE at 1250 nm. DFM#495.
16. Chrien, N. (14Aug95). Radiometic model for MISR cameras. DFM#675.
17. Vaughn, A. (18Aug95). Monochromator calibration. DFM#704.
18. Chrien, N. (25Oct95). Adjusted radiometric math model for MISR cameras. DFM#731.
19. Lee, M. (26Oct95). Contrasting target performance for PFA312. DFM#735.
20. Chrien, N. (10Oct95). Radiometric model for camera PFA421. DFM#744.
21. Korechoff, R. (20Dec95). Summary of OCC test results for camera PFA421. DFM#794.
22. Gaitley, B.J., and C.J. Bruegge (04Dec95). Spectral calibration of PFA421. DFM#777.
23. Lee, M. (04Dec95). Contrast target response of PFA421. DFM#778.
24. Bruegge, C.J. (04Dec95). Radiometric studies on camera PFA421. DFM#779.
25. Korechoff, R. (07Dec95). Summary of OCC test results for camera PFD233. DFM#782.
26. Chrien, N. (14Dec95). Radiometric model for camera PFD233. DFM#787.
27. Korechoff, R. (20Dec95). Summary of OCC test results for camera PFA421. DFM#794.
28. Chrien, N. (10Jan96). Radiometric model for camera PFA244. DFM#801.
29. Bhattacharaya, B., and C.J. Bruegge (17Jan96). Radiometric calibration of PFD233. DFM#806.
30. Gaitley, B.J., and C.J. Bruegge (25Jan95). Spectral calibration of PFD233. DFM#807.
31. Korechoff, R. (16Jan96). Summary of OCC test results for camera PFA244. DFM#811.
32. Korechoff, R. (02Feb96). Summary of OCC test results for camera PFB366. DFM#824.
33. Gaitley, B.J., and C.J. Bruegge (06Feb96). Radiometric calibration of PFA244. DFM#829.
34. Gaitley, B.J., and C.J. Bruegge (07Feb96). Spectral calibration of PFA244. DFM#830.
35. Gaitley, B.J., and C.J. Bruegge (21Feb96). Spectral calibration of PFB366. DFM#845.
36. Chrien, N. (28Feb96). Radiometric model for camera PFB366. DFM#848.
37. Chrien, N. (28Feb96). Radiometric model for camera PFB155. DFM#850.
38. Korechoff, R.P. (13Mar96). Pixel-averaged point spread functions. DFM#861.

39. Korechoff, R. (20Mar96). Summary of OCC test results for camera PFB155. DFM#862.
40. Gaitley, B.J., and C.J. Bruegge (21Mar96). Radiometric calibration of PFB366. DFM#864.
41. Gaitley, B.J., and C.J. Bruegge (21Mar96). Radiometric calibration of PFB155. DFM#865.
42. Gaitley, B.J., and C.J. Bruegge (21Mar96). Spectral calibration of PFB155. DFM#866.
43. Chrien, N. (02Apr96). Radiometric model for camera PFC297. DFM#872.
44. Korechoff, R. (04Apr96). Summary of OCC test results for camera PFC297. DFM#873.
45. Chrien, N. (16Apr96). Radiometric model for camera PFC188. DFM#879.
46. Korechoff, R. (17Apr96). Summary of OCC test results for camera PFC188. DFM#881.
47. Gaitley, B.J., and C.J. Bruegge (19Apr96). Radiometric calibration of PFC297. DFM#883.
48. Gaitley, B.J., and C.J. Bruegge (19Apr96). Spectral calibration of PFC297. DFM#884.
49. Bruegge, C.J. (26Apr96). Request for overclock pixels. DFM#888.
50. Gaitley, B.J., and C.J. Bruegge (16May96). Radiometric calibration of PFC188. DFM#897.
51. Gaitley, B.J., and C.J. Bruegge (16May96). Spectral calibration of PFC188. DFM#898.
52. Korechoff, R. (17May96). Coordinate transformations for Spectralon BRF files. DFM#899.
53. Deslis, T. (28May96). Code V transmittance predictions vs. measured coated and radiated. DFM#908.
54. Korechoff, R. (03Jun96). Summary of OCC test results for camera PFD3109. DFM#910.
55. Chrien, N. (20Jun96). Radiometric model for camera PFD3109. DFM#920.
56. Korechoff, R. (16Jul96). Summary of OCC test results for camera PFA172. DFM#926.
57. Chrien, N. (16Jul96). Radiometric model for camera PFA172. DFM#929.
58. Gaitley, B.J., and C.J. Bruegge (17Jul96). Spectral calibration of PFD3109. DFM#930.
59. Gaitley, B.J., and C.J. Bruegge (16Jul96). Radiometric calibration of PFD3109. DFM#931.
60. McMuldroch, S. (18Jul96). Optimizing the camera positions on the optical bench. DFM#932.
61. Ozawa, T. (22Mar96). MISR signal chain and its BLS circuit. DFM#933.
62. Gaitley, B.J., and C.J. Bruegge (12Aug96). Radiometric calibration of PFA172. DFM#946.
63. Gaitley, B.J., and C.J. Bruegge (12Aug96). Spectral calibration of PFA172. DFM#947.
64. Korechoff, R.P. (31Jul96).Pixel saturation effects.DFM#943.
65. Chrien, N. (12Aug96). Functional form for calibration equation. DFM#949.
66. Duval, V. (12Aug96). Integrating Sphere Calibration. DFM#951.
67. Duval, V. (12Aug96). Calibration of the Flight Calibration Photodiodes. DFM#952.
68. Bruegge, C.J. and N.L. Chrien (24Aug96). Round-robin'96 sphere calibration. DFM#961.
69. Korechoff, R.P. (05Sep96). Required measurements for BRF calibration of Spectralon panels. DFM#963.
70. Chrien, N.L. (8Jan97). Photodiode spectral response data summary. DFM#995.

7.3 SCIENCE DESIGN FILE MEMORANDUMS

71. Gaitley, B.J. (13Jan99). Ancillary Radiometric Products. SDFM#78A.
72. Chrien, N.L. (1997). Definitions of band and pixel ordering of the MISR cameras. SDFM#106.
73. Bruegge, C. (5Dec97). ARP structure and algorithm change requests. SDFM#107A.
74. Chrien, N.L. (2Dec97). Spherical coordinates and BRF for OBC. SDFM#117.
75. Bruegge, C.J. (16Oct98). IFRCC detector health algorithms. SDFM#138A.
76. Gaitley, B.J. (12Feb98). Spectral response function integrals. SDFM#140.
77. Chrien, N.L. (4Jun98). Alternate method for interpolation of MISR OBC BRF. SDFM#158.

78. Chrien, N.L. (18Jun98). OBC BRF at diode boresight vs. OBC BRF integrated over diode FOV. SDFM#168.

79. Bruegge, C.J. (20Jan99). Radiometric uncertainty algorithm. SDFM#196.

7.4 OTHER MISR DOCUMENTS

80. Duval, V.G. and G. Saghri (Oct95). Pre-calibration Procedure. Procedure 217P.

81. Duval, V.G., B. McGuckin, and D. Haner (July1995). Calibration plate optical test procedure (BRF test). Procedure 207P.

APPENDIX A. RADIOMETRIC EQUATION DEVELOPMENT

A.1 DETECTOR RESPONSE THEORY

This appendix develops the relationships between detector standard output current and incident radiance, as well as between incident radiance and MISR output DN. These relationships are used to establish the radiometric calibration for the MISR cameras. As radiometric calibration involves a preflight measurement, as well as multiple in-flight methodologies, each of these are additionally addressed.

A.1.1 Photodiode standards

MISR makes use of photodiode standards to establish its radiometic scale. This is the case for both the preflight and post-launch calibrations. As MISR photodiode standards are photoconductive devices, they produce a current in response to incident photons. For either the laboratory standards, used to calibrate the integrating sphere, or the flight standards, this relationship can be expressed by:

$$i_\lambda = R_\lambda^{diode} q N_\lambda , \text{ where} \tag{A.1}$$

R_λ^{diode} [none] is the detector quantum efficiency, filter and window transmittance product

$q = 1.6 \times 10^{-19}$ [Coul] is the electron charge

N_λ [p/s] is the photon rate

The energy per photon can be expressed by

$$E_\lambda = hc/\lambda \text{ [joule]} , \tag{A.2}$$

or in units of electron-Volts as

$$E_{ev} = hc/q\lambda \text{ [eV]} \tag{A.3}$$

$$= 1.2395 \text{ eV } \mu m/\lambda \text{ [eV]} \tag{A.4}$$

where

$h = 6.6256 \times 10^{-34}$ W s^2 is Planck's constant

$c = 2.9979 \times 10^8$ m/s is the speed of light

The photon rate is found as the ratio of incident flux, Φ_λ, to photon energy where

$\Phi_\lambda = L_\lambda A\Omega$ [W μm^{-1}]

L_λ [W m^{-2} sr^{-1} μm^{-1}] is the incident spectral radiance

$\text{A}\Omega \ [\text{m}^2 \ \text{sr}]$ is the detector area x field-of-view product

hence

$$N_\lambda = \Phi_\lambda/E_\lambda = L_\lambda A\Omega \ \lambda/hc \ [\text{p s}^{-1}] \tag{A.5}$$

and therefore

$$i_\lambda = R_\lambda^{\text{diode}} q \ A\Omega \ L_\lambda\lambda/hc = R_\lambda^{\text{diode}} A\Omega \ L_\lambda\lambda/1.2395 \ \text{W} \ \mu\text{m Amps}^{-1}[\text{Amps}/\mu\text{m}] . \tag{A.6}$$

Integrating over all wavelengths we have

$$i = \frac{A\Omega}{1.2395 \ \text{W} \ \mu\text{m Amps}^{-1}} \int_{200}^{1200} L_\lambda R_\lambda^{\text{diode}} \lambda d\lambda \ [\text{Amps}]. \tag{A.7}$$

Excitation occurs for all photons whose energy is at least as great as the energy gap, E_g, or

$$\lambda_{\text{cut-off}} = 1.2395 \ \text{eV} \ \mu\text{m}/E_g \ [\mu\text{m}] \tag{A.8}$$

For silicon, E_g=1.12 eV at 295 K (22C), and therefore the wavelength cut-off is 1.1 μm. This establishes a theoretical upper wavelength cut-off, used for camera studies. The lower limit is determined by the filter properties, which are measured down to 200 nm. By inspection of these data, a lower limit cut-off of 365 nm is selected for the camera's response function. It is noted that the lower and upper limits for the photodiodes covers a broader range. This is because the IQE is greater for these high quantum efficiency devices.

A.1.2 Laboratory standards

The photodiode standards used preflight are termed the "laboratory standards". They are used to provide the integrating sphere calibration prior to each camera's calibration[66]. Tube assembly #1 is used, which has an A of 3.86 x 10^{-8} m^2 sr. A set of laboratory filters, at the back end of the baffle tube, are used to measure incident radiance in a MISR-like spectral region. These filters were provided by the MISR filter vendor, and are manufactured to the same design as the flight filters. The transmission of the laboratory standard filters has been measured by using a Cary spectrometer. The separation between the filter and the diodes in the standards is sufficient to minimize the out-of-band scattering problems of the MISR filters.

The sphere itself contains 25 independent lamps (19 - 200 W and 6 - 30 W). The overall interior diameter of the sphere is 1.65 m and the aperture diameter is 76.2 cm. The small satellite sphere is used to fine tune low level red and IR radiances. For each MISR camera, we calibrate the sphere at 12 levels for each band at three different angles (right, center, and left), for a total of 144 radiances. The sphere also contains a photodiode stability monitor, which collects data during sphere operations. The stability monitor data is correlated to the laboratory standard and camera data readings by time tags to the files. These data are used to verify lamp stability during

calibration. Details of the set-up for the sphere calibration are contained in the Pre-Calibration Procedure[80].

In the ideal world, the response functions of both the photodiode standards and sensor to be calibrated would be the same. This would allow the camera-incident, band-weighted radiances to be computed directly from the photodiode current, along with Eqn. 7:

$$L_b^{ideal} = \frac{\int L_\lambda R_\lambda \lambda d\lambda}{\int R_\lambda \lambda d\lambda} = \frac{1.2395 \ i \ W \ \mu m \ Amps^{-1}}{A\Omega \int R_\lambda \lambda d\lambda} . \tag{A.9}$$

where R_λ would refer equally to the photodiode or sensor response function. The limits of integration are wavelengths where R_λ has finite response. As the photodiode standards, measured CCD, and standardized spectral response functions are unique, corrections are made for their differences, and the above approach is abandoned. Instead, the currents measured by the diode standards are converted to a monochromatic radiance by using an approximate form of Eqn. 9.

$$L_b^{lab} = \frac{1.2395 \ i \ W \ \mu m \ Amps^{-1}}{A\Omega \ \lambda^{lab} \Delta\lambda^{lab} R^{lab}} \tag{A.10}$$

where,

L^{lab} is the calibration source spectral radiance in $W \ m^{-2} \ sr^{-1} \ m^1$.

$\lambda^{lab}, \Delta\lambda^{lab}, R^{lab}$ are the source weighted, moments analysis parameters associated with the photodiode standard, as computed from the equations below:

$$\lambda^{lab} = \int \lambda \cdot P_\lambda(\lambda, 3100) R_\lambda^{lab} d\lambda / \int P_\lambda(\lambda, 3100) R_\lambda^{lab} d\lambda$$

$$\sigma^2 = \int \lambda^2 \cdot P_\lambda(\lambda, 3100) R_\lambda^{lab} d\lambda / \int P_\lambda(\lambda, 3100) R_\lambda^{lab} d\lambda - (\lambda^{lab})^2$$

$$\lambda_{u,l} = \lambda^{lab} \pm \sqrt{3} \cdot \sigma$$

$$\Delta\lambda^{lab} = 2\sqrt{3} \cdot \sigma$$

$$R^{lab} = \frac{1}{\Delta\lambda^{lab}} \int R_\lambda^{lab} d\lambda \tag{A.11}$$

λ has units [μm]

T has units [K]

$P_\lambda(\lambda, T)$ = Planks distribution = $c_1 \lambda^{-5} (\exp(c_2/T)-1)^{-1}$ [$W \ m^{-2} \ sr^{-1} \ \mu m^{-1}$]

$c_1 = 2hc^2 = 1.19096 \times 10^8$ [W m^{-2} sr^{-1} μm^{-4}]

$c_2 = hc/\lambda k = 1.43879 \times 10^4$ [μm K] (k is Boltzmann's constant).

Here a Planck distribution at temperature T=3100K is used to approximate the relative sphere output. It is this monochromatic radiance which is assumed during preflight camera calibration. (Recall from Chapter 1 we use the symbol L_b to denote radiances at a band-center wavelength, and L_b to denote band-weighted radiances). Section 3 will describe how the camera DN are used to retrieve band-weighted radiances, given the sphere calibration of Eqn. 10.

The product of the filter transmission values, the diode internal quantum efficiency (IQE), and a 3100K blackbody radiance, is calculated over the range of 200 - 1200 nm.

In the preflight analysis, the gain coefficients, G_i^{lab}, are first determined from a regression of DN versus the source radiances weighted over the laboratory standard's passband response, L_b^{lab}:

$$(DN - DN_o) = G_0^{lab} + G_1^{lab} L_b^{lab} + G_2^{lab} (L_b^{lab})^2 .$$ (A.12)

(The choice of the calibration equation form will be discussed in Section 3). By writing the desired equation

$$(DN - DN_o) = G_0 + G_1 L_b^{std} + G_2 (L_b^{std})^2 ,$$ (A.13)

and by making the approximation

$$L_b^{std} = L_b^{lab} k_{std\text{-}lab} , \text{ with}$$

$$k_{std\text{-}lab} = \frac{\int P_\lambda(\lambda, 3100) S_\lambda \lambda d\lambda}{\int P_\lambda(\lambda, 3100) R_\lambda^{lab} \lambda d\lambda} ,$$ (A.14)

we can make the correction for spectral differences after-the-fact. This was necessary, in that the standardized spectral parameters were not available during preflight data analysis. The relationships of the respective G_i coefficients can be found from the above equations as

$$G_0 = G_0^{lab}$$

$$G_1 = G_1^{lab} / k_{std\text{-}lab}$$

$$G_2 = G_2^{lab} / k_{std\text{-}lab}^2$$ (A.15)

Although not required by our algorithms, it is possible to develop the relationships between the desired G_i coefficients, and those used to retrieve monochromatic radiances, G_i^m. Consider the equation

$$(DN - DN_o) = G_0^m + G_1^m L_b^{std} + G_2^m (L_b^{std})^2 \quad , \tag{A.16}$$

as compared to the desired analysis represented by Eqn. 13. that desired regression computes the G_i coefficients using DN and band-weighted radiances, L_b. First the relationship between the radiances is estimated as:

$$\mathcal{L}_b^{std} = k \ L_b^{std} \ , \text{ where} \tag{A.17}$$

$$k = \frac{1}{P_b^{std}} \frac{\displaystyle\int_{365}^{1100} P_\lambda(\lambda, 3100) S_\lambda \lambda d\lambda}{\displaystyle\int_{365}^{1100} S_\lambda \lambda d\lambda} \tag{A.18}$$

$$P_b^{std} = P_\lambda(\lambda^{std}, 3100) \tag{A.19}$$

Here, the sphere spectral shape is approximated using the bulb-color temperature and Plancks equation. This temperature, 3100K, is provided by the sphere manufacturer, and confirmed by a best-fit Planck equation to the sphere output, as measured in the four MISR bands. The function S_λ is the standardized response of the camera.

In comparing Eqn. 13 with Eqn. 16, we observe

$G_0 = G_0^m$

$G_1 = G_1^m / k$

$G_2 = G_2^m / k^2$. $\tag{A.20}$

A.1.3 CCD devices

The response of a CCD device to an incident field is similar to Eqn. 7, but includes the integration time, t [s], and analog-to-digital conversion factor, g [DN/e]. Also, it has been determined that a quadratic calibration equation produces lower residuals, as compared to a linear approximation to the measured radiometric transfer curve[50]. The equations in this and the next

section, therefore, do not represent the final transfer equation, but motivate the approach that will be more precisely defined in Section 3. With this caveat, the DN is related to radiance by

$$DN = \frac{A\Omega tg}{hc} \int\limits_{365}^{1100} L_\lambda R_\lambda \lambda d\lambda \ [DN].$$
(A.21)

where here again the response, R_λ includes the detector quantum efficiency, and any optical transmittance terms, including the filter and lens. As stated earlier, the lower and upper wavelength cut-offs have been established to be 365 nm and 1100 nm, respectively.

It is noted that only the integral of the scene radiance, L_λ, with the system response function, R_λ, can be measured. In order to retrieve a parameter that is independent of the instrument characteristics, an assumption as to the relative scene spectral profile would be needed. Rather, one could simply choose to retrieve a band-weighted radiance, as this is more directly related to the camera output. The most accurate parameter to retrieve would be

$$L_b^{meas} = \frac{\int\limits_{365}^{1100} L_\lambda R_\lambda \lambda d\lambda}{\int\limits_{365}^{1100} R_\lambda \lambda d\lambda}$$
(A.22)

The radiometric calibration process would empirically determine the system gain, G^{meas}, from

$$DN = G^{meas} L_b^{meas}.$$
(A.23)

Ideally, L_p^{meas} would be determined by a standard detector with the same relative spectral profile as the system under test. From these equations we expect the measured constant, G^{meas}, to be proportional to

$$G^{meas} = \frac{A\Omega tg}{hc} \int\limits_{365}^{1100} R_\lambda \lambda d\lambda \ .$$
(A.24)

This approach is not practical for MISR, as it would produce radiance products that have a unique spectral weighting for each of the 1504 x 9 different detector elements within a band. Further, the photodiode standards have slightly different response functions, R_λ^{diode}, even when identical filters are used. This is due to detector quantum efficiency, optical transmittance differences, and differences in the filters. They do not, therefore, provide a direct measure of the CCD spectral weighted radiances. For these reasons MISR prefers to deliver scene radiances that

are weighted by a fixed spectral response function, $S_{\lambda,b}$, unique only for each of the four spectral bands. This standardized response function is to be created as the average of the measured profiles, and is used to retrieve

$$L_b^{std} = \frac{\int\limits_{365}^{1100} L_\lambda S_\lambda \lambda d\lambda}{\int\limits_{365}^{1100} S_\lambda \lambda d\lambda} \ . \tag{A.25}$$

With knowledge of the calibration source output, L_b^{std}, the cameras are calibrated via a regression of the form

$$DN = G^{std} L_b^{std}. \tag{A.26}$$

Although G^{std} is empirically determined, a model derivation of its value provides insight into the assumptions associated with the calibration process.

Using the above equations, it can be shown

$$G^{std} = \frac{DN}{L_b^{std}} = \frac{G^{meas} L_b^{meas}}{L_b^{std}} = G^{meas}\left(\frac{\int L_\lambda^{cal} R_\lambda \lambda d\lambda}{\int R_\lambda \lambda d\lambda} \Big/ \frac{\int (L_\lambda^{cal} S_\lambda \lambda d\lambda)}{\int S_\lambda \lambda d\lambda}\right) \ . \tag{A.27}$$

Here L_b^{meas} and L_b^{std} are the band weighted response functions, when viewing a calibration target, as weighted by a camera's measured and standardized response function, respectively. The limits of integration are over the entire response range, 365 to 1100 nm. In practice, then, the coefficient G^{std} is shown to be correct for differences between the actual detector response, and the standardized response. Note that $G^{std} \sim G^{meas}$ provided $S_\lambda \sim R_\lambda$.

In using this approach for scene radiance retrieval, L_b^{ret}, it is shown that

$$L_b^{ret} = \frac{DN}{G^{std}} = (L_b^{meas,scene} \ L_b^{std,cal})/L_b^{meas,cal} \ . \tag{A.28}$$

From this we see that we have the desired relationship

$$L_b^{ret} = L_b^{std,scene} \tag{A.29}$$

provided either the scene and calibration source have the same relative spectral shape, or provided the measured and standardized spectral response functions are nearly identical. The first assumption will hold true for the in-flight calibration, provided the scene reflectance is spectrally flat.

In general, it is believed this calibration approach corrects, to first order, for differences in spectral profiles among the detector elements of a given band. The assumptions are believed to contribute no more than a percent error at low scene reflectances, and produce a negligible error at more typical radiance levels[5].

A.2   SOURCE CORRECTION

Using this model approach, it can be shown that MISR will not need to apply a source-correction scaler to the preflight-determined calibration coefficients. This is sometimes done by other programs, to account for the source-color differences between the laboratory calibration (using a sphere source), and Sun color temperature. The argument for using these correction factors is that the Sun-illuminated target provides a different out-band target, which affects the gain constant. As MISR is reporting band-weighted radiances, this correction is not needed, as will be explained in this section.

Consider the case where a sensor is used to report the monochromatic radiance at the band center wavelength. An equation of the form

$$DN = G_m L_b^{meas}$$ (A.30)

might be adopted, where L_b^{meas} is the monochromatic radiances of calibration source or scene under view, at the sensor wavelength $\lambda^{std} = \lambda_{m,solar,b}^{std}$. The DN reported by a camera, when viewing an integrating sphere, may also be found using a Planck relative spectral distribution approximation, at a color temperature of T=3100 K, and the following equation

$$DN = \frac{kL_b^{lab}}{P_b^{std}} \int P_\lambda(\lambda, 3100) R_\lambda \lambda d\lambda$$ (A.31)

where L_b^{lab} is the radiance measured by the photodiode standard, at wavelength λ^{std}, P_b^{std} is the Planck function value at wavelength λ^{std} (a normalization factor), and $k = \frac{A\Omega Tg}{hc}$ from Eqn. 24. Thus, we have

$$G_m = \frac{k}{P_b^{std}} \int P_\lambda(\lambda, 3100) R_\lambda \lambda d\lambda$$ (A.32)

For the retrieval of a Solar-illuminated scene a source correction adjustment, F^{source}, is needed such that $L^{ret}=L^{scene}$:

$$L_b^{ret} = \frac{DN}{F^{source}G_m} = \frac{\left(\dfrac{kL_b^{scene}}{F^{source}P_\lambda(\lambda^{std}, 5800)}\int P_\lambda(\lambda, 5800)R_\lambda\lambda d\lambda\right)}{\dfrac{k}{P_\lambda(\lambda^{std}, 3100)}\int P_\lambda(\lambda, 3100)R_\lambda\lambda d\lambda} \qquad (A.33)$$

hence

$$F^{source} = \frac{P_b(\lambda^{std}, 3100)\int P_\lambda(\lambda, 5800)R_\lambda\lambda d\lambda}{P_b(\lambda^{std}, 5800)\int P_\lambda(\lambda, 3100)R_\lambda\lambda d\lambda} \qquad (A.34)$$

Here $P_\lambda(\lambda, 5800)$ is used to approximate the exo-atmospheric solar irradiance. To estimate the magnitude of this correction, the difference between $F^{source}G_m$ and G_m is 6% at 450 nm, but only 1% at 1000 nm. This assumes a square band response, of width 20 nm. If a 10^{-3} out-band rejection is added, the difference in the gains is 34% and 1% at these same wavelengths, respectively. The Band 1 correction is greater, as the differences in the normalized shapes of the Sun and sphere sources is greatest for blue wavelengths.

Next, consider the case where a sensor reports a band-weighted radiance, as does MISR. During preflight calibration photodiode standards are used to measure L_b^{cal}. This is multiplied by a constant (see next Section) to obtain L_b^{cal}, the radiance weighted over the measured spectral response function. Next, using G^{meas} per Eqn. 26, it can be found that

$$L_b^{ret} = \frac{DN}{G^{meas}} = \left(\frac{kL_b^{scene}}{P_b(\lambda^{std}, 5800)}\int P_\lambda(\lambda, 5800)R_\lambda\lambda d\lambda\right)/(k\int R_\lambda\lambda d\lambda) = L_b^{scene} \qquad (A.35)$$

it is shown that $L^{ret} = L^{scene}$ exactly, without use of a source correction factor. As was mentioned in the previous section, this assumes that $S_\lambda \sim R_\lambda$.

A.3 QUADRATIC CALIBRATION EQUATION

From the above analysis it has been shown that the preferred calibration approach is to provide a data regression to a calibration equation of the form of Eqn. 26. In practice, analysis has shown that the smallest residuals are obtained with use of a quadratic calibration equation[65]. MISR therefore adopts the following relationship:

$$(DN - DN_o) = G_0 + G_1 L_b^{std} + G_2 (L_b^{std})^2 \qquad (A.36)$$

where

$L_b^{std} =$ incoming spectral radiance weighted by the standardized spectral response [W m^{-2} μm^{-1} sr^{-1}];

$DN - DN_o =$ offset subtracted sensor digital number output [DN];

$G_0 =$ detector gain coefficient [DN];

$G_1 =$ detector gain coefficient [(W m^{-2} μm^{-1} sr^{-1})$^{-1}$ DN]; and

$G_2 =$ detector gain coefficient [(W m^{-2} μm^{-1} sr^{-1})$^{-2}$ DN].

The standardized band weighted radiance can be found from the flight diode current using the expression

$$L_b^{std} = \frac{1.2395 \ i \ E_{0b} \ \text{W} \ \mu\text{m} \ \text{Amps}^{-1}}{1200} \Big/ A\Omega \int_{200} E_{0\lambda} R_\lambda^{OBC} \lambda d\lambda \qquad (A.37)$$

The above represents a simplified notation, as the ARP requires the G_i coefficients (where i=0,1, or 2) to be computed for 3 averaging modes, am, 36 channels, c, and s output samples (where s=1504 when am=1x1, s=752 when am=2x2, and s=376 when am=4x4). Thus, in the most general case we will use the notation $G_i(am,c,s)$.

Coefficients for the 2x2 and 4x4 averaging modes will be constructed from the 1x1 (unaveraged) mode, by averaging each of G_0, G_1, and G_2 over the appropriate number of consecutive pixels:

$$G_i(2x2,c,s) = \frac{1}{2} \sum_{j=2s-1,2s} G_i(1x1,c,j) \ , \text{and} \qquad (A.38)$$

$$G_i(4x4,c,s) = \frac{1}{4} \sum_{j=4s-1,4s} G_i(1x1,c,j) . \qquad (A.39)$$

The resulting parameters will be validated, as the mission operations plan calls for the collection of data in all averaging modes, during calibration diffuse-panel view.

APPENDIX A. Radiometric equation development

APPENDIX B. PREFLIGHT CAMERA CALIBRATION

B1. TESTING OVERVIEW

Some degree of testing of MISR flight hardware is done at the component, camera, and system levels, as well as after shipment and integration onto the spacecraft. The bulk of the performance data, however, are collected at the camera level of assembly. By characterizing each camera individually, testing can be spread sequentially over time and the test hardware is simplified. Camera testing is done using two MISR-dedicated thermal vacuum chambers. The camera-level approach to characterization also permits camera spares to be stored as calibrated, ready to fly hardware. The shorter system level tests are to be conducted in shared, more costly facilities. Radiometric stability is verified at the system level of assembly by deploying and illuminating the flight diffuse panels. Instrument geometric stability is characterized at the system level with use of a calibrated nine-collimator fixture which rests on the instrument optical bench during test.

Table B1. Optical Characterization Chamber (OCC) tests. Here pinhole imaged onto camera via collimator and camera is mounted to two axis gimbal.

Test name.	Test description	Test deliverables
Boresight	Collimated beam illuminates camera at angle perpendicular to lens mounting flange (no gimbal skewing).	Provides verification that boresight is within 8 pixels of CCD array center. Specific boresight location feeds into camera pointing model.
Point-spread-function (PSF) response.	Scan accomplished by moving gimbal in 0.1 pixel steps at five field points. Repeated with white and filtered light.	Provides cross- and down-track point-spread function. Used to predict contrast target response, and available for at-launch contrast sharpening algorithm. Used to measure optical and electrical spectral crosstalk terms. Used to determine MTF and verify MTF specification (26% beginning of life at pixel sampling frequency).
Effective focal length	Same as above.	Best focus position determined at lens level of assembly. Camera assembled using appropriate shims to place detector at focus. Focus verified at camera through temperature range.

Table B1. Optical Characterization Chamber (OCC) tests. Here pinhole imaged onto camera via collimator and camera is mounted to two axis gimbal.

Test name.	Test description	Test deliverables
Distortion mapping	Same as above, but over entire CCD array. White light only.	Measures deviation of image point from h=EFL tan θ. Provides pixel IFOV knowledge to subpixel accuracy.
Stray light	Pinhole illuminates various field points outside of the sensor field-of-view. Pinhole stationary to allow pixel summing.	Used to verify 10^{-5} out-of-field stray-light rejection.
Blooming, time response, and hysteresis studies	The pinhole source is shuttered to determine time response. Neutral density filters and camera integration time controlled saturated conditions (10 times full well).	Used to verify detector response specifications: time response for within dynamic range signals; saturation recovery in both the spatial and temporal dimensions.

The specific tests conducted in each of the two thermal vacuum chambers are summarized in Table B1. After assembly a camera first goes to the Optical Characterization Chamber (OCC). The Optical Characterization Chamber (OCC) is a thermal-vacuum test facility that was used for both MISR lenses and camera subsystems. Data acquired from this chamber have allowed for the characterization of the camera instantaneous fields-of-view, relative pixel pointing angles, effective focal length, Modulation Transfer Function (MTF), point-spread function (PSF), and saturation response.

The chamber is a cylinder four feet in diameter and five feet in length with hinged doors at both ends. The chamber has been constructed to operate in high vacuum (about 10^{-6} torr) and is equipped with feed-thrus for electrical power and signals, lines for gaseous nitrogen, and a fiber optic cable. The principal hardware inside the chamber is a two-axis gimbal, a thermal header attached to the inner gimbal, a 1-m focal length collimator (off-axis parabola), and a target wheel at the focus of the collimator.

The lens or camera under test mounts to the thermal header. The temperature of the test item is set by controlling the temperature and flow rate of the gaseous nitrogen through the thermal header. The lens or camera is then cooled (or heated) by conduction. This arrangement allows testing of lenses and cameras over the expected operational range (0 to 10°C) and the range of survival temperatures (-30 to 60°C) but keeps the chamber optics at ambient temperature and thus does not disturb their alignment (see below).

The fiber optic cable transmits light from the source light house, located outside the clean room, through the chamber wall to the target wheel. The light house contains a xenon bulb, variable attenuator, and space for inserting spectral filters. This flexible setup allows the user to

choose the source spectral range and intensity. The target wheel contains four pinhole positions (35, 50, 100, and 200 min diameter) and three extended source (half plane, central obstruction, no obstruction) positions. The size of the pinhole is changed to match the lens or camera entrance pupil.

Light from the selected pinhole object in the target wheel is collimated by the off-axis parabola and redirected to the lens or camera under test by two turning flats. The turning flats are aligned such that an autocollimating mirror mounted flush to the thermal header interface surface will superimpose the pinhole image on the object when the gimbal encoders read zero in both axes. Thus, the gimbal zero position implies that the surface of the lens/camera interface flange is perpendicular to the incident light; this orientation defines the boresight of the unit under test.

The gimbal was designed to be able to cover the entire MISR field of view. In the crosstrack direction, the shortest focal length camera requires coverage of ±15° but only about ±0.3° in the downtrack direction. The gimbal is capable of being rotated more than ±20° and hence can be used to examine the effect of illumination outside the active pixel area.

For lens testing a microscope objective/video camera attached to a three-axis translation stage is installed inside the OCC behind the lens. The video camera records the image formed by the lens at a magnification of 40. The translation stages allow the microscope to determine the optimum focal plane for various wavelengths, temperatures, and field points by performing through-focus measurements. The optimum focus point is based on the criterion of a maximum in the modulation transfer function (MTF). These measurements are facilitated by positioning the lens in the thermal header such that its nodal point is coincident with the gimbal rotation axes. In this situation the images from various field points come to focus at different points along the optical axis but are not displaced in the transverse directions. The lens tests yield the effective focal length (EFL) of the lens, a mapping of the optimum focal plane, and the lens MTF in the optimum focal plane.

For camera testing the microscope objective/video camera and the translation stages are removed. To determine the MTF of the camera (lens and detector combined), the image of the appropriate pinhole is scanned slowly over a selected set of pixels. This lens image/detector responsivity convolution is then Fourier transformed to yield the MTF in the scan direction. The other principal camera test performed is determining the crosstrack viewing angle of each active pixel. This measurement is referred to as the pixel-theta test and is a measure of the camera distortion. This test is described in great detail[10]. The MTF and pixel-theta measurements, combined with the determination of EFL (comes from pixel-theta measurement), boresight, and stray light constitutes the standard set of measurements performed on all cameras in the OCC. In addition to these standard tests, several special tests dealing with saturated pixels, and optical and electrical crosstalk between CCD channels were performed.

After testing in the OCC, a given camera is next moved to the Radiometric Characterization Chamber (RCC). This chamber has a 0.5 m (20") diameter window within it's door. Either a monochromator or integrating sphere are wheeled in front of the chamber, illuminating the camera through this window. Tables A.2 and A.3 describe tests conducted with these respective sources. For the spectral tests each pixel analyzed is parameterized in terms of a

best-fit Gaussian to the in-band region, this being the 1% points with respect to the peak. As the band profile was specified to be Gaussian, it is believed that this function best represents a simplified spectral response function, with parameterization derived so as to preserve the integrated energy. As the MISR filters do have a finite out-of-band response, however, an equivalent parameterization is desired which accounts for the out-of-band energy. For this an equivalent square-band analysis is made. Out-of-band response beyond the limits of the monochromator (900 nm) is determined by use of a bandpass filter covering the 900 to 1100 nm region. This filter is used to prefilter the light while the camera views the integrating sphere.

Table B2. Radiometric Characterization Chamber. Monochromator illuminates camera via window in chamber door.

Test name.	Test description	Test deliverables
SpectCal-In band	Scan monochromator from 400 to 900 nm in 0.5 nm steps, setting exit slit to 1 nm dispersion.	Gaussian in-band best-fit response parameters.
SpectCal-Out band	Scan monochromator from 400 to 900 nm in 10 nm steps, setting exit slit to 20 nm dispersion.	Equivalent square band response determined using moments analysis. Provides out-band rejection and response function for out-of-band correction to the flight data.

Table B3. Radiometric Characterization Chamber. Integrating sphere illuminates camera via window in chamber door.

Test name.	Test description	Test deliverables
Light transfer	At fixed integrating sphere output level, ramp camera from 0.32 to 40.8 ms integration times (full available range).	Determines ADC gain, electronics linearity and linearity range, and desired camera integration time.
RadCal	Set the integrating sphere to one of 12 precalibrated output levels per band. Turn off bulbs and adjust external sphere aperture to sequence through all preprogrammed levels. Repeat for all 4 MISR spectral bands.	Provides the sensor absolute and relative radiometric calibration, radiance uncertainty, and signal-to-noise performance.

Table B3. Radiometric Characterization Chamber. Integrating sphere illuminates camera via window in chamber door.

Test name.	Test description	Test deliverables
Doubling	At 9 radiometric levels, each achieved by two identical bulb groupings, acquire data with first, second, then and both bulb sets in turn.	Verifies linearity over sensor dynamic range where radiometric accuracy requirements are defined (ρ_{eq}=100%. to 5%).
Polarization	Rotate polarizing sheet (ambient test).	Verifies camera ±1% polarization insensitivity specification.

The integrating sphere used in these tests is 1.6 m (65") in diameter, has a 76x23 cm (30x9") exit port, and a 30 cm (12") external sphere with variable aperture.The main sphere is illuminated with use of eighteen 200 W bulbs and six 30 W bulbs; the satellite sphere has a single 200 W bulb. The sphere is sequenced through a number of lamp-on settings, allowing digital data to be collected at multiple radiometric levels. The coefficients in the calibration equation are determined for each pixel using these data. A statistical approach called the Fidelity Analysis is used to fit a quadratic through the data, provide a measure of the uncertainty in this fit, and extrapolate the uncertainty to an arbitrary radiometric level. With these pixel coefficients the radiance of the scene can be determined from the camera DN output. In addition to the radiometric uncertainties determined in this manner, there is a systematic uncertainty of about 2% in the laboratory detector standards. Another contributor to radiometric error is the sphere drift between calibrations. By monitoring the sphere with an internal photodiode during testing, the total radiance and equivalent reflectance retrieval error can be reduced such that we meet the 3% (1σ at ρ_{eq}=100%) uncertainty requirement.

B1.1 Preflight calibration

The preflight calibration coefficients have been reported in the design files69. They were developed by regressing data using Eqn. 8.12, then making a transformation of the coefficients using Eqn. 8.15.

Need to past back in what had in original version: computed monochromatic, then later converted to band averaged when had standardized response functions.

Table B4 presents the equivalent square-band parameters for the photodiode standards, as weighted by the sphere color temperature. These were the filters used to measure the sphere radiance.

Table B4. Equivalent Square Band Parameters for MISR Lab Filters

BAND	λ^{lab}, center wavelength (nm)	$\Delta\lambda^{lab}$, bandwidth (nm)	R^{lab}, transmission
1	447.567	59.418	0.406
2	556.917	35.382	0.382
3	670.886	35.703	0.295
4	867.584	51.994	0.433

B1.1.1. Laboratory standards

The preflight calibration of the MISR cameras has been documented in various MISR DFMs (see listing, Chapter 7). Also investigated were signal-to-noise, local response uniformity, and calibration repeatability. Additionally, a round-robin validation experiment was conducted at the MISR High Bay facility to compare the MISR radiometric scale against National Institute of Standards and Technology (NIST) measurements and those of other EOS calibration scientists. Agreement was within 3% for a substantial number of the data points[68]. The preflight calibration uncertainty budget is provided below

The uncertainty in the performance of the laboratory diode standards is given in Table 5. The QED-200 is used to calibrate Bands 1 and 2, while the QED-150 is used to calibrate Bands 3 and 4.

Table B5. Laboratory Diode Standards Radiance Uncertainties

Source Of Uncertainty	Uncertainty	Method
QED-200 (Blue) UDT Inversion Layer Diodes		
Internal QE >0.998 (400-700 nm)	0.2%	Intercomparison of different diode types
Reflection Loss <20% Per Diode	0.03%	JPL and Vendor tests
Linearity >99.8%	0.25%	Vendor test and JPL analysis
SNR 1000	0.1%	Test and analysis
Spectral Bandwidth 0.1 nm	0.3%	Cary measurements and analysis

APPENDIX. Preflight camera calibration

Table B5. Laboratory Diode Standards Radiance Uncertainties

Source Of Uncertainty	Uncertainty	Method
QED-200 (Blue) UDT Inversion Layer Diodes		
Filter Transmission ~60%	0.5%	Cary measurements and analysis
Out-of-band Transmission	0.1%	Cary measurements and analysis
Étendue 3.55 X 10^{-4} cm^2 sr	0.21%	Tolerancing and inspection of fabricated parts and alignment
RSS TOTAL	0.72%	
QED-150 (Red) Hamamatsu p-on-n Diodes		
Internal QE >0.996 (600-950 nm)	0.2%	Intercomparison of different diode types
Reflection Loss <30% Per Diode	0.24%	JPL and Vendor tests
Linearity >99.9%	0.25%	Vendor test and JPL analysis
SNR 2000	0.05%	Test and analysis
Spectral Bandwidth 0.1 nm	0.4%	Cary measurements and analysis
Filter Transmission ~60%	0.5%	Cary measurements and analysis
Out-of-Band Transmission	0.1%	Cary measurements and analysis
Étendue 3.55 x 10^{-4} cm^2 sr	0.21%	Tolerancing and inspection of fabricated parts and alignment
RSS TOTAL	0.79%	

B1.1.2. Error tables

This section needs a lot of work. There are multiple tables that need to be reconciled.

Table B6. Preflight absolute radiometric calibration uncertainties

REQUIREMENTS: 3% for ρ = 1.0; 6% for ρ = 0.05

SOURCE OF UNCERTAINTY	UNCERTAINTY ρ = 1.0	UNCERTAINTY ρ = 0.05	GROUNDS
RADIANCE	0.60% Bands 1,2 0.49% Bands 3,4	0.60% Bands 1,2 0.49% Bands 3,4	LABORATORY DIODE STANDARDS
SPHERE NON-UNIFOR-MITY	0.5%	0.5%	VENDOR SPECIFIED VALUE JPL WITNESS TEST
CAMERA SNR	0.06%	0.3%	1/(700*2.24); 1/(150*2.24) 5x SUM
SOURCE DYNAMIC RANGE LIMITATIONS	0.6%	2.3%	FIDELITY INTERVAL COMPONENT ASSUMING CALIBRA-TION OVER LESS THAN FULL DYNAMIC RANGE
SPECTRAL NON-UNIFORMITY	1.3%	1.3%	0.48 nm UNCER-TAINTY IN BAND-WIDTH ACROSS FOV
NON-LINEARITY	0.5%	0.5%	DOUBLING DEVIA-TION METHOD
STABILITY	1.0%	1.0%	VENDOR VALUE / MONITORED
TEMPERATURE EFFECTS	0.01%	0.2%	EFFECTS OF 1 C TEMPERATURE VARI-ATION DURING TEST
RSS TOTAL	2.0% Bands 1,2 2.0% Bands 3,4	3.0% Bands 1,2 3.0% Bands 3,4	

Table B7. Preflight relative radiometric calibration uncertainties

REQUIREMENT

EQUIVALENT REFLECTANCE	MAXIMUM PIXEL-TO-PIXEL RADIOMETRIC UNCERTAINTY	MAXIMUM BAND-TO-BAND RADIOMETRIC UNCERTAINTY	MAXIMUM CAMERA-TO-CAMERA RADIOMETRIC UNCERTAINTY
1.0	0.5%	1.0%	1.0%
0.05	1.0%	2.0%	2.0%

UNCERTAINTY

SOURCE OF UNCER-TAINTY	Pixel/ pixel $\rho = 1.0$	Pixel/ pixel $\rho = 0.05$	Band/ band $\rho = 1.0$	Band/ band $\rho = 0.05$	Camera/ camera $\rho = 1.0$	Camera/ camera $\rho = 0.05$	GROUNDS
SPHERE NON-UNI-FORMITY	0.5%	0.5%	0.5%	0.5%	0.5%	0.5%	VENDOR SPECIFIED VALUE
SPHERE RELATIVE STABILITY	--	--	--	--	0.2%	0.2%	VENDOR SPECIFIED VALUE
SNR	0.06%	0.3%	0.06%	0.3%	0.06%	0.3%	1/(700*2.24); 1/(150*2.24)
RSS TOTAL	0.50%	0.58%	0.50%	0.58%	0.54%	0.62%	

The error sources identified as contributing to the preflight radiometric calibration are given in Table 8 below. A description of these errors is briefly provided, along with their values at two specific radiometric levels. The at-launch ARP will be populated with uncertainty values determined from this preflight analysis. For the ARP, however, the analysis is extended to 15 radiometric levels, using the algorithms provided here. A complete description of the preflight uncertainties are documented in MISR SDFM#91, Rev. A. which summarizes the results for all 15 radiometric input levels. Error values distinguished with an "*" are independent of radiometric level. To compute the various error terms, RSS are taken using values checked, $\sqrt{}$, within a given row. Absolute errors are computed using checked parameters within the absolute error column, etc. Values with a check $\sqrt{}$ are used to provide the total error for 1x1 averaging mode. Values with a check $\sqrt{}$sys are RSS to provide the systematic error terms. Both total and systematic values are

used in deriving values reported to the ARP. The Fidelity Interval analysis does not enter into the ARP report, but used as a consistency check. These preflight values are computed and loaded into the initial ARP file. As the IFRCC processing software does not recompute these values, the algorithm description (identical in approach preflight and post-launch), is deferred to the OBC discussion. The reader is additionally referred to SDFM#91, Rev. A for any further algorithm clarifications used to derive these data.

Table B8. Preflight sources of radiometric uncertainty

Parameter	% uncertainty at ρ_{eq}=1.	% uncertainty at ρ_{eq}=0.05	Uncertainty type			
			Absolute error term	Camera vs. camera	Band vs. band	Pixel vs. pixel
Diode radiance accuracy: internal QE, linearity, SNR, AΩ	0.8	0.8*	√, √sys			
Diode radiancy accuracy: filter transmittance	0.5	0.5*			√, √sys	
Diode to camera out-of-band correction	1.	1.*	√, √sys			
Sphere non-uniformity correction	0.5	0.5*	√, √sys	√, √sys		√, √sys
Sphere temporal stability	1.	1.*	√, √sys	√, √sys		
Sphere color temperature stability	0.1	0.1*			√, √sys	
Calibration equation fit			√, √sys			
Finite radiometric levels			√, √sys			
SNR: dark current and photon noise			√, √sys	√, √sys	√, √sys	√, √sys
Quantization			√	√	√	√
Fidelity Interval (FI) {Band 1/ Blue, Band 2/ Green, Band 3/ Red, Band 4/ NIR}	{0.53, 0.10,0.30, 0.13}	{0.66, 1.7, 4.7, 2.2}	Used as verification of the last 4 errors.			

- **diode radiance accuracy.** MISR has made use of commercial light-trapped, high quantum-efficient photodiodes as its radiometric standards. These are used to establish the integrating sphere output, at the four MISR spectral bands. The terms considered in

Row 1 include photodiode internal quantum efficiency, reflection loss, linearity, signal-to-noise (SNR), spectral response knowledge, and the area-solid angle ($A\Omega$) uncertainty. The photodiode filter transmittance uncertainty appears separately in Row 3, as it dominates the band-to-band uncertainty for the sphere output levels used in calibration testing.

- correction for diode-to-camera out-of-band differences. Although the filters used for the cameras and laboratory photodiode standards are of the same design, the final as-built responses are slightly different for the two. These differences are characterized, and corrections are made with these measurements.

- sphere non-uniformity knowledge. The sphere has been measured to be 3% different at the field-edges, as compared to smaller view angles. This output deviation with view angle is slowly varying, and thus only a few measurement points are needed to characterize this non-uniformity. This determination is used to adjust the incident radiances over the field-of-view of a given camera.

- sphere stability. Stability monitor readings are recorded both during calibration of the sphere, and calibration of the cameras. Sphere stability is measured to be 1%, after a warm-up period of 20 minutes. No correction is made for this drift.

- sphere color temperature stability. Should there be a drift in the sphere bulb temperature, there would be a corresponding change in the sphere output radiance, one-band relative to another. The magnitude of this error has not been characterized, except to assume it is much less than the overall sphere stability reported above.

- calibration equation fit. Determined from DFM# (Nadine's calibration equation memo).

- quantization error. Estimated from the camera radiometric model.

- snr : photon noise and dark current. Measured as the variance from the mean of 64 data samples, at a given sphere output level. Modeled where measurement unavailable.

- finite radiometric levels. Estimated from the second term of Eqn. 8.62 (i.e., that within the { }).

- Fidelity Interval. The regression of camera output digital numbers against incident radiances provides the desired calibration gain coefficients terms. By making use of the Fidelity Interval analysis to perform this fit, we can also obtain an uncertainty of the fit due to camera signal-to-noise, goodness of fit of the calibration equation to the measured data, and adequacy of the sphere output range to that of the detector range to be calibrated.

(To address one reviewers concern, the thermal vacuum window does not contribute to the preflight radiometric error, as the laboratory standards which are used to establish the output of

the integrating sphere look through the chamber window, as do the cameras during calibration data acquisition.)

Using the data within Table 8, a root-sum-squared (RSS) is taken of values along a given column to produce the absolute, camera relative, band relative, and pixel relative errors. Table B9 provides the results of this analysis, for the two radiometric levels so indicated, and for the systematic and total parameters.

Table B9. Preflight radiometric uncertainties

Radiometric uncertainty	Actual		Requirement	
	% uncertainty at ρ_{eq}=1.	% uncertainty at ρ_{eq}=0.05	% uncertainty at ρ_{eq}=1.	% uncertainty at ρ_{eq}=0.05
Absolute_sys				
Absolute	{1.8,1.7,1.7,1.7}	{1.9,2.5,5.0,2.8}	3.	6.
Camera-to camera relative_sys				
Camera-to camera relative	1.1	1.2	1.	2
Band-to-band relative_sys				
Band-to-band relative	0.5	0.7	1.	2.
Pixel-to-pixel relative_sys				
Pixel-to-pixel relative	0.1	0.5	0.5	1.